The Astrophysical Journal, 971:178 (31pp), 2024 August 20 https://doi.org/10.3847/1538-4357/ad54bd


# The Fraction of Dust Mass in the Form of Polycyclic Aromatic Hydrocarbons on 10–50 pc Scales in Nearby Galaxies

Jessica Sutter[1,2], Karin Sandstrom[2], Jérémy Chastenet[3], Adam K. Leroy[4,5], Eric W. Koch[6], Thomas G. Williams[7], Ryan Chown[4], Francesco Belfiore[8], Frank Bigiel[9], Médéric Boquien[10], Yixian Cao[11], Mélanie Chevance[12,13], Daniel A. Dale[14], Oleg V. Egorov[15], Simon C. O. Glover[12], Brent Groves[16], Ralf S. Klessen[12,17], Kathryn Kreckel[15], Kirsten L. Larson[18], Elias K. Oakes[19], Debosmita Pathak[4], Lise Ramambason[12], Erik Rosolowsky[20], and Elizabeth J. Watkins[21]

[1] Whitman College, 345 Boyer Avenue, Walla Walla, WA 99362, USA; sutterjs@whitman.edu
[2] Department of Astronomy & Astrophysics, University of California, San Diego, 9500 Gilman Drive, La Jolla, CA 92093, USA
[3] Sterrenkundig Observatorium, Universiteit Gent, Krijgslaan 281 S9, B-9000 Gent, Belgium
[4] Department of Astronomy, The Ohio State University, 140 West 18th Avenue, Columbus, OH 43210, USA
[5] Center for Cosmology and Astroparticle Physics (CCAPP), 191 West Woodruff Avenue, Columbus, OH 43210, USA
[6] Center for Astrophysics | Harvard & Smithsonian, 60 Garden Street, 02138 Cambridge, MA, USA
[7] Sub-department of Astrophysics, Department of Physics, University of Oxford, Keble Road, Oxford, OX1 3RH, UK
[8] INAF—Osservatorio Astrofisico di Arcetri, Largo E. Fermi 5, I-50125, Florence, Italy
[9] Argelander-Institut für Astronomie, Universität Bonn, Auf dem Hügel 71, 53121 Bonn, Germany
[10] Université Côte d'Azur, Observatoire de la Côte d'Azur, CNRS, Laboratoire Lagrange, 06000, Nice, France
[11] Max-Planck-Institut für Extraterrestrische Physik (MPE), Giessenbachstr. 1, D-85748 Garching, Germany
[12] Universität Heidelberg, Zentrum für Astronomie, Institut für Theoretische Astrophysik, Albert-Ueberle-Str 2, D-69120 Heidelberg, Germany
[13] Cosmic Origins Of Life (COOL) Research DAO, Germany[22]
[14] Department of Physics and Astronomy, University of Wyoming, Laramie, WY 82071, USA
[15] Astronomisches Rechen-Institut, Zentrum für Astronomie der Universität Heidelberg, Mönchhofstr. 12-14, D-69120 Heidelberg, Germany
[16] International Centre for Radio Astronomy Research, University of Western Australia, 7 Fairway, Crawley, 6009 WA, Australia
[17] Universität Heidelberg, Interdisziplinäres Zentrum für Wissenschaftliches Rechnen, Im Neuenheimer Feld 205, D-69120 Heidelberg, Germany
[18] AURA for the European Space Agency (ESA), Space Telescope Science Institute, 3700 San Martin Drive, Baltimore, MD 21218, USA
[19] Department of Physics, University of Connecticut, 196A Auditorium Road, Storrs, CT 06269, USA
[20] Department of Physics, University of Alberta, 4-183 CCIS, Edmonton, AB, T6G 2E1, Canada
[21] Jodrell Bank Centre for Astrophysics, Department of Physics and Astronomy, University of Manchester, Oxford Road, Manchester, M13 9PL, UK
*Received 2024 March 6; revised 2024 May 11; accepted 2024 May 23; published 2024 August 16*

## Abstract

Polycyclic aromatic hydrocarbons (PAHs) are a ubiquitous component of the interstellar medium (ISM) in $z \sim 0$ massive, star-forming galaxies and play key roles in ISM energy balance, chemistry, and shielding. Wide field-of-view, high-resolution mid-infrared (MIR) images from JWST provide the ability to map the fraction of dust in the form of PAHs and the properties of these key dust grains at 10–50 pc resolution in galaxies outside the Local Group. We use MIR JWST photometric observations of a sample of 19 nearby galaxies from the Physics at High Angular Resolution in Nearby GalaxieS (PHANGS) survey to investigate the variations of the PAH fraction. By comparison to lower-resolution far-infrared mapping, we show that a combination of the MIRI filters ($R_{\rm PAH}$ = [F770W+F1130W]/F2100W) traces the fraction of dust by mass in the form of PAHs (i.e., the PAH fraction, or $q_{\rm PAH}$). Mapping $R_{\rm PAH}$ across the 19 PHANGS galaxies, we find that the PAH fraction steeply decreases in H II regions, revealing the destruction of these small grains in regions of ionized gas. Outside H II regions, we find $R_{\rm PAH}$ is constant across the PHANGS sample with an average value of $3.43 \pm 0.98$, which, for an illuminating radiation field of intensity 2–5 times that of the radiation field in the solar neighborhood, corresponds to $q_{\rm PAH}$ values of 3%–6%.

*Unified Astronomy Thesaurus concepts:* Interstellar medium (847); Polycyclic aromatic hydrocarbons (1280); Interstellar dust (836)

## 1. Introduction

Dust is a key component of the interstellar medium (ISM) of galaxies, and plays important roles regulating the thermal and ionization balance within the ISM. Dust also absorbs and scatters ultraviolet (UV) and optical light, reprocessing on average an estimated ∼30% of the starlight produced in galaxies and reemitting it in the infrared (IR; Draine 2003). The composition, properties, and distribution of the dust set the ISM heating efficiency and determine attenuation, making the dust a key component of any ISM model. Of particular interest is the breakdown between larger carbonaceous and silicate dust grains and the smallest carbonaceous grains, the polycyclic aromatic hydrocarbons (PAHs). PAHs are widely considered to be responsible for broad emission features that dominate the near- and mid-infrared (NIR and MIR, respectively) spectra of galaxies, including prominent emission features that are produced by the stretching and bending vibrational modes of the C–C (6.2 $\mu$m, 7.7 $\mu$m) and C–H (3.3 $\mu$m, 11.3 $\mu$m) bonds in PAHs (Leger & D'Hendecourt 1985; Puget et al. 1985; Allamandola et al. 1989).[23] PAH emission has been detected from a wide variety of

[22] coolresearch.io

[23] A variety of alternative explanations for the carrier of the MIR bands can be found in the literature, including a number of materials with primarily hydrocarbon composition (see, e.g., Jones et al. 2013).

objects, including H II regions, planetary nebulae, young stellar objects, asymptotic giant branch stars, and in the ISM of dwarf, spiral, elliptical, and ultraluminous infrared galaxies (see Li 2020, and references within).

A key aspect of understanding the roles of PAHs in the ISM and using their emission as a tracer of galaxy properties is quantifying their abundance relative to the total dust grain population (Draine et al. 2007; Jones et al. 2015). Since PAHs are typically stochastically heated (Sellgren et al. 1983; Draine & Li 2001; Li & Draine 2001), and therefore respond linearly to the radiation field intensity, the fraction of the dust mass in the form of PAHs can be inferred from comparisons of the MIR PAH emission to the far-infrared (FIR) emission from dust in thermal equilibrium with the radiation field (e.g., Draine & Li 2007), given assumptions about the dust grain populations and radiation field strength and spectrum. Dust models in the literature make a variety of assumptions about the specific characteristics of the PAHs (or alternative small carbonaceous grain components), other small grains that contribute to the MIR emission, and the radiation field heating those grains (Draine & Li 2007; Compiègne et al. 2011; Jones et al. 2013, 2017; Galliano et al. 2021; Hensley & Draine 2023). Because all of these choices impact the MIR spectral energy distribution (SED), different models will produce different measurements of the PAH fraction and its variation. In the following, we adopt the Draine & Li (2007) dust model to guide our interpretation of the MIR SED and PAH fraction. This model does not have a variable "very small grain" (VSG) population and assumes a distribution of radiation field intensities heating the dust described by a delta function plus power-law component (Dale et al. 2001; Draine & Li 2007; Aniano et al. 2012). The fraction of the dust mass in the form of PAHs (with less than $10^3$ carbon atoms) in the Draine & Li (2007) model is denoted as $q_{\rm PAH}$.

Studies of local Universe galaxies (Li & Draine 2001; Weingartner & Draine 2001; Draine & Li 2007; Aniano et al. 2020) including the Large and Small Magellanic Clouds (LMC and SMC; Li & Draine 2002; Sandstrom et al. 2010; Paradis et al. 2011; Chastenet et al. 2019; Dale et al. 2023b; Paradis et al. 2023) have found $q_{\rm PAH}$ varies between approximately 0%–5%. The PAH fraction has been shown to decrease in low-metallicity galaxies (Engelbracht et al. 2005; Draine et al. 2007; Khramtsova et al. 2013; Rémy-Ruyer et al. 2015; Galliano et al. 2018; Chastenet et al. 2019; Aniano et al. 2020) and to fall dramatically within H II regions (Cesarsky et al. 1996; Chastenet et al. 2019). Tracing $q_{\rm PAH}$ across different environments allows for insights into where PAHs are being produced or destroyed and how they impact their surroundings. $q_{\rm PAH}$ measurements have, however, been limited in resolution and sample size due to the necessity of IR observations covering both PAH emission and FIR emission from larger dust grains.

An alternative approach to full MIR to FIR SED modeling is to trace the PAH fraction with ratios of PAH emission to small dust grain continuum emission in the MIR. Engelbracht et al. (2005) used Spitzer IRAC 8 $\mu$m and MIPS 24 $\mu$m measurements to show strong metallicity trends in PAH-to-continuum ratios, which were then validated with MIR Spitzer spectroscopy (Engelbracht et al. 2008). These MIR-only measurements have greatly expanded our view of PAHs in the ISM (see Li 2020, and references therein), and can be translated to use Wide-field Infrared Survey Explorer (WISE) 12 and 22 $\mu$m photometry for all nearby galaxies (though at lower resolution). However, they remain limited by the sensitivity and resolution of Spitzer, with a 6″ resolution at 24 $\mu$m, corresponding to ∼hundreds of parsecs in nearby galaxies. The sensitivity of Spitzer also made it difficult to trace PAH emission from the diffuse ISM. Yet, with the advent of the JWST, a new realm of environments for PAH studies are available.

Within its first year, JWST has already expanded our view of PAHs, detecting PAH emission at a distance of 100 pc from an actively accreting supermassive black hole (NGC 7469; Lai et al. 2022; Armus et al. 2023), in an extended disk around merging galaxies (VV 114; Evans et al. 2022), in the diffuse ISM of local star-forming galaxies (Leroy et al. 2023a; Sandstrom et al. 2023), tracing PAH emission up to $z = 2$ (Shivaei et al. 2024), and has tracked the properties of PAHs in stellar associations (Dale et al. 2023a) and star-forming regions (Egorov et al. 2023; Ujjwal et al. 2024). While JWST spectroscopy can provide precise details about the PAH population (see, e.g., Chown et al. 2024), the small field of view of both the MIRI integral field unit and NIRSpec make it observationally costly to study the distribution of PAHs in local Universe galaxies using JWST spectroscopy. Instead, MIRI and NIRCam photometric bands situated precisely on many of the strongest PAH features at $z \sim 0$ can be used as indicators of PAH emission across the disks of nearby galaxies. Following the work of Chastenet et al. (2023a) and Egorov et al. (2023), this paper presents an analysis of a proposed photometrically derived tracer of the fraction of dust stored in PAHs using three of the MIRI filters: F770W, F1130W, and F2100W.

Tracing PAHs in the ISM of nearby galaxies with JWST will help address many outstanding questions surrounding these small dust grains. Understanding the formation and destruction mechanisms of the PAHs across ISM phases and galaxy environments will provide context for using PAH emission as a tracer of star formation rate (SFR; e.g., Peeters et al. 2004; Calzetti et al. 2007; Shipley et al. 2016; Whitcomb et al. 2020; Belfiore et al. 2023) or gas column density (e.g., Cortzen et al. 2019; Leroy et al. 2023b; Whitcomb et al. 2023a) and will help to clarify why $q_{\rm PAH}$ decreases at low metallicity (e.g., Aniano et al. 2020). Previous work with Spitzer has already provided clues into the complex life cycle of the PAHs, showing suppression of $q_{\rm PAH}$ in regions with warm dust measured by increased $\nu L_\nu(70\,\mu{\rm m})/L_{\rm TIR}$ values (Aniano et al. 2020), implying that PAHs are destroyed in regions surrounding young stars. This was further confirmed in Chastenet et al. (2019) and Chastenet et al. (2023a), both of which show decreasing PAH fractions in H II regions in the LMC, and initial work on four of the galaxies from the Physics at High Angular Resolution in Nearby GalaxieS (PHANGS) sample, respectively.

Using the 19 galaxies observed by JWST as part of the PHANGS-JWST Cycle 1 Treasury (Lee et al. 2023; Williams et al. 2024), along with additional multiwavelength observations, we examine how galaxy environment, specific star formation rate (sSFR), and ISM conditions impact the PAH fraction at spatial scales of 10–100 pc.

This paper is organized as follows. Section 2 describes the observations used to complete this analysis. Section 3 provides a justification for the proposed photometric tracer of the PAH fraction. Section 4 uses this tracer to map the distribution of PAHs within our sample, and describes trends seen as a function of environment, gas phase, metallicity, and proximity

**Table 1**
Galaxy Sample

| Target | $\log_{10}M_{\star,g}$ ($M_\odot$) | $\log_{10}M_{\star,JWST}$ ($M_\odot$) | $\log_{10}SFR_{JWST}$ ($M_\odot$ yr$^{-1}$) | Distance (Mpc) | P.A. (deg) | $i$ (deg) | $r_{25}$ (arcmin) | H I Map | MUSE Res. (arcsec) |
|---|---|---|---|---|---|---|---|---|---|
| IC 5332 | 9.68 | 9.20 | −1.30 | 9.01 | 74.4 | 26.9 | 3.0 | MeerKAT | 0.87 |
| NGC 0628 | 10.34 | 10.08 | −0.35 | 9.84 | 20.7 | 8.9 | 4.9 | VLA | 0.92 |
| NGC 1087 | 9.94 | 9.94 | 0.26 | 15.85 | 359.1 | 42.9 | 1.5 | VLA | 0.92 |
| NGC 1300 | 10.62 | 10.62 | −0.08 | 18.99 | 278.0 | 31.8 | 3.0 | MeerKAT | 0.89 |
| NGC 1365 | 11.00 | 10.92 | 0.35 | 19.57 | 201.1 | 55.4 | 6.01 | ⋯ | 1.15 |
| NGC 1385 | 9.98 | 9.98 | 0.44 | 17.22 | 181.3 | 44.0 | 1.7 | VLA | 0.77 |
| NGC 1433 | 10.87 | 10.83 | −0.25 | 18.63 | 199.7 | 28.9 | 3.1 | ⋯ | 0.91 |
| NGC 1512 | 10.72 | 10.71 | −0.19 | 18.83 | 261.9 | 42.5 | 4.2 | MeerKAT | 1.25 |
| NGC 1566 | 10.79 | 10.78 | 0.50 | 17.69 | 214.7 | 29.5 | 3.6 | ⋯ | 0.80 |
| NGC 1672 | 10.73 | 10.73 | 0.79 | 19.40 | 134.3 | 43.6 | 3.1 | ⋯ | 0.96 |
| NGC 2835 | 10.00 | 9.87 | −0.27 | 12.22 | 1.0 | 41.3 | 3.2 | VLA | 1.15 |
| NGC 3351 | 10.37 | 10.37 | −0.24 | 9.96 | 193.2 | 45.1 | 3.6 | VLA | 1.05 |
| NGC 3627 | 10.84 | 10.84 | 0.71 | 11.32 | 173.1 | 57.3 | 5.1 | VLA | 1.05 |
| NGC 4254 | 10.42 | 10.42 | 0.52 | 13.10 | 68.1 | 34.4 | 2.5 | VLA | 0.89 |
| NGC 4303 | 10.51 | 10.51 | 0.69 | 16.99 | 312.4 | 23.5 | 3.4 | VLA | 0.78 |
| NGC 4321 | 10.75 | 10.75 | 0.48 | 15.21 | 156.2 | 38.5 | 3.0 | VLA | 1.16 |
| NGC 4535 | 10.54 | 10.47 | −0.01 | 15.77 | 179.7 | 44.7 | 4.1 | MeerKAT | 0.56 |
| NGC 5068 | 9.41 | 9.27 | −0.74 | 5.20 | 342.4 | 35.7 | 3.7 | VLA | 1.04 |
| NGC 7496 | 10.00 | 10.00 | −0.29 | 18.72 | 193.7 | 35.9 | 1.7 | MeerKAT | 0.89 |

**Notes.** Global stellar masses ($M_{\star,g}$) from Leroy et al. (2021b) as well as the stellar mass ($M_{\star,JWST}$) and SFR ($SFR_{JWST}$) measured within the area of the galaxy mapped by JWST. SFR measurements are made using the extinction-corrected H$\alpha$ measurements from Belfiore et al. (2023). $r_{25}$ radius is given in arcminutes from the HyperLeda database (Makarov et al. 2014). Distances are from Anand et al. (2021). Position angles and inclinations are from Leroy et al. (2012). The H I map column lists the origin of the H I data, and the "MUSE Res." column displays the final "copt" resolution of the MUSE data (see Section 2.3 for details). Additional information can be found in Table 1 of the survey paper (Lee et al. 2023).

to sites of active star formation. Section 5 situates the results of this paper in the broader astronomical context. Finally, Section 6 summarizes the conclusions drawn from this analysis.

## 2. Data and Methods

The galaxies included in this study are all part of the PHANGS-JWST Cycle 1 sample (Lee et al. 2023; Williams et al. 2024). This survey includes observations of 19 galaxies in four NIRCam and four MIRI bands. Information about the 19 galaxies can be found in Table 1. The 19 galaxies included in the PHANGS-JWST sample are all nearby ($D \lesssim 20$ Mpc) and all have relatively low inclinations ($i \leqslant 60°$). All are star-forming galaxies, with metallicities spanning $12 + \log_{10}(O/H) = 8.4$–$8.7$ (Groves et al. 2023) and stellar masses between $\log_{10}(M_\star/M_\odot) = 9.5$–$11.1$ (Leroy et al. 2021b). The galaxies included in this sample include a range of morphologies and a subset that host active galactic nuclei (AGNs).

### 2.1. JWST MIRI and NIRCam

This work uses data from three of the MIRI bands, F770W, F1130W, and F2100W (Rieke et al. 2015), as well as the NIRCam F200W. The MIRI F770W and F1130W filters capture the emission from two of the strongest PAH features, the 7.7 and 11.3 $\mu$m features. The F2100W filter is dominated by dust continuum emission. As an example, the F770W and F2100W maps of NGC 4303 are shown in Figure 1. The NIRCam F200W filter primarily covers stellar emission and is therefore used to remove starlight from the F770W data (see Section 3.1).

Each target was covered by small one- to four-pointing mosaics, chosen to maximize the overlap with the available optical and millimeter spectroscopy and cover the majority ($\geqslant$70%) of star formation activity traced by MIR emission in each galaxy (defined by a contour of 0.5 MJy sr$^{-1}$ at WISE 12 $\mu$m). Details of the data processing are described in Williams et al. (2024). Briefly, JWST data are reduced using the most up-to-date calibration reference data system context (jwst_1201), and JWST calibration pipeline version v1.13.4, and the PHANGS-JWST data version 1.1.0. In addition to the calibration pipeline, the background level in each filter is matched to existing wide-field Spitzer or WISE data that extend off of the galaxy, as discussed in Leroy et al. (2023b). The JWST data are finally all convolved to a common Gaussian resolution of 0.″90, a resolution slightly larger than the F2100W beam, to improve signal-to-noise at F2100W and match the resolution of existing multiwavelength data (see discussion in Williams et al. 2024). This corresponds to only a moderate decrease in resolution (native resolution of 0.″67 at F2100W, the largest of this filter set) but greatly improves the signal-to-noise, as the noise in these filters is pixel based rather than resolution element based. The convolution was implemented using the method described in Aniano et al. (2011), using the WebbPSF models to generate kernels.[24,25] The pixel scale is left at the original pixel scale of 0.″11, which oversamples the point-spread function (PSF), but this does not affect the analysis presented in this paper.

A 3$\sigma$ signal-to-noise cut is performed on each MIRI filter used in this work. We determine the typical noise by finding empty sky regions in a subset of the maps that were large enough to include areas off the galaxy. This was possible for NGC 1087, NGC 1385, NGC 1433, NGC 1512, NGC 1566, and NGC 7496. The 1$\sigma$ level was determined as the average of the standard deviations of the sky regions found in these six

[24] https://stsci.app.box.com/v/jwst-simulated-psf-library
[25] https://github.com/francbelf/jwst_kernels

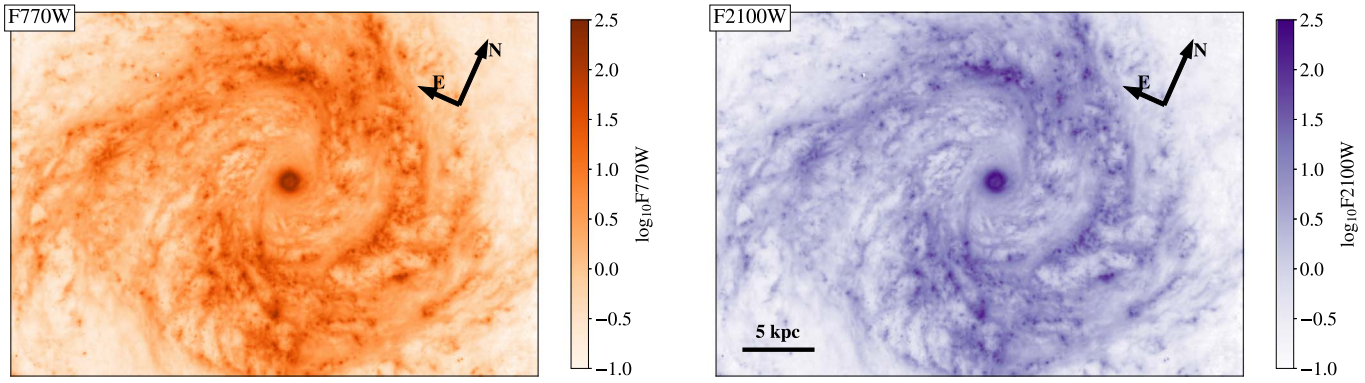


**Figure 1.** NGC 4303 in F770W (left) and F2100W (right). F770W and F2100W intensities are both shown in log scale to capture the full dynamic range, and F770W has been corrected to remove starlight emission (see Section 3.1 for details). The $R_{\rm PAH}$ map of NGC 4303 is shown in Figure 2. The observed emission in F770W and F2100W over large parts of the galaxy look very similar, indicating that $R_{\rm PAH}$ does not change substantially in the diffuse neutral gas. The ratio map shown in Figure 2 reveals that in the bright, compact H II regions, $R_{\rm PAH}$ drops steeply.

maps. All background regions showed similar standard deviations and median values. With this method, our $3\sigma$ limits are 0.09 MJy sr$^{-1}$ in F770W, 0.13 MJy sr$^{-1}$ in F1130W, and 0.29 MJy sr$^{-1}$ in F2100W. These values are in good agreement with the characterization of noise levels presented in Williams et al. (2024) and match well with the expected values from convolving the pipeline-generated error maps. Additionally, several of the nuclei in our sample saturated in F2100W, producing diffraction spikes across the maps. By-eye masking is done to exclude regions where these spikes contaminate the maps. In convolving to lower resolution, we also convolve the spike masks and use them to conservatively exclude any contaminated pixels by removing all pixels where the convolved mask has a value greater than 0.9.

### 2.2. z0MGs Dust Maps

In order to assess the combination of JWST bands as tracers of dust properties, we compare the JWST data to the results of MIR-to-FIR SED fitting to the Draine & Li (2007) dust models produced as part of the $z = 0$ Multiwavelength Galaxy Synthesis program (z0MGs; Leroy et al. 2019; Chastenet et al. 2021; J. Chastenet et al. 2024, in preparation). The results of the Draine & Li (2007) model fitting include maps of $q_{\rm PAH}$, which we use to calibrate our JWST photometric measurement of the PAH fraction, $R_{\rm PAH}$. These fit results were produced using a combination of WISE and Herschel Space Observatory data and the Draine & Li (2007) dust models (using the DustBFF code; Gordon et al. 2014).

### 2.3. Ancillary Data

In addition to the IR data, we use ancillary data products to determine the gas and stellar properties of the galaxies in our sample. These include $^{12}$CO (2–1) moment 0 maps from PHANGS-ALMA (Leroy et al. 2021a, 2021b), H$\alpha$ maps from PHANGS-MUSE (Emsellem et al. 2022), and H I maps from several Very Large Array (VLA) projects including THINGS (Walter et al. 2008) or MeerKAT (Sun et al. 2022), depending on data availability. MeerKAT H I maps are used in instances where both VLA and MeerKAT data are available.

The sources of the H I maps are listed in Table 1. These maps have resolutions ranging from 11″ to 15″, and are left at their native resolutions for our analysis. While the typical H I resolution is much larger than the other maps used in this work, the smoothness and flatness of the atomic gas profile observed in the Milky Way (MW) and other galaxies suggests that convolution to matched resolutions will not greatly impact our comparisons (Schruba et al. 2011; Bigiel & Blitz 2012; Leroy et al. 2013; Wong et al. 2013). The H I intensities are converted to atomic gas densities including helium and assuming optically thin H I gas, using the equation $\Sigma_{\rm HI}$ [$M_\odot$ pc$^{-2}$] = 0.020$I_{\rm HI}$ [K km s$^{-1}$].

The $^{12}$CO (2–1) moment 0 maps were observed with the Atacama Large Millimeter/submillimeter Array (ALMA) using the 12 m, 7 m, and total power array, producing maps with $\sim$1″ resolution (Leroy et al. 2021b). The $^{12}$CO (2–1) intensities were converted to a molecular gas surface density using a constant $\alpha_{\rm CO,1-0}$ of 4.35 $M_\odot$ pc$^{-2}$ (K km s$^{-1}$)$^{-1}$ and a $^{12}$CO (2–1)/ $^{12}$CO(1–0) line ratio $R_{21} = 0.65$ (Leroy et al. 2021b; den Brok et al. 2022). For this work, we require only a coarse estimate of the molecular gas surface density and so neglect conversion factor variations due to metallicity effects, excitation variations, and opacity variations. We use the broad moment 0 masks, which maximize the $^{12}$CO (2–1) emission included in the moment 0 maps, and which are further described in Leroy et al. (2021b).

H$\alpha$ maps were obtained from the PHANGS-MUSE data (Emsellem et al. 2022) for all 19 galaxies. For this work, we use the convolved–optimized ("copt") resolution maps. The copt resolution provides a uniform PSF for all MUSE data for a single galaxy using the broadest PSF for all observations. Resolutions for each MUSE map are listed in Table 1. The H$\alpha$ line was fit using the `pPXF` tool to fit the stellar continuum (including H$\alpha$ absorption) and a Gaussian profile for each spaxel. Further discussion of the MUSE data products can be found in Emsellem et al. (2022). In general, the MUSE copt resolutions are very similar to or slightly larger than the 0.″9 resolution of the convolved F2100W data. We do not do any additional steps of resolution matching, since we primarily rely on the nebular catalog for our analysis, as described below.

### 2.4. PHANGS Data Products

In addition to the maps described above, we rely on several of the PHANGS higher-order data products to distinguish between environments and compare to physical properties in individual regions. These data products are described below.

H II regions are identified based on the catalogs compiled by Santoro et al. (2022) and further described in Groves et al. (2023). These nebular region catalogs were produced using the

Hα maps from the PHANGS-MUSE survey (described above) and the HIIPhot algorithm for segmentation described in Thilker et al. (2000). Below, we distinguish between $R_{\rm PAH}$ inside ($R_{\rm PAH,Neb}$) and outside ($R_{\rm PAH,Diffuse}$) of these nebular regions. When we do so, we include all nebular regions in the catalogs, which are mostly H II regions but also include some other nebular regions like supernova remnants.

Metallicity maps for each galaxy were produced in Williams et al. (2022). These maps were created with the MUSE data described above (Emsellem et al. 2022) and the Pilyugin & Grebel (2016) S calibration, which relies on the relative strengths of the Hβ, [O III]λ5007, [N II]λ6584, and [S II] λ6717 + 6731 emission lines. All lines were corrected for dust extinction using the Balmer decrement before the metallicity was calculated. The Williams et al. (2022) metallicity maps interpolate between H II-region metallicities using Gaussian process regression, yielding a fully sampled metallicity map for each galaxy.

We also use the environmental maps from Querejeta et al. (2021) to isolate morphological environments within each galaxy. These maps were created with the Spitzer 3.6 μm images and primarily distinguish between centers, bars, spiral arms, interarm disks, and disks without strong spiral arms.

Finally, we use the extinction-corrected Hα SFR and stellar mass ($M_\star$) maps produced by Belfiore et al. (2023). These maps were produced using the integral field spectroscopy from the PHANGS-MUSE survey (Emsellem et al. 2022). The Hα measurements are corrected for attenuation using an $E(B-V)$ determined based on the measured Balmer decrement across the maps. Stellar masses were determined using Voronoi binning of the MUSE data cubes and full-spectral fitting using the pPXF tool (Cappellari & Emsellem 2004), as described in Emsellem et al. (2022, their Section 5.2.4).

### 2.5. Methods

To test trends in the PAH distribution, we examine the MIRI data from each galaxy on three scales: pixel by pixel, in circular regions with radii of 1 kpc spaced using a hexagonal grid to evenly sample the full MIRI maps, and the average of each band across the full maps. The pixel-by-pixel trends leverage the resolution of JWST and are the finest statistical sample available with this data set. Because we are also interested in how large-scale environment affects $R_{\rm PAH}$ (e.g., $\Sigma_\star$, $\Sigma_{\rm SFR}$, sSFR) we also use larger (1 kpc) regions. Within each 1 kpc region, we record the values of $R_{\rm PAH}$ in the nebular regions ($R_{\rm PAH,Neb}$) and diffuse gas ($R_{\rm PAH,Diffuse}$), and also note that this cannot be done pixel by pixel, as each pixel can only be in either a nebular region or a diffuse region. Finally, in using the full maps, we determine how integrated galaxy properties might enhance or decrease the PAH fraction. These integrated diagnostics also provide the most direct comparison to higher-redshift measurements of PAHs, which will primarily yield galaxy-integrated PAH data.

## 3. Defining $R_{\rm PAH}$

Work by Engelbracht et al. (2005), Wu et al. (2006), and Engelbracht et al. (2008) showed the utility of MIR photometric tracers of PAH fraction with Spitzer data. In order to leverage the increased resolution of JWST to efficiently map the PAH fraction in a wide range of environments, we propose to update previous Spitzer-based photometric tracers of $q_{\rm PAH}$ with MIRI photometric bands. Previous studies with Spitzer have shown 8 μm/24 μm from the IRAC4 and MIPS1 bands, respectively, is a good indicator of the PAH fraction (Engelbracht et al. 2005, 2008; Smith et al. 2007; Marble et al. 2010; Croxall et al. 2012). With the narrower MIRI filters, we can improve upon this indicator by including both the 7.7 μm and 11.3 μm PAH features (F770W and F1130W) in place of IRAC4 and replacing the MIPS1 24 μm emission with F2100W. Just like the PAH emission features, the 21 μm continuum is often produced by stochastic heating events, though in regions of high radiation field intensity it can include a contribution from small grains in equilibrium with the radiation field. In the case where all three filters are dominated by stochastically heated dust emission, almost any dependence of $R_{\rm PAH}$ on the interstellar radiation field (ISRF) will be removed (Draine & Li 2007; Chastenet et al. 2023a). This is further explored in Appendix C, where we use the Draine et al. (2021) dust models to explore variations in predicted $R_{\rm PAH}$ for different ISRFs. Although it is possible that changes in the ISRF could slightly shift the measured $R_{\rm PAH}$, on the 10–50 kpc scales we are measuring this should not be the dominant effect. As we discuss below, current evidence suggests that almost all of our data will lie in or near this regime where all three bands are dominated by stochastic heating.

Based on the work done in Chastenet et al. (2023a) and Egorov et al. (2023), we define our photometric tracer $R_{\rm PAH}$ as

$$R_{\rm PAH} = \frac{\rm F770W_{ss} + F1130W}{\rm F2100W},$$

where F1130W and F2100W are the surface brightness in the MIRI bands measured in megajanskys per steradian and $\rm F770W_{ss}$ is the surface brightness in the F770W band with a starlight subtraction (see Section 3.1). As the F770W and F1130W bands include two of the strongest PAH features (the 7.7 μm and 11.3 μm features, respectively), they are used as a proxy for total PAH emission. We normalize by the F2100W band, which includes a significant contribution from non-PAH, small dust grain continuum emission. $R_{\rm PAH}$ is thus the ratio of PAH emission to other small grain emission, providing a high-spatial-resolution estimation of the PAH fraction without costly spectroscopy. An example of a map of $R_{\rm PAH}$ in NGC 4303 is shown in Figure 2, with environments (yellow, nucleus; pink, bar; cyan, spiral arms) and nebular regions (light green) indicated with colored contours.

We will use $R_{\rm PAH}$ as a tracer of the PAH fraction. That interpretation relies on several assumptions: (i) the F770W and F1130W bands are dominated by PAH emission where PAHs are present, (ii) that the combination of the 7.7 μm and 11.3 μm feature strengths is a good indicator of the total PAH emission, (iii) that the F2100W band includes a contribution from non-PAH dust continuum sufficient to give leverage on the PAH-to-continuum ratio, and (iv) the MIR emission spectrum is primarily altered by the PAH fraction, or that any other effects altering the ratio (e.g., increases in the radiation field intensity) are covariant with changes in the PAH fraction and do not undermine the correlation between $R_{\rm PAH}$ and $q_{\rm PAH}$.

These assumptions all have clear evidence in their support. (i) Observations and dust-emission models show that when PAHs are present and illuminated by typical ISRF intensities and spectra their emission dominates the F770W and F1130W filters (see spectral decomposition of MIR spectra from

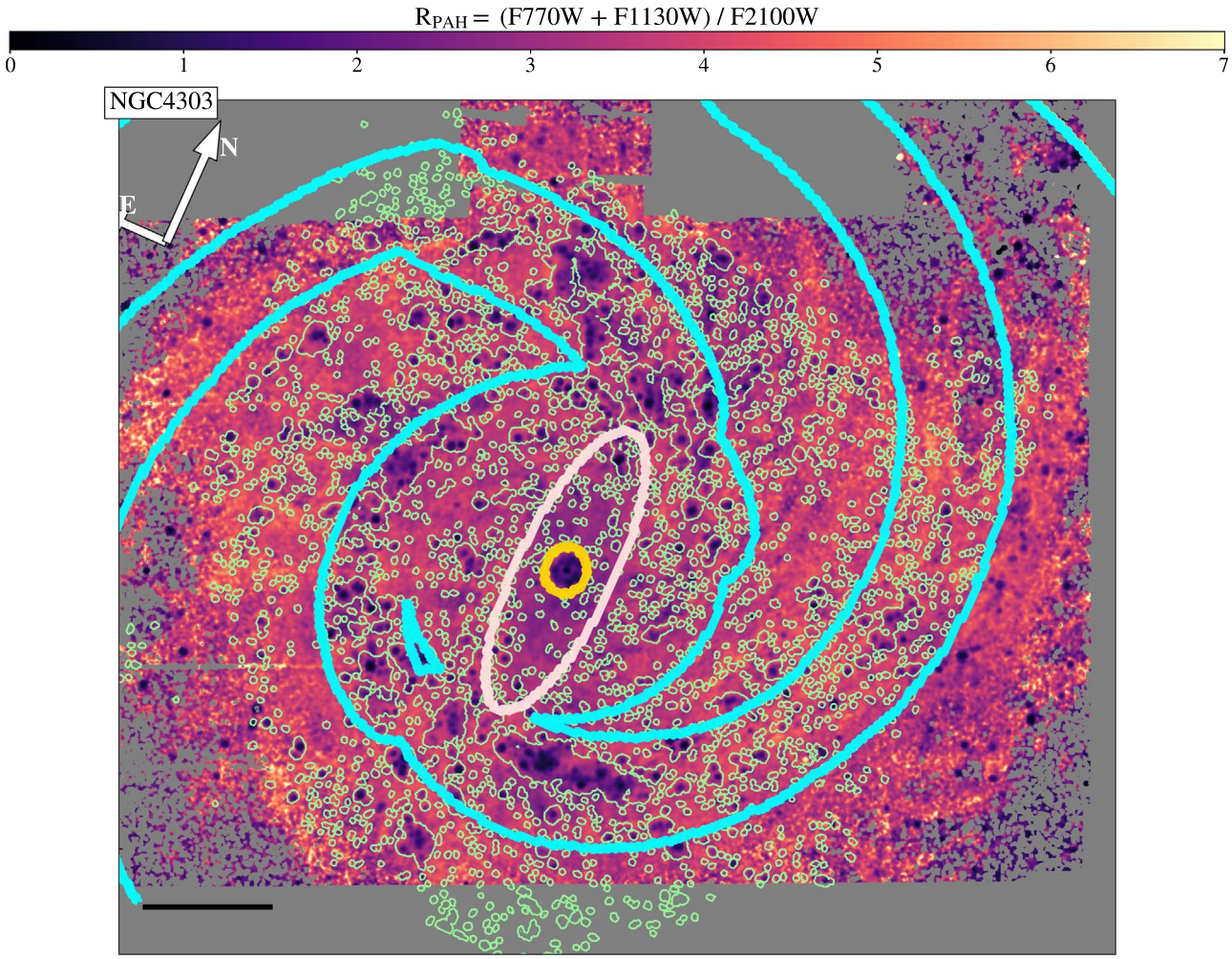


**Figure 2.** $R_{PAH}$ mapped in NGC 4303, with the F770W star subtraction described in Section 3.1 completed before incorporation of the F770W into the $R_{PAH}$ map. Yellow, pink, and blue contours show the location of the nucleus, bar, and spiral arms, respectively, as defined by the maps from Querejeta et al. (2021). Light green contours show the locations of the nebular regions from the PHANGS-MUSE nebular catalogs (Santoro et al. 2022; Groves et al. 2023). The black bar on the bottom left represents a scale of 5 kpc. Maps have been smoothed to $0\farcs9$ to increase the signal-to-noise.

Whitcomb et al. 2023b). In cases where there is low ISM column relative to stellar mass surface density (e.g., central bulges of galaxies), the F770W filter can have a significant contribution from starlight, which we will correct for (see further discussion in Section 3.1). (ii) Models of PAH emission show that in a typical ISRF, the 7.7 $\mu$m emission is produced primarily by charged PAHs and the 11.3 $\mu$m feature by neutral PAHs, and the sum of both provides a robust tracer of PAH emission regardless of the ionization state of the PAHs (Draine & Li 2007; Smith et al. 2007; Draine et al. 2021). (iii) The ratio of (F770W+F1130W)/F2100W traces the PAH fraction in data and in dust-emission models in such a way that even with varying radiation field intensity and $q_{PAH}$ the F2100W provides sufficient leverage on dust continuum emission in comparison to PAH emission (see Section 3.2 for more detailed analysis; Draine et al. 2021; Hensley & Draine 2023). (iv) Finally, over the range of radiation field intensities relevant for the 10–50 pc resolution of our observations, the Draine & Li (2007) models of dust emission do not show substantial changes to $R_{PAH}$ related to radiation field intensity. We will discuss this point in more detail in Appendix E. Changing the radiation field spectrum can alter the relationship between $q_{PAH}$ and $R_{PAH}$, in the sense that harder spectra produce more PAH emission for a given PAH surface density (Draine et al. 2021). This means that in regions with harder radiation fields, our $R_{PAH}$ tracer may suggest higher $q_{PAH}$. Since our primary observation is a decrease in $R_{PAH}$ toward regions of recent star formation, this effect would strengthen our conclusions. We also investigate $R_{PAH}$ diagnostics using only F770W/F2100W and only F1130W/F2100W. These are described in Appendix B, where we find that using only one PAH tracing band can provide a viable alternative tracer of PAH fraction, although both alternatives have the potential to confuse changes in the PAH fraction with changes in the size, ionization state, and heating of the PAHs (Draine et al. 2021).

Maps of $R_{PAH}$ for the complete sample are shown in Figures 2 and 3. A 5 kpc scale bar has been placed in the lower left of each image, and all images have the same linear scaling for $R_{PAH}$. In instances where an AGN saturated the center (NGC 1365, NGC 4535, and NGC 7496), masks have been placed to remove the affected pixels. Galaxies have been rotated for ease of display. The average $R_{PAH}$ values for each galaxy as well as for isolated environments are listed in Table 2.

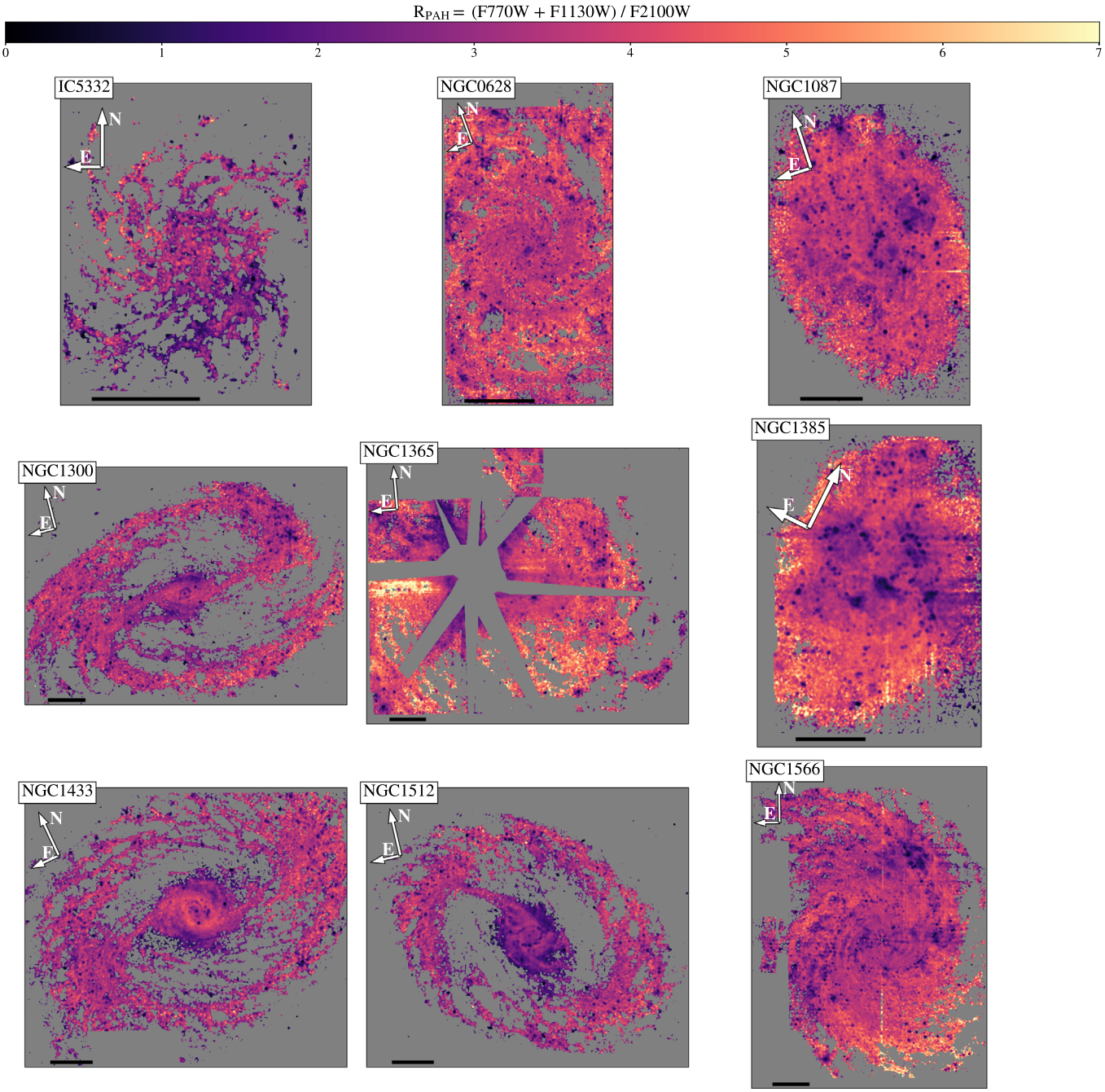


**Figure 3.** $R_{\rm PAH}$ mapped in 9 of the 18 galaxies included in this work. See Figures 3 and 2 for the other targets. Pixels below the $3\sigma$ noise limit are cut, and shown in gray. Additional by-eye masking is done on galaxies where a bright nucleus is saturated in F2100W, creating diffraction spikes, which are cut for our analysis. Black bars in the lower-left corner of each image represent 5 kpc in each source. Each galaxy has been rotated to better fill the space; arrows showing the north and east directions are displayed in the upper left of each panel. Maps have been smoothed to $0\farcs9$ to increase the signal-to-noise. The starlight subtraction method described in Section 3.1 was performed on the F770W fluxes before producing these $R_{\rm PAH}$ maps.

### 3.1. Starlight Subtraction

In rare cases in the PHANGS sample where there is low dust column relative to the stellar surface density (e.g., in some galactic bulges) and/or a very low PAH fraction, the F770W band can have a significant contribution from starlight. F1130W is at a long enough wavelength where the contribution from starlight will always be minimal. To demonstrate this, we show two SED models produced using the Code for Investigating GALaxy Emission (CIGALE; Boquien et al. 2019) in Figure 4. In one model, the PAH fraction is set to a relatively high value of $q_{\rm PAH} = 6.63\%$ (solid lines), while in the other model the PAH fraction is set to a low value of $q_{\rm PAH} = 0.47\%$ (dashed lines). The red and black lines represent the dust and total emission, respectively. Both models assume the same stellar population, with the unattenuated starlight from this population shown as the solid purple line. In the case of the low-PAH fraction model (or in the case of a model with the same $q_{\rm PAH}$ but a far lower dust column density), it is clear that the F770W MIRI filter will have a substantial contribution from starlight.

In order to remove contributions from starlight from the F770W photometry, we scale the NIRCam F200W maps to

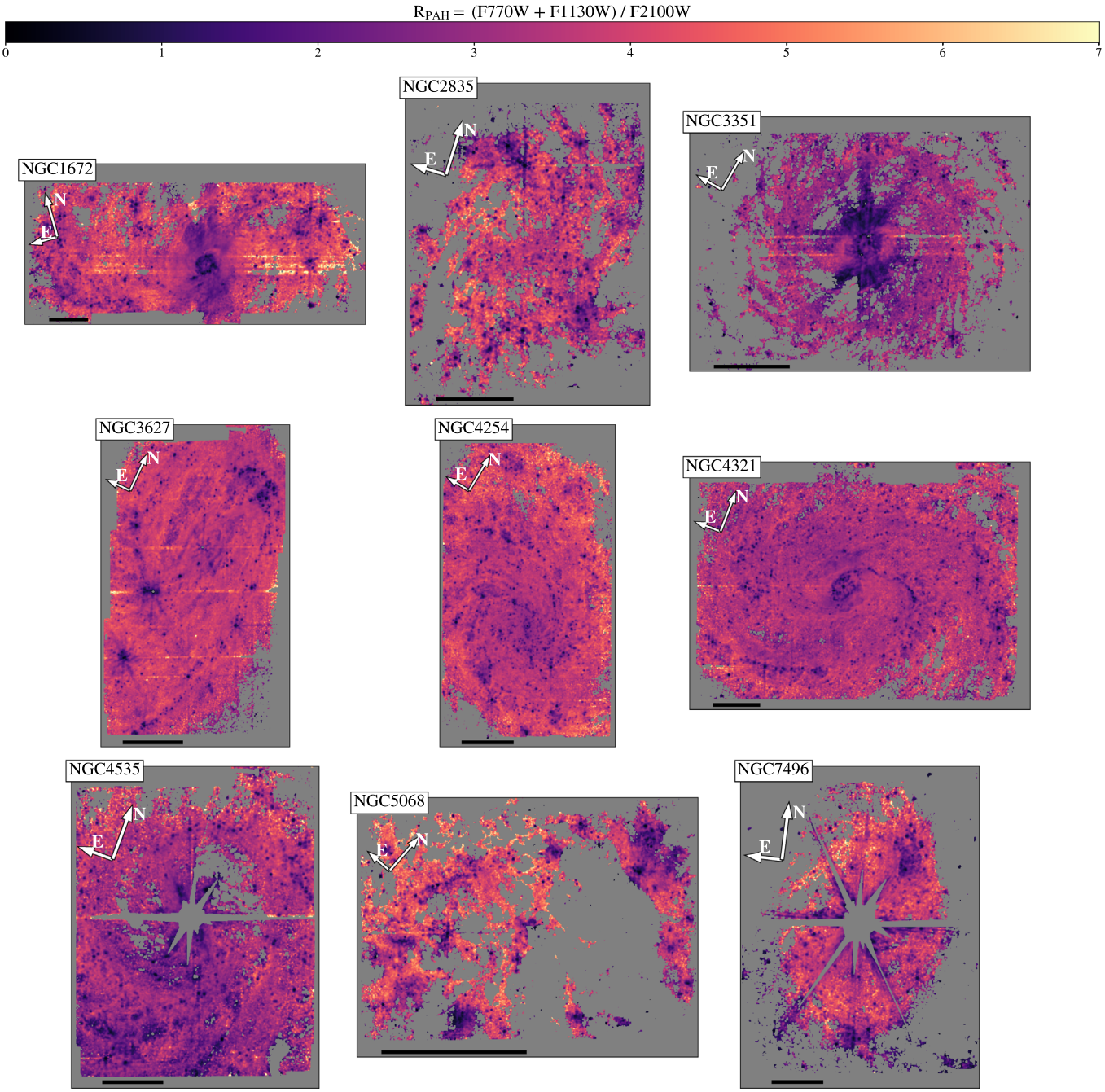


**Figure 3.** (Continued.)

predict the amount of starlight in the F770W band, following a similar procedure to what was done by Helou et al. (2004) using Spitzer 3.6 $\mu$m (see also Draine et al. 2007; Dale et al. 2009). We use a ratio of $F770W_{starlight}/F200W = 0.13 \pm 0.04$, determined from a range of reasonable stellar emission models with ages spanning 0.5–13 Gyr, a later burst of star formation, and the Chabrier (2003) initial mass function. In general, the results are fairly insensitive to the details of the stellar populations (see also Appendix B of Ciesla et al. 2014, for a detailed investigation). These starlight models are also assumed to experience attenuation following Calzetti et al. (2000). Dust emission is set using the Draine et al. (2014) models, with the available range of $q_{PAH}$. CIGALE does not couple the attenuation curve and $q_{PAH}$ assumption. It assumes an energy balance, so all light attenuated in the optical and UV is reemitted in the IR. CIGALE does not adjust the 2175 Å feature when $q_{PAH}$ changes, but for energy balance to be maintained the integral of the IR SED will impact the level of attenuation applied to the starlight. The stellar emission models are produced using CIGALE (Boquien et al. 2019), with all additional properties held constant using the default CIGALE settings. Synthetic photometry is performed on each stellar emission model to determine the relative fluxes in the F770W and the attenuated stellar emission model to determine the flux in the F200W bands. We use the F200W band to correct for starlight instead of the F300M due to the higher signal-to-noise

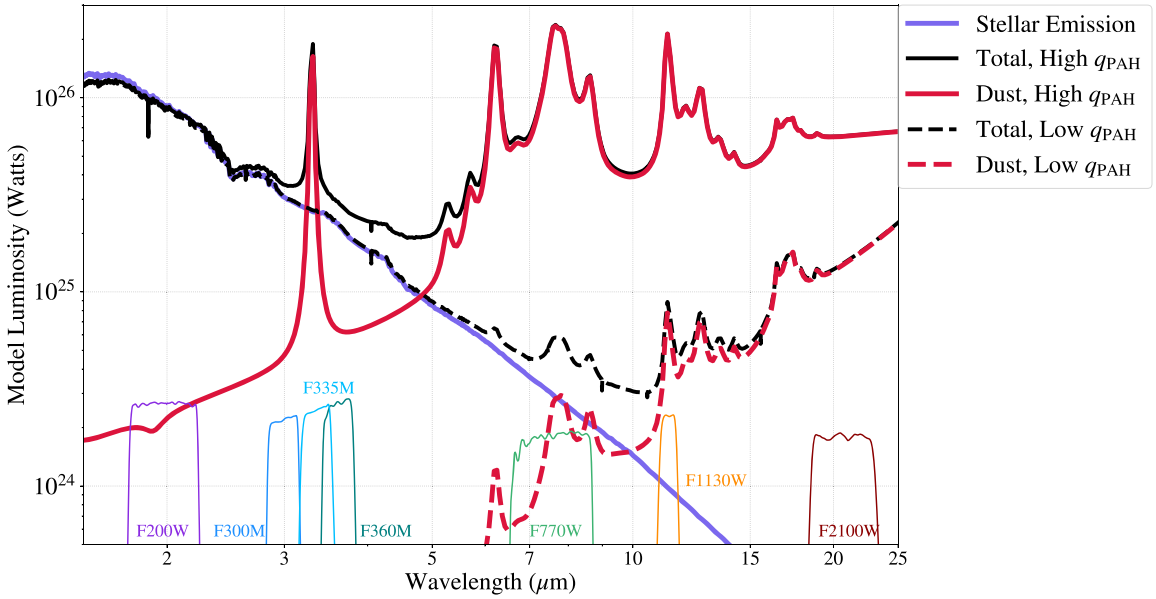


**Figure 4.** Two models of MIR emission compiled using CIGALE. Solid (high PAH content) and dashed (low PAH content) red lines represent the dust emission, while the solid and dashed black lines represent the total luminosity. The same stellar radiation field was used in both models, and is shown as a solid blue line. The filter profiles for a subset of the JWST filters are shown along the $x$-axis, for reference.

**Table 2**
Average $R_{PAH}$ Values across Environments

| Target | $\langle R_{PAH} \rangle$ | $\langle R_{PAH,Diff.} \rangle$ | $\langle R_{PAH,Neb.} \rangle$ | $\langle R_{PAH,Nuc.} \rangle$ | $\langle R_{PAH,Bar} \rangle$ | $\langle R_{PAH,Arms} \rangle$ | $\langle R_{PAH,IA} \rangle$ | $\langle R_{PAH,Disk} \rangle$ |
|---|---|---|---|---|---|---|---|---|
| IC 5332 | $2.53^{3.62}_{1.42}$ | $2.54^{3.64}_{1.43}$ | $2.57^{3.60}_{1.47}$ | $3.26^{3.89}_{2.28}$ | … | … | … | $2.51^{3.61}_{1.42}$ |
| NGC 0628 | $3.68^{4.45}_{2.79}$ | $3.72^{4.50}_{2.84}$ | $3.56^{4.28}_{2.66}$ | $3.41^{3.84}_{2.88}$ | … | $3.70^{4.43}_{2.85}$ | $3.72^{4.55}_{2.72}$ | … |
| NGC 1087 | $3.47^{4.16}_{2.45}$ | $3.55^{4.23}_{2.53}$ | $3.25^{3.92}_{2.34}$ | … | $3.21^{3.66}_{2.43}$ | … | … | $3.51^{4.18}_{2.55}$ |
| NGC 1300 | $2.99^{3.83}_{1.99}$ | $2.97^{3.83}_{1.96}$ | $3.10^{3.82}_{2.21}$ | $3.14^{3.64}_{2.34}$ | $2.84^{3.57}_{1.88}$ | $3.26^{4.05}_{2.40}$ | $2.78^{3.75}_{1.79}$ | … |
| NGC 1365 | $3.85^{4.95}_{2.70}$ | $3.91^{5.01}_{2.78}$ | $3.60^{4.63}_{2.41}$ | $2.79^{3.00}_{2.49}$ | $3.77^{4.71}_{2.84}$ | $3.73^{4.48}_{2.77}$ | $3.92^{5.07}_{2.64}$ | … |
| NGC 1385 | $3.59^{4.56}_{2.56}$ | $3.76^{4.69}_{2.80}$ | $3.14^{4.12}_{2.17}$ | … | … | $3.74^{4.70}_{2.62}$ | $3.55^{4.49}_{2.54}$ | … |
| NGC 1433 | $2.89^{3.77}_{1.80}$ | $2.85^{3.76}_{1.76}$ | $3.08^{3.83}_{2.17}$ | $3.52^{4.13}_{2.73}$ | $2.74^{3.62}_{1.62}$ | … | … | $2.91^{3.79}_{1.84}$ |
| NGC 1512 | $2.81^{3.73}_{1.75}$ | $2.76^{3.71}_{1.70}$ | $3.05^{3.81}_{2.17}$ | $2.72^{3.13}_{2.06}$ | $2.29^{3.22}_{1.37}$ | $3.07^{3.85}_{2.13}$ | $2.85^{3.85}_{1.77}$ | … |
| NGC 1566 | $3.41^{4.19}_{2.45}$ | $3.44^{4.20}_{2.53}$ | $3.27^{3.97}_{2.31}$ | $2.48^{3.51}_{1.65}$ | $3.22^{3.62}_{2.60}$ | $3.43^{4.15}_{2.47}$ | $3.44^{4.28}_{2.44}$ | … |
| NCG 1672 | $3.57^{4.40}_{2.56}$ | $3.65^{4.47}_{2.68}$ | $3.31^{4.14}_{2.26}$ | $1.77^{2.49}_{1.11}$ | $3.43^{4.20}_{2.56}$ | $3.70^{4.45}_{2.89}$ | $3.64^{4.50}_{2.57}$ | … |
| NGC 2835 | $3.37^{4.29}_{2.22}$ | $3.49^{4.38}_{2.34}$ | $3.14^{4.05}_{2.07}$ | $3.52^{3.95}_{3.11}$ | $3.48^{3.98}_{2.88}$ | $3.33^{4.23}_{2.15}$ | $3.37^{4.37}_{2.20}$ | … |
| NGC 3351 | $2.77^{3.47}_{1.84}$ | $2.79^{3.48}_{1.89}$ | $2.84^{3.48}_{1.96}$ | $1.73^{2.24}_{1.22}$ | $2.35^{3.23}_{1.33}$ | … | … | $2.84^{3.52}_{2.02}$ |
| NGC 3627 | $3.60^{4.06}_{2.96}$ | $3.68^{4.08}_{3.21}$ | $3.39^{3.90}_{2.53}$ | $3.11^{3.57}_{2.50}$ | $3.39^{3.77}_{2.76}$ | $3.58^{4.01}_{2.83}$ | $3.65^{4.11}_{3.05}$ | … |
| NGC 4254 | $3.63^{4.26}_{2.96}$ | $3.73^{4.36}_{3.18}$ | $3.34^{3.95}_{2.55}$ | $2.88^{3.11}_{2.29}$ | … | $3.61^{4.28}_{2.94}$ | $3.64^{4.25}_{3.02}$ | … |
| NGC 4303 | $3.53^{4.11}_{2.73}$ | $3.64^{4.15}_{3.03}$ | $3.36^{3.93}_{2.50}$ | $2.29^{3.14}_{1.33}$ | $3.03^{3.42}_{2.65}$ | $3.54^{4.07}_{2.73}$ | $3.57^{4.16}_{2.78}$ | … |
| NGC 4321 | $3.28^{3.82}_{2.69}$ | $3.32^{3.85}_{2.78}$ | $3.11^{3.64}_{2.35}$ | $2.61^{3.31}_{1.84}$ | $3.21^{3.58}_{2.75}$ | $3.26^{3.75}_{2.70}$ | $3.33^{3.92}_{2.69}$ | … |
| NCG 4535 | $2.99^{3.76}_{2.18}$ | $2.95^{3.69}_{2.15}$ | $2.91^{3.55}_{2.13}$ | … | $2.64^{3.15}_{1.89}$ | $3.20^{3.83}_{2.52}$ | $2.96^{3.78}_{2.12}$ | … |
| NGC 5068 | $3.68^{4.74}_{2.28}$ | $4.00^{4.95}_{2.68}$ | $3.21^{4.31}_{1.95}$ | $2.67^{3.39}_{2.00}$ | $3.86^{4.59}_{2.75}$ | … | … | $3.66^{4.76}_{2.24}$ |
| NGC 7496 | $3.29^{4.24}_{1.86}$ | $3.33^{4.29}_{1.95}$ | $3.30^{4.13}_{2.11}$ | … | $3.31^{3.86}_{2.44}$ | … | … | $3.29^{4.28}_{1.84}$ |

**Notes.** List of the average $R_{PAH}$ values for various environments in each galaxy. A "…" is listed when the specified environment does not exist in the galaxy or was not included in the JWST maps. The upper and lower values for each represent the 84th and 16th percentiles for each environment, respectively.

of the F200W measurements and the narrower range of F770W/F200W ratios produced by different stellar emission models, as shown in Figure 5.

One potential issue with using the F200W band to correct for starlight is the possible presence of Paschen-$\alpha$ emission in this filter. To confirm the small influence of the Paschen-$\alpha$ line, we once again use the grid of CIGALE models produced to estimate the contribution of Paschen-$\alpha$ emission to the F200W band. As CIGALE also models the nebular emission, we are able to estimate the fraction of the F200W flux from Paschen-$\alpha$ emission across all of our models. Within the range of models we test, we find the maximum contribution Paschen-$\alpha$ is 2%, with a median contribution of 0.04%, confirming that this emission line will not significantly affect our starlight correction using the F200W filter. It should be noted that the models tested here do not include a wide range of nebular gas emission properties, which is likely limiting the range of contributions from Paschen-$\alpha$ to the F200W filter in these

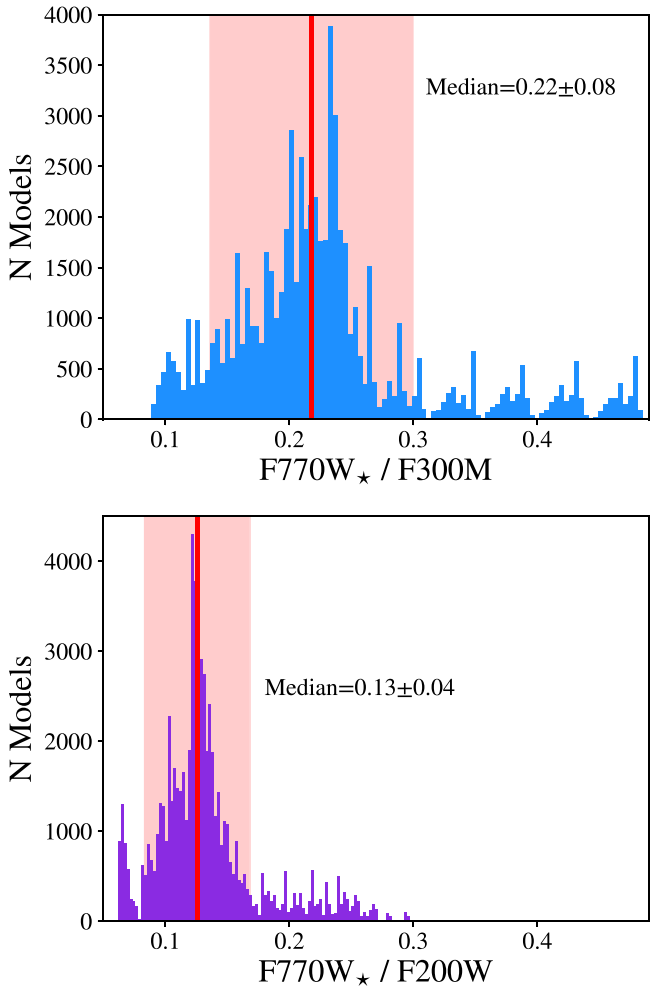


**Figure 5.** Using CIGALE to produce a range of stellar emission models, we determine the expected F770W$_\star$/F300M and F770W$_\star$/F200W ratios assuming only stellar emission in each band. The resulting histograms are displayed, along with the medians as a solid red line, with the standard deviation displayed as a shaded area surrounding the median line.

models. We still advocate for the use of the F200W filter as an indicator of starlight in F770W for the galaxies included in our sample due to the higher signal-to-noise in F200W compared to F300M.

As an additional test, star subtractions in F770W using both F200W and F300M were compared. We find that the average differences between these measurements are $\leqslant$0.01 MJy Sr$^{-1}$, below the signal-to-noise ratio threshold for the F770W data. This suggests that the choice of starlight filter will not impact our overall results. There are some instances where this may no longer be the case, specifically when the ISRF is dominated by an older stellar population. In the top panel of Figure 5, several repeating peaks can be seen in the F770W$_\star$/F300M plot. These peaks represent models with increasingly older stellar populations, which shifts the amount of modeled starlight in the F300M band relative to the F770W band. Because the median does not reflect these older stellar populations, we find that in the nuclei of our galaxies, which will be dominated by an older stellar population, starlight subtractions using F300M remove much less flux than the F200W starlight subtraction. This is a further reason for our choice of the F200W band for the starlight subtraction, which is less dependent on the age of the stellar population.

### 3.2. R$_{PAH}$ as a Proxy for q$_{PAH}$

#### 3.2.1. Comparison to Infrared SED Modeling Results

To determine the effectiveness of using $R_{\rm PAH}$ as a proxy for the fraction of the interstellar dust that is PAHs, we compare our measurements of $R_{\rm PAH}$ to $q_{\rm PAH}$ in a selection of galaxies where MIR-to-FIR SED modeling has been carried out using the Draine & Li (2007) models. $q_{\rm PAH}$ maps were created as part of z0MGs (Leroy et al. 2019), as described in Section 2.2 and Chastenet et al. (2021) and J. Chastenet et al. (2024, in preparation). As the dust modeling uses FIR photometry from Herschel PACS and SPIRE, the maps of $q_{\rm PAH}$ are much lower resolution (18″, the resolution of the SPIRE 250 $\mu$m data) than the MIRI data, and are only available for a subset of the galaxies in our sample: NGC 0628, NGC 1365, NGC 1512, NGC 1566, NGC 3351, NGC 3627, and NGC 4321. These galaxies cover a wide range in morphological type and physical properties, and therefore can be considered representative of the full sample.

In order to compare our measurements of $R_{\rm PAH}$ to the modeled $q_{\rm PAH}$ maps, we first smooth the MIRI data to the SPIRE resolution using a smoothing kernel made by convolving the WebbPSF models with a 16″ Gaussian, using the same method as described in Section 2.1. In NGC 1365, which was masked to remove saturated pixels, the mask was also smoothed to the SPIRE resolution and all pixels with a convolved-mask value greater than 0.9 were discarded to remove all pixels impacted by the large diffraction spikes after convolution. Comparisons between these $R_{\rm PAH}$ and $q_{\rm PAH}$ measurements for each galaxy are shown in Figure 6. Bins are color-coded by the dust model estimates of $\log_{10}(\overline{U})$, the dust mass surface density weighted-average intensity of the radiation field heating the dust (see, e.g., Draine & Li 2007; Aniano et al. 2012; Chastenet et al. 2019, for details). Only bins with at least eight measurements are included in the individual galaxy plots, while only bins with 20 or more measurements are included in the final panel with all seven sources. Each panel also includes solid lines representing the binned medians and dashed lines showing the best-fit linear relationship between $R_{\rm PAH}$ and $q_{\rm PAH}$. The slopes and intercepts for each linear relationship are listed in Table 3. The relative similarity between the slopes and intercepts of the five galaxies shows that the linear relationship between $R_{\rm PAH}$ and $q_{\rm PAH}$ is relatively consistent regardless of galaxy properties. The one exception to this seems to be NGC 1365, where the JWST data had to undergo masking to remove many saturated pixels from the bright nucleus. As we have tried to preserve as much usable data as possible, the chosen cuts may not be adequately removing pixels impacted by the saturation in the nucleus, leading to erroneous high or low values of F2100W, which could be partially responsible for the increased scatter here. Additionally, cutting all the pixels from the nucleus, where $R_{\rm PAH}$ tends to be lower and more uniform, will increase the scatter we see in the binned histograms shown in Figure 6. Further discussion of the correlation between IR photometry ratios and $q_{\rm PAH}$ can be found in Appendix E.

#### 3.2.2. Expectation from Dust Models

We also explore the $R_{\rm PAH}$–$q_{\rm PAH}$ relation expected based on models. We use the models of Draine & Li (2007) and Hensley & Draine (2023) to determine $R_{\rm PAH}$ for models with a range of radiation field intensities $U$, $q_{\rm PAH}$, and size distributions. Here,

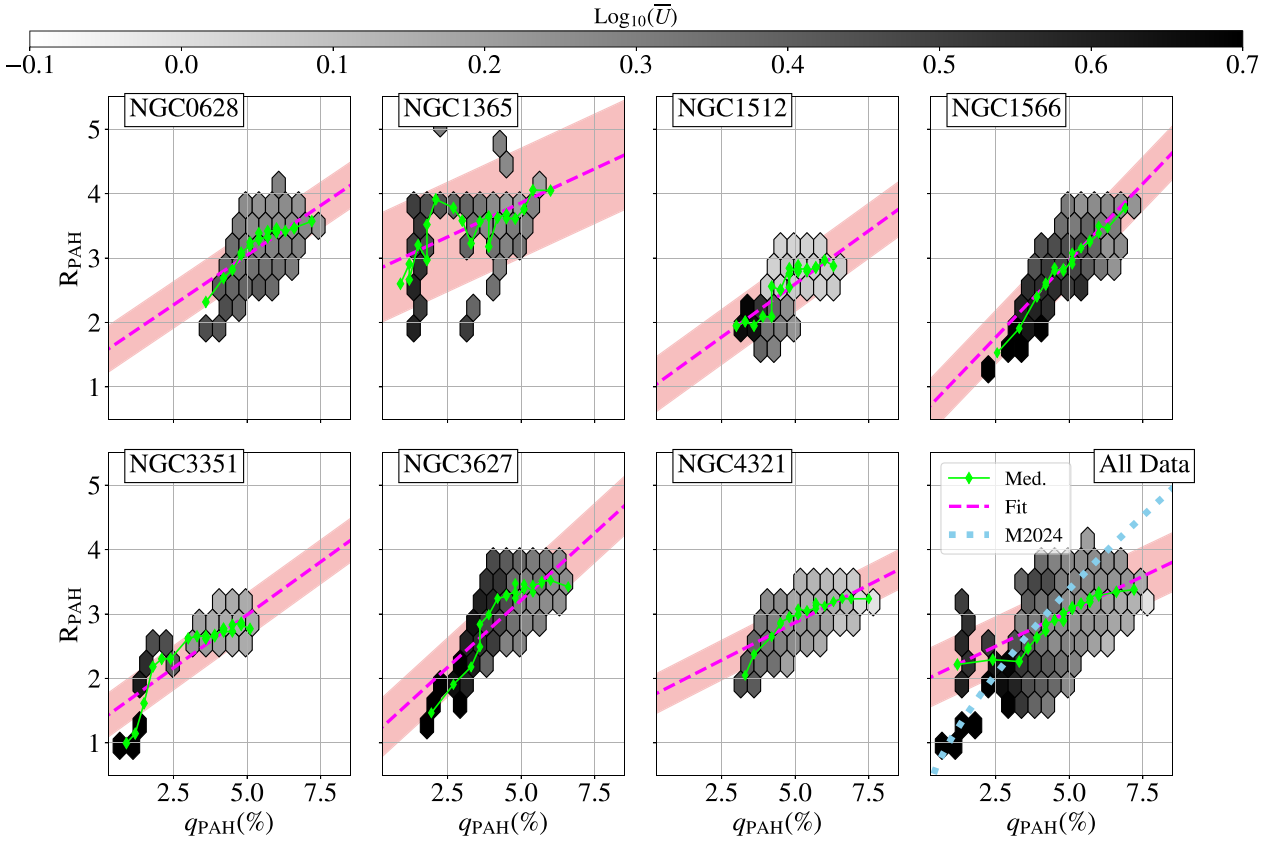


**Figure 6.** Binned data showing $R_{\rm PAH}$ vs. $q_{\rm PAH}$ for the subsample of galaxies with available $q_{\rm PAH}$ maps from the z0MGs survey (Chastenet et al. 2021; J. Chastenet et al. 2024, in preparation). Bins are color-coded by the average radiation field heating the dust, represented by the average $\log_{10}(\overline{U})$ value. Only bins with significant numbers of measurements are plotted. Binned medians are shown as solid lines, while lines of best fit are displayed in each panel as dashed pink lines, with the $1\sigma$ scatter shaded on either side. The final panel shows the binned medians for all galaxies together, and also includes the predicted relationship between $R_{\rm PAH}$ and $q_{\rm PAH}$ from Matsumoto et al. (2024, M2024) for dust grains heated by a 3 Gyr stellar population as a blue dotted line.

**Table 3**
Slopes of $R_{\rm PAH}$ vs. $q_{\rm PAH}$ Relationships

| Target | Slope | Intercept | rms | $R^2$ |
|---|---|---|---|---|
| NGC 0628 | 0.308 | 1.51 | 0.35 | 0.35 |
| NGC 1365 | 0.228 | 2.73 | 0.85 | 0.15 |
| NGC 1512 | 0.332 | 0.96 | 0.42 | 0.40 |
| NGC 1566 | 0.473 | 0.60 | 0.42 | 0.60 |
| NGC 3351 | 0.329 | 1.33 | 0.34 | 0.55 |
| NGC 3627 | 0.421 | 1.11 | 0.45 | 0.62 |
| NGC 4321 | 0.235 | 1.68 | 0.35 | 0.44 |
| All | 0.330 | 1.30 | 0.42 | 0.49 |

**Notes.** Slopes and intercepts found assuming a linear relationship between $R_{\rm PAH}$ and $q_{\rm PAH}$, in the form $R_{\rm PAH} = m \times q_{\rm PAH} + b$. The rms scatter and coefficient of determination ($R^2$, with values closer to 1 showing a better fit) are listed to demonstrate the significance of relationships.

$U$ is the radiation field intensity in units of the Mathis et al. (1983) solar neighborhood radiation field ($U_{\rm MMP}$). We use the Draine & Li (2007) over the Draine et al. (2021) models as these include $q_{\rm PAH}$ as a model parameter, while the Draine et al. (2021) models do not. Synthetic photometry for the F770W, F1130W, and F2100W filters was then performed on a range of the available Draine & Li (2007) and Hensley & Draine (2023) models, to track how $R_{\rm PAH}$ varies with $q_{\rm PAH}$ in these widely used models of PAH emission. As these models *only* include dust emission, we do not replicate our star subtraction for the model fluxes.

The results of this analysis are shown in Figure 7, along with the measurements from the sample with $q_{\rm PAH}$ estimates, displayed as a gray histogram. The estimates produced by the Draine & Li (2007) models are shown on the left, where solid and dashed lines show the model values of $R_{\rm PAH}$ for the range of $q_{\rm PAH}$ available. Different colors represent different values of $U_{\rm min}$, the minimum ISRF heating the dust, and the solid and dashed lines represent two values of $\gamma$, the fraction of dust heated by a radiation field greater than $U_{\rm min}$, 0.01 (solid lines) and 0.005 (dashed lines). The data almost completely fall within the ranges predicted by the models. These models show a directly proportional relationship between $R_{\rm PAH}$ and $q_{\rm PAH}$, with systematic shifts driven by changes in the radiation field heating the dust.

Three models of $R_{\rm PAH}$ as a function of $q_{\rm PAH}$ from Hensley & Draine (2023) are overplotted on our subsample in the right panel. The Hensley & Draine (2023) models were produced using three PAH size distributions, the small, standard, and large size distributions described in Draine et al. (2021), a $\log_{10} U$ of 1.0, and $\gamma = 0$. We note that in this comparison the radiation field is assumed to have a fixed spectral shape, given by the Mathis et al. (1983) solar neighborhood radiation field. Changes in the radiation field hardness can also shift the $R_{\rm PAH}$–$q_{\rm PAH}$ relationship. As shown in Appendix B, changing the PAH ionization fraction does not noticeably shift the measurement of $R_{\rm PAH}$, as long as $U$ and the size distribution are held constant, so changes to the ionization fraction are not included here. This seems to be due to the fact that charged

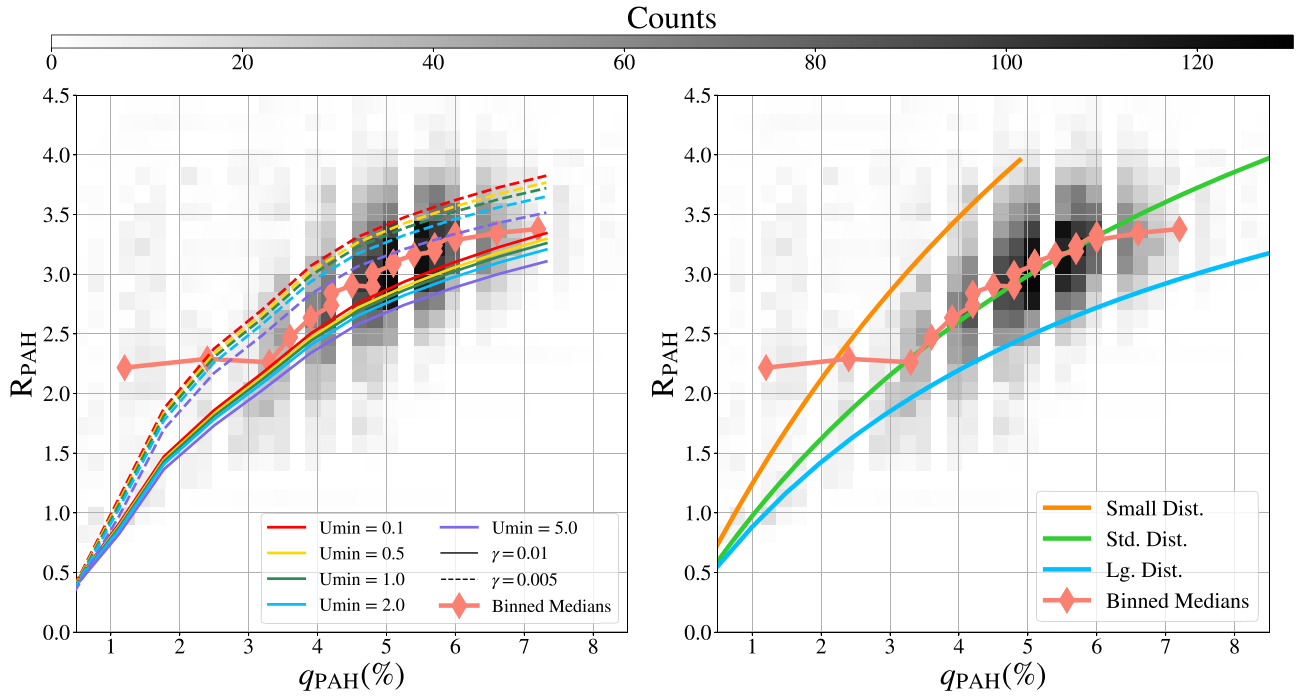


**Figure 7.** $R_{PAH}$ plotted against the modeled $q_{PAH}$ values for the five galaxies with $q_{PAH}$ maps (gray histogram, and pink diamonds representing the binned data). Overplotted are predictions for $R_{PAH}$ as a function of $q_{PAH}$ from the Draine & Li (2007) dust models (left) and Hensley & Draine (2023) models (right). In the Draine & Li (2007) models, we vary $U_{min}$, the minimum value of the ISRF, from 0.1 to 5.0, and use two values of $\gamma$, the fraction of dust heated by a radiation field greater than $U_{min}$, of $\gamma = 0.01$ (solid lines) and $\gamma = 0.005$ (dashed lines). The Hensley & Draine (2023) models were measured using the small, standard, and large size distribution and standard ionization distribution, and varying the relative emission from PAHs and graphite, in a radiation field $U = 1.0$.

PAHs emit more in the F770W band, while neutral PAHs emit more in the F1130W band, so changing the charge distribution only shifts the relative strengths of the two features, but not the total emission in these two bands. In these models, $q_{PAH}$ is varied by changing the $B_1$ and $B_2$ parameters in the PAH distribution (see Hensley & Draine 2023, their Equation (18)). All other Hensley & Draine (2023) model parameters are kept at those recommended in the paper. For all three size distributions, $R_{PAH}$ increases with $q_{PAH}$, although the smallest PAHs produce the largest values of $R_{PAH}$ for a given $q_{PAH}$.

To summarize, the basic theoretical expectation from dust models is that $R_{PAH}$ and $q_{PAH}$ show a clear, characteristic correspondence and that the radiation field intensity perturbs this only moderately over the range $U \sim 0.1$–10.

Additionally, while we see a relatively linear relationship between $R_{PAH}$ and $q_{PAH}$ in both the models and the data at low $q_{PAH}$ (with the exception of data from NGC 1365, which is driving the observed flattening in $R_{PAH}$ at low $q_{PAH}$ as it contains the bulk of our low-$q_{PAH}$ pixels), the slope of this relationship decreases slightly in the models at an $R_{PAH}$ value of $\sim$3.5 above $q_{PAH}$ of 5%. Examinations of the Draine & Li (2007) models suggest this flattening effect is caused by the smaller relative contribution of non-PAH continuum emission to the F2100W band at high $q_{PAH}$. Although there are no PAH emission features in this band, the Draine et al. (2021) models, which split emission up into carbonaceous grains (PAHs and graphite) and AstroDust show continuum emission from small grains, including PAHs, contributing up to $\sim$80% of the F2100W flux at $q_{PAH} \geqslant 4.5\%$. Despite this, as there are no longer-wavelength photometric dust continuum tracers at similar sensitivities and resolution, $R_{PAH}$ is the best possible tracer of PAH abundance at high angular resolution in most conditions expected to be found in typical galaxy ISMs. Although this indicates that $R_{PAH}$ is less sensitive to changes in $q_{PAH}$ at $q_{PAH} \geqslant 4.5\%$, the linear trend below a $q_{PAH}$ of 4.5 shows that $R_{PAH}$ can provide a robust tracer of regions with low $q_{PAH}$, where it is likely PAH destruction will lower $q_{PAH}$.

## 4. Trends in $R_{PAH}$

With these results verifying $R_{PAH}$ traces $q_{PAH}$ in ISM conditions expected of our sample, we can now investigate how $R_{PAH}$ changes as a function of galaxy properties. By comparing $R_{PAH}$ to the relative fractions of ionized, molecular, and atomic gas, as well as the ISM metallicity and galaxy environment, we can establish where within the ISM we expect the PAH fraction to vary. Additionally, by isolating $R_{PAH}$ from the nebular regions identified in Groves et al. (2023), we can determine how the PAH fraction in the vicinity of H II regions ($R_{PAH,Neb}$) differs from that in the diffuse gas ($R_{PAH,Diffuse}$). As our definition of "diffuse" gas is based only on the nebular regions identified using the on average 70 pc resolution H$\alpha$ maps, it will include both diffuse gas and molecular clouds. Throughout this paper, we will use $R_{PAH,Diffuse}$ to represent all $R_{PAH}$ measurements in regions not identified as nebular regions, which will be dominated by diffuse gas but will include other nonionized gas as well.

### 4.1. Decreases in $R_{PAH}$ Measured in H II Regions

#### 4.1.1. Differences in Nebular Region versus Diffuse Gas $R_{PAH}$ Averages

The most notable trend in $R_{PAH}$ is the steep decrease seen within the nebular regions, suggestive of the destruction of PAHs within H II regions. This can be seen in Figure 2, as lower $R_{PAH}$ values (darker purple color) within the nebular region contours. Similar trends in subsets of the PHANGS-

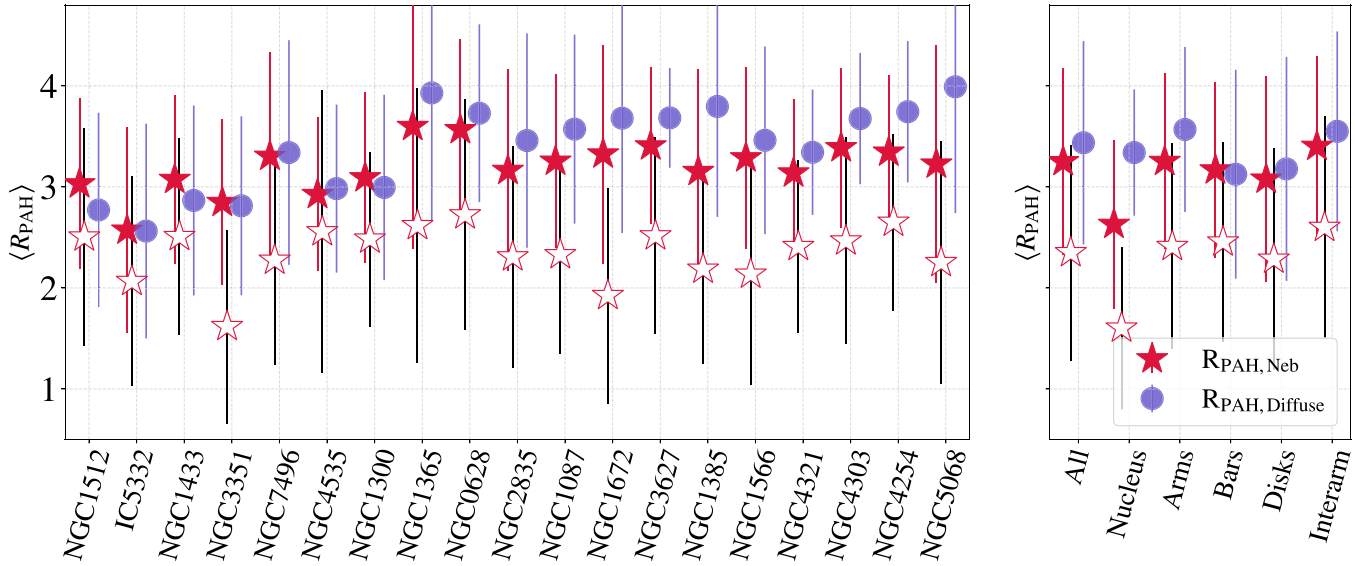


**Figure 8.** Median $R_{\rm PAH}$ values for each galaxy within (red stars, $R_{\rm PAH,Neb}$) and outside (blue circles, $R_{\rm PAH,Diffuse}$) of the nebular regions classified by Groves et al. (2023). Vertical bars on each point represent $1\sigma$ scatter. Empty red stars are the H$\alpha$ weighted averages of $R_{\rm PAH,Neb}$, with black error bars representing the H$\alpha$-weighted scatter. Galaxies are ordered by increasing sSFR.

JWST galaxies were identified by Chastenet et al. (2023a) and Egorov et al. (2023). We quantify this difference using the nebular catalogs of Groves et al. (2023) to isolate nebular regions and compare to diffuse gas. We include all nebular regions identified in Groves et al. (2023) within the coverage of our MIRI observations. It is worth noting that the definition of a nebular region is limited by the resolution of the MUSE maps, and the nebular catalog boundary generally extends well beyond the limit of the actual H II regions (see Barnes et al. 2022, for further discussion). Future work comparing $R_{\rm PAH}$ to the higher-resolution Hubble Space Telescope (HST) H$\alpha$ data could better address the effects of spatial resolution on isolating the nebular regions, but for the purposes of this work we treat the nebular regions as a conservative cut that isolates H II regions from the surrounding neutral ISM. In order to adjust for the fact that the nebular regions extend outside of the boundary of the actual H II regions (i.e., include some contribution from the diffuse ISM), we also investigate the $I$(H$\alpha$) weighted-average $R_{\rm PAH,Neb}$ values. By weighting $R_{\rm PAH,Neb}$ by the H$\alpha$ surface brightness, the pixels clearly inside the H II regions play a larger role setting the average $R_{\rm PAH,Neb}$ value, while those sampling mainly diffuse neutral gas will have less of an impact.

Across the full sample of galaxies, the H$\alpha$ surface-brightness weighted average of $R_{\rm PAH}$ within the nebular regions is 2.31 with a $\pm1\sigma$ scatter of $\pm0.69$, while the average of $R_{\rm PAH}$ outside of the nebular regions (not weighted by H$\alpha$) is 3.43 with a $\pm1\sigma$ scatter of $\pm0.71$, showing a 1.6 times the standard deviation of $R_{\rm PAH,Neb}$ increase in $R_{\rm PAH}$ outside of nebular regions. The difference in average values measured between the diffuse gas and nebular regions implies a lower PAH fraction within H II regions, suggestive of PAH destruction.

The difference in $R_{\rm PAH}$ between nebular and diffuse regions is further illustrated in Figure 8, which displays the median values of $R_{\rm PAH}$ within the nebular regions, $\langle R_{\rm PAH,Neb}\rangle$, and outside of the nebular regions, $\langle R_{\rm PAH,Diffuse}\rangle$, for each galaxy (left panel), as well as in the full sample and individual environments (right panel). Error bars on each point represent the $1\sigma$ standard deviation of the values of all pixels included in those regions. The empty red stars are the H$\alpha$-weighted $\langle R_{\rm PAH,Neb}\rangle$ averages, which are consistently lower than the non-H$\alpha$-weighted median $\langle R_{\rm PAH,Neb}\rangle$ values. This emphasizes that the highest-surface-brightness H II regions, which will often have the highest $U$ values, have the lowest values of $R_{\rm PAH}$. We note that changing the radiation field intensity can also contribute to changing the mapping between $R_{\rm PAH}$ and $q_{\rm PAH}$, though we argue (see Appendix E) that this is a minor effect for the range of radiation field intensities we expect. The low $R_{\rm PAH}$ values in the regions with high H$\alpha$ surface brightness and radiation field intensities was also explored by Egorov et al. (2023), who found anticorrelations between $R_{\rm PAH}$ measured in H II regions and both the ionization parameter and H II-region surface brightness of those regions.

By examining the right panel of Figure 8, we find that across the various galactic environments (arms, bars, nuclei, disks, and interarm regions), the difference between $\langle R_{\rm PAH,Neb}\rangle$ and $\langle R_{\rm PAH,Diffuse}\rangle$ is largest for the nuclei and spiral arms, which together host the bulk of the star formation. In the more quiescent disks, bars, and interarm regions, the differences between $R_{\rm PAH}$ in the nebular and diffuse gas shrinks. In these more quiescent environments, it is also expected that the nebular regions would be smaller and therefore more difficult to resolve in the MUSE data. This could lead to some misidentified pixels, which would drive the diffuse and nebular $R_{\rm PAH}$ measurements closer together. Further discussion of this point is presented in Section 4.1.3

In the left panel of Figure 8, the galaxies are sorted by the sSFR, where sSFR was computed only including data within the area covered by the JWST footprints, determined using the maps from Belfiore et al. (2023; see Section 2.4 for details). Using this order, we see that while both the weighted and unweighted values of $\langle R_{\rm PAH,Neb}\rangle$ are relatively constant across the sample, the $\langle R_{\rm PAH,Diffuse}\rangle$ increases with sSFR. This is further demonstrated in Figure 9, whose top row shows $\langle R_{\rm PAH,Neb}\rangle$ and $\langle R_{\rm PAH,Diffuse}\rangle$ plotted as a function of SFR, $M_\star$, and sSFR. The bottom row plots the difference between the average $R_{\rm PAH}$ in the diffuse and nebular regions, as a function of these same variables. The Spearman's rank correlation coefficient ($\rho$) and $p$-value ($p$) are listed in each panel of

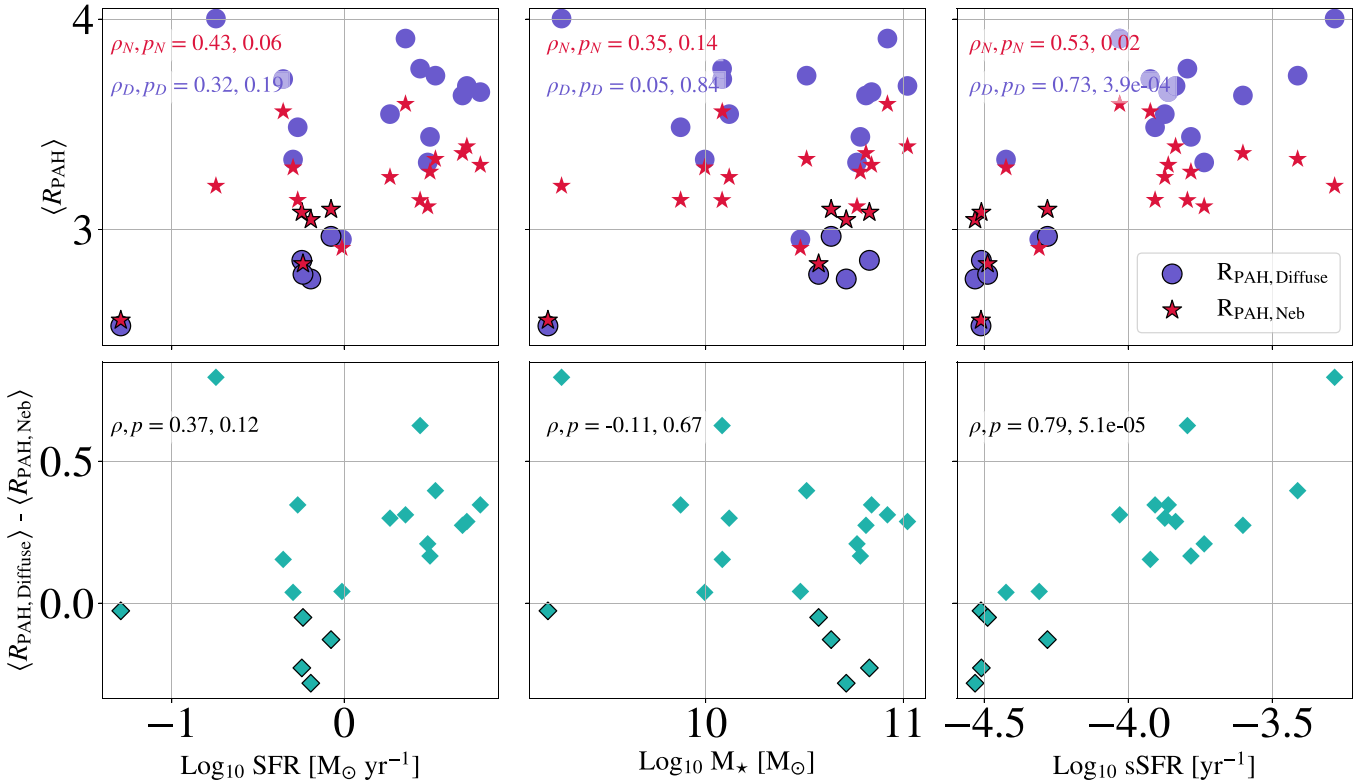


**Figure 9.** Top row: average $R_{\rm PAH}$ values plotted as a function of SFR (left), stellar mass (middle), and sSFR (right). Red stars are the average $R_{\rm PAH}$ within the nebular regions and blue circles are the average $R_{\rm PAH}$ in the diffuse gas, for each galaxy. SFR, $M_\star$, and sSFR were all computed using the same method as in Figure 8. Points outlined in black represent galaxies where $\langle R_{\rm PAH,Neb}\rangle$ is greater than $\langle R_{\rm PAH,Diffuse}\rangle$. Bottom row: the differences between the average $R_{\rm PAH}$ in the nebular and diffuse gas, plotted as a function of SFR, $M_\star$, and sSFR. Diamonds outlined in black represent galaxies where $\langle R_{\rm PAH,Neb}\rangle$ is greater than $\langle R_{\rm PAH,Diffuse}\rangle$.

Figure 9, showing that the most significant trends we observe are between $\langle R_{\rm PAH,Diffuse}\rangle$ and $\log_{10}$sSFR, with $\rho_D = 0.73$, and $\langle R_{\rm PAH,Diffuse}\rangle - \langle R_{\rm PAH,Neb}\rangle$ and $\log_{10}$sSFR, with $\rho = 0.79$. All of the other panels have correlations that would not be considered significant based on their $p$-values.

While the majority of the galaxies in this sample have $\langle R_{\rm PAH,Diffuse}\rangle > \langle R_{\rm PAH,Neb}\rangle$, a subset with low sSFR show the opposite trend: NGC 1512, NGC 1433, NGC 3351, and IC 5332. In addition, NGC 7496 and NGC 1300 have nearly equivalent $R_{\rm PAH,Diffuse}$ and $R_{\rm PAH,Neb}$. Of these galaxies, four share a similar structure, with a strong bar that extends to a bright outer ring (NGC 1512, NGC 1433, NGC 1300, and NGC 3351). Within these JWST images, the stellar bar takes up a large fraction of the field of view, and lacks any significant star formation. By examining the H$\alpha$ data, we find that the bars in these galaxies appear "dark," with little ongoing star formation. This phenomenon is widely observed in barred galaxies, and is described as "star formation deserts" (James & Percival 2018; Neumann et al. 2020). Because there are few nebular regions within these bars or the areas surrounding them, they make a substantial contribution to the $\langle R_{\rm PAH,Diffuse}\rangle$ for these sources. Across the maps of these four galaxies, we find that these environments have very low fluxes in all MIRI bands, likely indicative that the dominant ISRF heating the dust is from an older stellar population or a low gas surface density. These low-SFR bars could therefore be driving down our measurements of $\langle R_{\rm PAH,Diffuse}\rangle$ through softer radiation fields that have fewer UV photons to excite the PAHs across these star formation deserts, even if $q_{\rm PAH}$ has not changed.

The other two galaxies that show lower $\langle R_{\rm PAH,Diffuse}\rangle$ compared to $\langle R_{\rm PAH,Neb}\rangle$ are IC 5332, the lowest-metallicity galaxy of our sample, and NGC 7496, which contains both a bar and an AGN. While the difference in IC 5332 *could* be due to its lower metallicity, NGC 5068, which has a similar metallicity, has one of the largest positive differences between $\langle R_{\rm PAH,Diffuse}\rangle$ and $\langle R_{\rm PAH,Neb}\rangle$, making it unlikely metallicity alone is driving this shift. Alternatively, IC 5332 and NGC 7496 both have low sSFR, while NGC 5068 has the highest sSFR of our sample, suggesting that these differences are more driven by changes in sSFR than other ISM conditions. This effect will be further investigated in Section 4.1.3.

### 4.1.2. Pixel-based Measurements

In addition to examining the galaxy-averaged nebular versus diffuse $R_{\rm PAH}$ trends presented above, we can trace changes in $R_{\rm PAH}$ using our pixel-based measurements and compare to a tracer of the relative amount of ionized gas in each pixel, $I_{\rm H\alpha}/\Sigma_{\rm HI+H_2}$, following work by Chastenet et al. (2019, 2023a). This ratio uses the intensity of the H$\alpha$ line as a proxy for the amount of ionized gas, and normalizes by the total surface density of neutral (H I) and molecular ($H_2$) gas. Figure 10 shows the behavior of $R_{\rm PAH}$, both in nebular and diffuse regions, as a function of $\log_{10}(I_{\rm H\alpha}/\Sigma_{\rm HI+H_2})$. Each colored line represents the binned medians for an individual galaxy, color-coded by increasing $\log_{10}$sSFR value inside the JWST footprint. Individual galaxy pixel-based histograms are available in Appendix A. Each galaxy shows a decreasing trend above $\log_{10}(I_{\rm H\alpha}/\Sigma_{\rm HI+H_2}) \sim 37.5$ erg s$^{-1}$ kpc$^{-2}$ $(M_\odot\,{\rm pc}^{-2})^{-1}$. This is similar to what was seen for the smaller sample presented in Chastenet et al. (2023a). Regions with $\log_{10}(I_{\rm H\alpha}/\Sigma_{\rm HI+H_2}) \gtrsim 37.5$ erg s$^{-1}$ kpc$^{-2}$ $(M_\odot\,{\rm pc}^{-2})^{-1}$ are

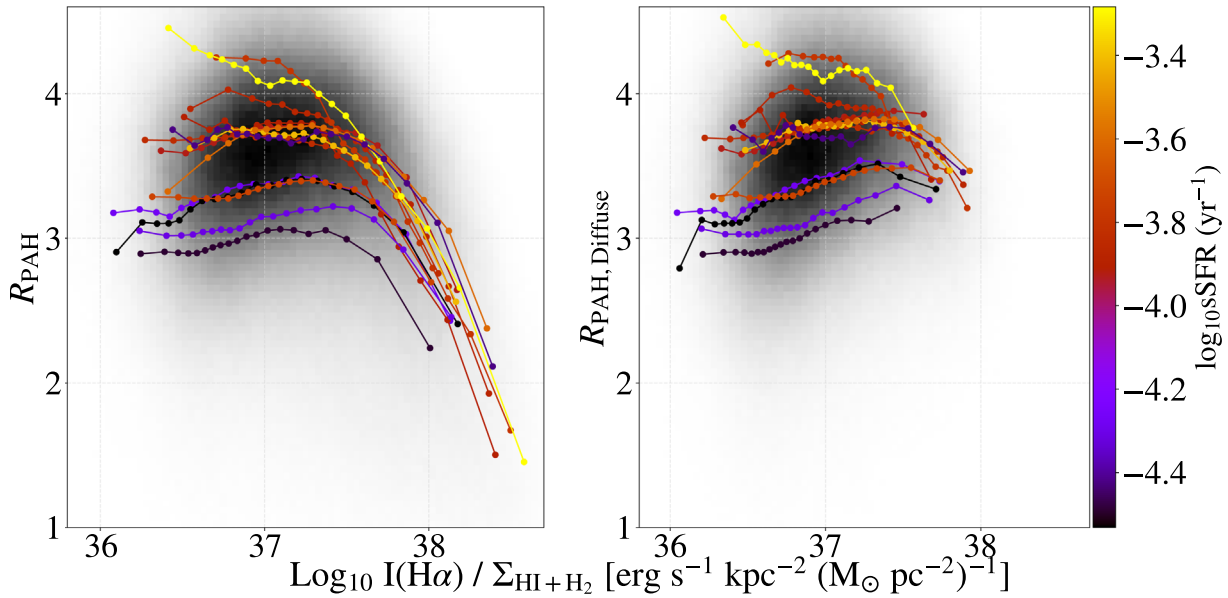


**Figure 10.** $R_{PAH}$ vs. $I_{H\alpha}/\Sigma_{HI+H_2}$ for the full sample with H I data. Left panel shows all data, right panel shows only $R_{PAH,Diffuse}$. Lines represent binned medians for each galaxy, color-coded by sSFR.

primarily regions identified as nebular regions. In the right panel of Figure 10, we can see that $R_{PAH,Diffuse}$ does not have a strong dependence on $I_{H\alpha}/\Sigma_{HI+H_2}$. Here, we see very few pixels above $\log_{10}(I_{H\alpha}/\Sigma_{HI+H_2}) = 37.5$ erg s$^{-1}$ kpc$^{-2}$ ($M_\odot$ pc$^{-2}$)$^{-1}$, and no decreasing trend, validating the expectation that the decreasing trend is being driven by $R_{PAH}$ changes within the nebular regions. Figure 10 also shows that the binned median $R_{PAH,Diffuse}$ at a given $I_{H\alpha}/\Sigma_{HI+H_2}$ increases with average sSFR, following the trend seen for the galaxy-averaged $R_{PAH,Diffuse}$.

#### 4.1.3. 1 kpc Scales

In Figure 8, the average $R_{PAH}$ for each individual galaxy is plotted, and trends in these quantities are shown in Figure 9. The most significant trend we find is the correlation between $\langle R_{PAH,Diffuse}\rangle - \langle R_{PAH,Neb}\rangle$ and $\log_{10}$sSFR, as shown by the Spearman's rank correlation coefficient: $\rho = 0.79$, $p = 5.1 \times 10^{-5}$. To further examine this trend and determine whether sSFR remains the dominant driver of changes to the average $R_{PAH}$ on smaller scales, we examined the $\langle R_{PAH,Diffuse}\rangle$ and $\langle R_{PAH,Neb}\rangle$ in 1 kpc regions. These 1 kpc regions allow us to break down the galaxies by environment and test whether the correlations between the average $R_{PAH}$ and $I(H\alpha)$ or $\log_{10}$SFR become tighter than $\log_{10}$sSFR when smaller scales are considered. 1 kpc regions are chosen because this size is large enough to contain both significant numbers of pixels identified as nebular and diffuse, while also allowing us to obtain a meaningful measurement of sSFR, which would not be possible in isolated diffuse gas pixels.

Examining the trends in sSFR, $I(H\alpha)$, and SFR with both $\langle R_{PAH,Diffuse}\rangle$ and $\langle R_{PAH,Neb}\rangle$ measured in 1 kpc regions, we find that sSFR remains the best predictor of changes in $\langle R_{PAH,Diffuse}\rangle$. The relationship between $\langle R_{PAH,Diffuse}\rangle$ and $\log_{10}$sSFR is shown in the right panel of Figure 11, with $\langle R_{PAH,Neb}\rangle$ in the left panel. In this figure, we can see across the range of $\log_{10}$sSFR that $\langle R_{PAH,Neb}\rangle$ decreases slightly, while $\langle R_{PAH,Diffuse}\rangle$ increases and then remains constant. The fact that the increasing trend in $\langle R_{PAH,Diffuse}\rangle$ and $\log_{10}$sSFR is still found at 1 kpc scales implies that higher sSFR increases $R_{PAH,Diffuse}$. This is likely due to the fact that at low sSFR the radiation field will be more dominated by softer radiation from an older stellar population that less effectively excites the PAHs (Draine et al. 2021), lowering our observations of $R_{PAH,Diffuse}$ in regions with low sSFR.

Another possible factor to consider while investigating the trends observed in $\langle R_{PAH,Diffuse}\rangle - \langle R_{PAH,Neb}\rangle$ is the limited resolution of the MUSE maps. Due to this limited resolution, the nebular regions defined in Groves et al. (2023) contain some diffuse gas. This is caused by the inability to perfectly resolve the smallest H II regions with MUSE. This effect was confirmed in Barnes et al. (2022), which found H II regions measured by HST H$\alpha$ were smaller than those measured by MUSE, with typical radii $\lesssim$10 pc. If we assume the main factor changing $R_{PAH,Neb}$ across our sample is destruction of PAHs within H II regions, we might expect that $R_{PAH,Neb}$ and $R_{PAH,Diffuse}$ will have two distinct and relatively constant values representing these two phases of the ISM. If smaller nebular regions and the edges of larger nebular regions are contaminated by diffuse gas, we would expect $\langle R_{PAH,Neb}\rangle$ to shift upwards toward $\langle R_{PAH,Diffuse}\rangle$ in nebular regions where this diffuse gas contamination is more significant. We can test this with our 1 kpc measurements by determining what percentage of the pixels in each region are identified as within a nebular region: 1 kpc regions that cover the centers of large, well-defined H II regions will have the majority of their pixels identified as part of the nebular region catalog, while 1 kpc regions containing smaller, unresolved nebular regions or situated at the edges of a larger nebular regions will have low percentages of pixels identified as part of the nebular catalog. If these regions with lower percentages of pixels in nebular regions have more contamination from diffuse gas, we would expect $\langle R_{PAH,Neb}\rangle$ to increase toward the $\langle R_{PAH,Diffuse}\rangle$ value of 3.43. We test this prediction in Figure 12, where the left panel shows the $\langle R_{PAH,Neb}\rangle$ measured in the 1 kpc regions as a function of the percentage of pixels identified as within a nebular region and the right panel shows the trends in $\langle R_{PAH,Diffuse}\rangle$. The black line in the left panel represents the

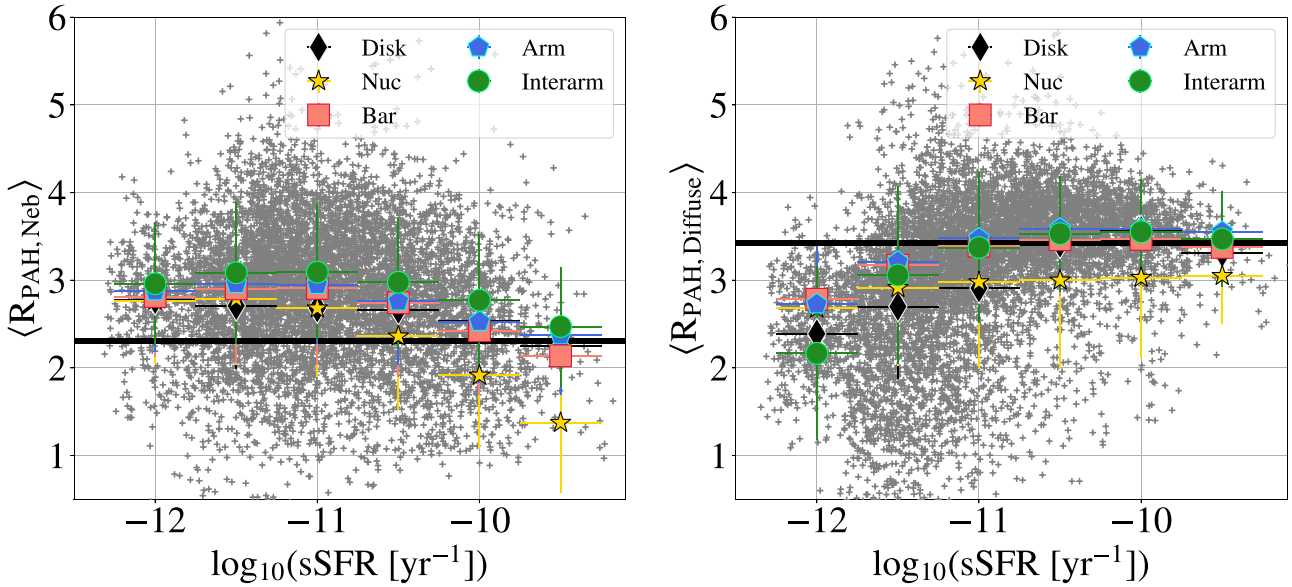


**Figure 11.** Left: $\langle R_{PAH,Neb} \rangle$, measured in 1 kpc regions, plotted as a function of $\log_{10}$sSFR. Binned medians are shown over the full distribution, and are color-coded by environment of origin, with black diamonds being disks, red squares being bars, yellow stars being nuclei, green circles being interarm, and blue pentagons being arms. The black line represents the H$\alpha$-weighted median value of $\langle R_{PAH,Neb} \rangle$ found across the full sample. Right: same, but for $\langle R_{PAH,Diffuse} \rangle$, with the black line representing the median value of $\langle R_{PAH,Diffuse} \rangle$ found across the full sample without H$\alpha$ weighting.

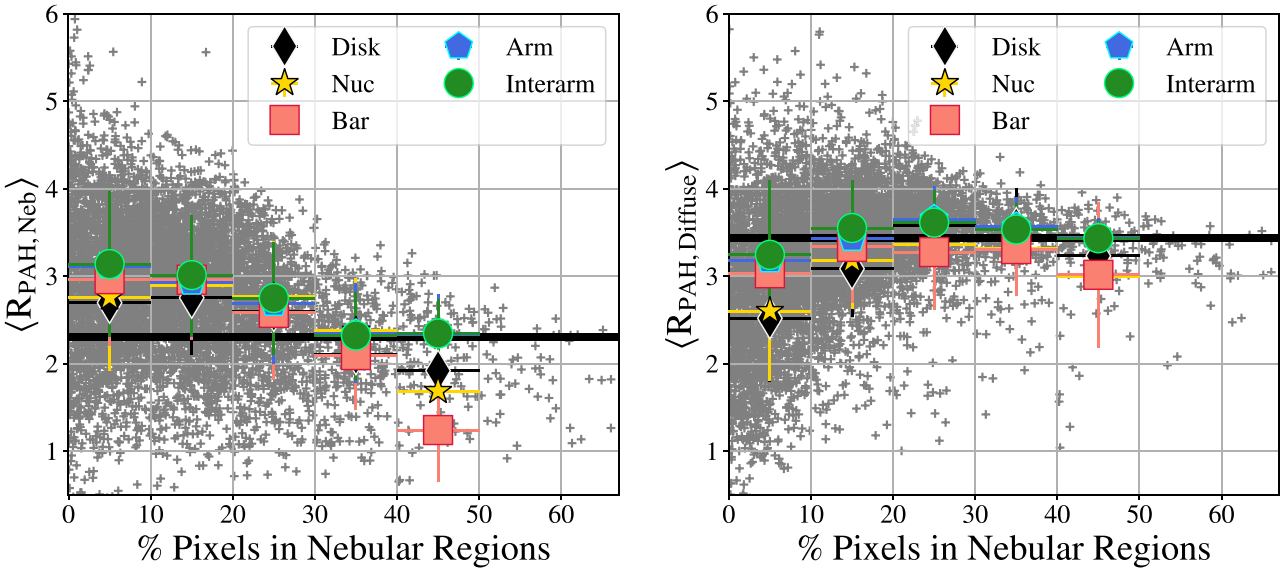


**Figure 12.** Left: $R_{PAH,Neb}$, measured in 1 kpc regions, plotted as a function of the fraction of the pixels in the region in a nebular region. Symbols are the same as in Figure 11. Right: same, but for $R_{PAH,Diffuse}$.

H$\alpha$-weighted value of $\langle R_{PAH,Neb} \rangle$ found above, while the black line in the right pane represents the non-H$\alpha$-weighted $\langle R_{PAH,Diffuse} \rangle$. In the 1 kpc regions with near 30% of their pixels in nebular regions, we see both $\langle R_{PAH,Diffuse} \rangle$ and $\langle R_{PAH,Neb} \rangle$ flatten toward these black lines. This implies that around the larger nebular regions, where the MUSE data can better distinguish between nebular and diffuse gas, $R_{PAH}$ becomes remarkably constant in both the nebular regions (at a value of 2.31 with $\pm 1\sigma$ scatter of 0.78) and in the diffuse gas (at a value of 3.43 with $\pm 1\sigma$ scatter of 0.98).

### 4.2. Further Investigations of $R_{PAH}$ outside of H II Regions

As shown above, the most obvious factor driving changes in $R_{PAH}$ is likely the destruction of PAHs within H II regions. Outside of H II regions, $R_{PAH}$ is relatively constant at a value of $\sim$3.43, indicating either a constant $q_{PAH}$ in the diffuse gas or possibly that we are in a high-$q_{PAH}$ regime, where the mapping between $R_{PAH}$ and $q_{PAH}$ begins to flatten (see Section 3.2 for details). Comparing to the Hensley & Draine (2023) models, we can determine what possible values of $q_{PAH}$ correspond to the average value of $R_{PAH}$ we measure in the diffuse gas. A range of possible $q_{PAH}$ values for different single-$U$ radiation field strengths and PAH size distributions are listed in Table 4. We find that our average $R_{PAH,Diffuse}$ of 3.43 corresponds to a $q_{PAH}$ of 5.5% using the Hensley & Draine (2023) dust models assuming the Draine et al. (2021) standard grain distribution, 8.1% assuming the large grain distribution, or 3.91% using the small grain distribution, in a radiation field with $\log_{10}U = 0.0$

**Table 4**
Predicted $q_{PAH}$ from Hensley & Draine (2023) for $R_{PAH} = 3.43$

| Model | $\log_{10}U = -1$ | $\log_{10}U = 0$ | $\log_{10}U = 1$ |
|---|---|---|---|
| Sm | 3.20% | 3.91% | 4.88% |
| Std | 4.55 % | 5.55% | 9.14% |
| Lg | 6.70% | 8.12% | 13.1% |

**Notes.** Predictions of $q_{PAH}$ from the Hensley & Draine (2023) dust models with single radiation field intensities, to match $R_{PAH,Diffuse} = 3.43$ based on the averages from the 1 kpc regions measured in the full sample. "Sm," "Std," and "Lg" correspond to the small, standard, and large PAH size distributions from Draine et al. (2021).

and $\gamma = 0$. We note that fixing $\gamma = 0$ (i.e., using single values of $U$ rather than a distribution) will produce the widest range of inferred $q_{PAH}$ values for a given $R_{PAH}$, since there is no contribution to the MIR emission from radiation fields that extends up to high intensities. As can be seen in Draine & Li (2007, their Figure 18), contributions from the power-law component can be important at 21 $\mu$m. Therefore, Table 4 represents the widest range of $q_{PAH}$ measurements that could yield $R_{PAH} = 3.43$. In the remainder of this section, we will examine any secondary trends in $R_{PAH,Diffuse}$ that we can measure with the full suite of ancillary data sets available.

#### 4.2.1. $R_{PAH,Diffuse}$ and Galaxy Environment

Using the environment maps from Querejeta et al. (2021), which allow us to sort pixels by the structure they fall in, we examine how $R_{PAH,Diffuse}$ varies as a function of galactic environment. Histograms showing the pixel-based distribution of $R_{PAH,Diffuse}$ in galaxy nuclei, bars, spiral arms, interarm regions, and disks without significant arms are shown in Figure 13. Examining these histograms, we find that $R_{PAH,Diffuse}$ tends to be highest in the spiral arms, and lowest in bars and disks without spiral arms. Galaxy nuclei have the narrowest distributions of $R_{PAH,Diffuse}$, while bars and extended disks have the broadest. Overall, though, all five environments show similar distributions of $R_{PAH,Diffuse}$, suggesting that galactic environment does not drive changes to $R_{PAH,Diffuse}$. Histograms of the distribution of $R_{PAH,Diffuse}$ in isolated environments for each galaxy in our sample can be found in Appendix A.

#### 4.2.2. $\langle R_{PAH,Diffuse} \rangle$ and Integrated Gas Properties

Similar to the analysis in Section 4.1.1, here we examine how $\langle R_{PAH,Diffuse} \rangle$ for each galaxy varies as a function of global galaxy gas properties. Figure 14 shows $\langle R_{PAH,Diffuse} \rangle$ measurements over the full JWST maps as a function of global $M_{H_2}$, $M_{HI}$, $f_{Mol}$, and $12 + \log_{10}$O/H from Lee et al. (2023), as well as the average $\overline{\Sigma_{H_2}}$ and $\overline{\Sigma_{HI}}$ within the area covered by the JWST data. Spearman's $\rho$ and $p$-values are listed in each panel. While we find no significant trends in average $R_{PAH,Diffuse}$ as a function of global galaxy properties, we do see some indication of increases in $R_{PAH,Diffuse}$ with higher $M_{H_2}$ and $\overline{\Sigma_{HI}}$. It is worth noting that while $M_{H_2}$ is well correlated with the SFR, as one would expect based on the Kennicutt–Schmidt relationship, we find none of these quantities is correlated with sSFR, suggesting any correlations found between $\langle R_{PAH,Diffuse} \rangle$ and $M_{H_2}$ or $\overline{\Sigma_{HI}}$ is not driven by the correlation between $\langle R_{PAH,Diffuse} \rangle$ and sSFR, but a separate ISM process.

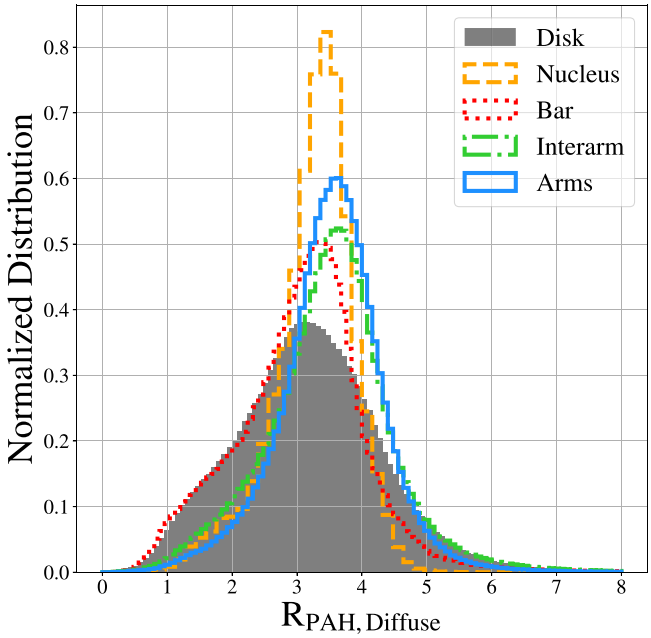


**Figure 13.** Histograms showing the distribution of $R_{PAH}$ for different galactic environments, as defined by Querejeta et al. (2021). Nebular regions have been excluded to remove the effects of PAH destruction in H II regions. Histograms showing individual galaxies can be found in Appendix A.

#### 4.2.3. $R_{PAH,Diffuse}$ as a Function of Metallicity and $H_2$ Gas Fraction on Pixel Scales

Studies of PAH emission from the SMC and LMC (Chastenet et al. 2019; Paradis et al. 2023) as well as in nearby galaxies (see, e.g., Engelbracht et al. 2005; Calzetti et al. 2007; Draine et al. 2007; Gordon et al. 2008; Li 2020) have shown that PAH abundance tends to decrease in low-metallicity environments. We test this trend in our sample by plotting $R_{PAH,Diffuse}$ as a function of $12 + \log_{10}$(O/H), using the maps of Williams et al. (2022). The pixel-by-pixel results of this analysis are shown in the left panel of Figure 15.

The galaxies in our sample are all near solar metallicity and span a fairly small range ($\sim$0.3 dex) in $12 + \log_{10}$(O/H) and show no obvious trends in $R_{PAH,Diffuse}$ as a function of metallicity. A small subsample (IC 5332, NGC 1385, NGC 2835, NGC 5068, and NGC 7496) reach $12 + \log_{10}$(O/H) $< 8.5$. In this subsample, we observe a trend with decreasing $R_{PAH}$ with decreasing $12 + \log_{10}$(O/H). However, due to the small amount of data below this metallicity, it is difficult to diagnose exactly at what value of $12 + \log_{10}$(O/H) this decreasing trend begins, especially when we consider that the galaxy that reaches the lowest $12 + \log_{10}$(O/H) (NGC 5068) also has the highest sSFR, and the highest average value of $R_{PAH,Diffuse}$.

It may also be the case that the PAH fraction could decrease in regions of dense molecular gas, where PAHs may coagulate into larger dust grains (e.g., Miville-Deschênes et al. 2002; Köhler et al. 2015). Dense molecular environments may also have higher values of $A_V$, which could attenuate the UV field. This could lower $R_{PAH}$ at a given PAH fraction as a consequence of the softer radiation field (Draine et al. 2021). Attenuation effects have been suggested to explain high-spatial-resolution observations of MIR-to-FIR colors in MW molecular clouds (Flagey et al. 2009); however, at the 10–50 pc

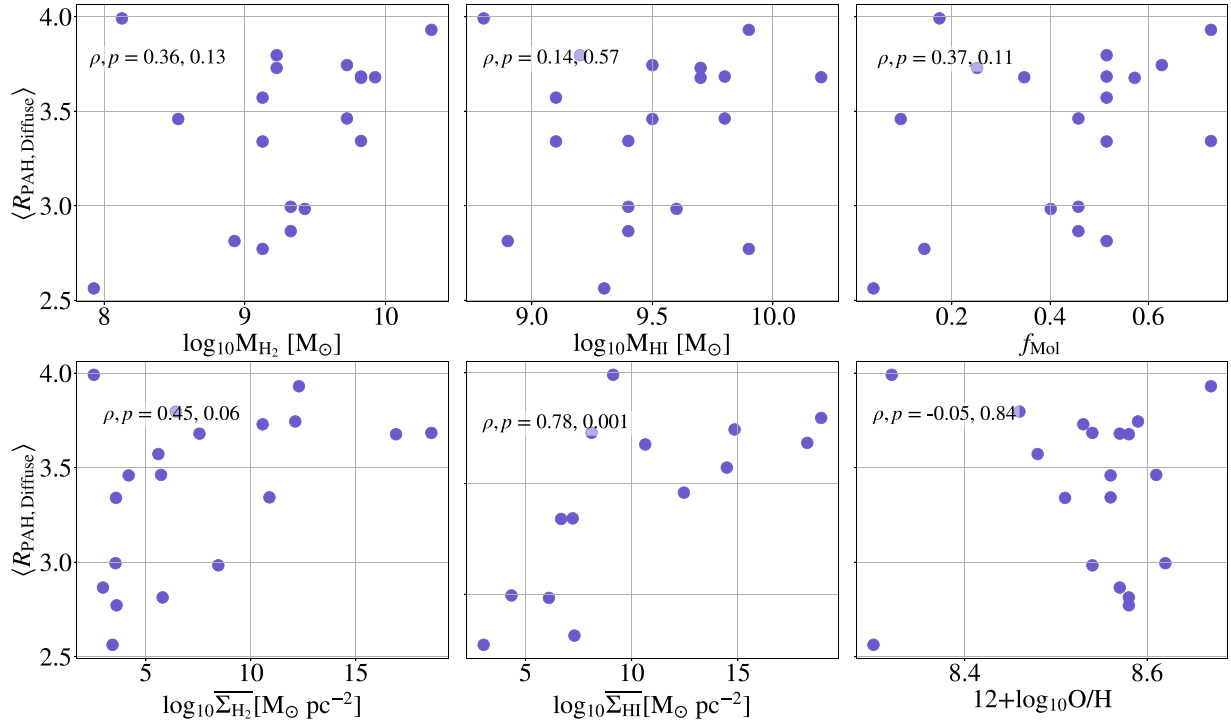


**Figure 14.** Top row: $\langle R_{\rm PAH,Diffuse}\rangle$ as a function of global gas mass, both molecular and atomic, and global molecular gas fraction ($f_{\rm mol}$) from Lee et al. (2023). Bottom row: $\langle R_{\rm PAH,Diffuse}\rangle$ as a function of average atomic ($\overline{\Sigma_{\rm HI}}$) and molecular gas ($\overline{\Sigma_{\rm H_2}}$) surface density determined in the area covered by the JWST data and $12 + \log_{10}{\rm O/H}$ estimated at $R_{\rm eff}$ from Groves et al. (2023).

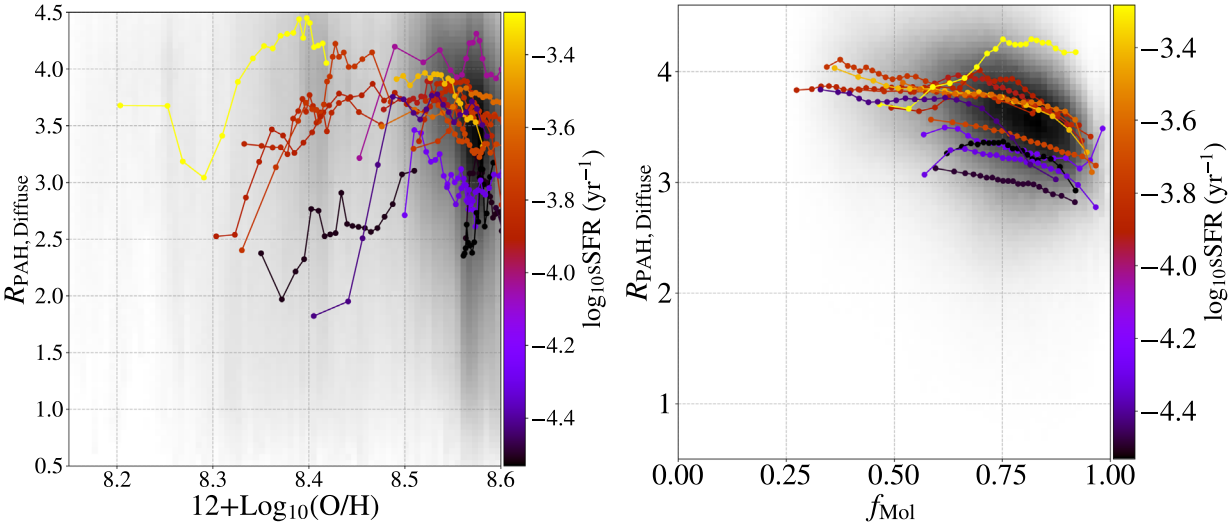


**Figure 15.** The per-pixel values of $R_{\rm PAH,Diffuse}$ plotted as a function of metallicity (right) and $f_{\rm Mol}$ (left). Metallicities were determined using the metallicity maps of Williams et al. (2022). Binned medians are shown for each galaxy, color-coded by sSFR. Histograms for individual galaxies are displayed in Appendix A.

scales we probe, the fraction of dust contributing from highly shielded regions is likely to be small. To test the possible changes in $R_{\rm PAH}$ as a function of molecular gas abundance, the right panel of Figure 15 shows $R_{\rm PAH,Diffuse}$ plotted as a function of $f_{\rm Mol}$, the molecular gas fraction, defined as $f_{\rm Mol} = \Sigma_{\rm H_2}/(\Sigma_{\rm H_2} + \Sigma_{\rm HI})$. We find a fairly flat relationship between $R_{\rm PAH,Diffuse}$ and $f_{\rm Mol}$ below $f_{\rm Mol} = 0.8$, followed by a decreasing trend in $R_{\rm PAH,Diffuse}$.

## 5. Discussion

Prior to the launch of JWST, $R_{\rm PAH}$-equivalent measurements (i.e., requiring only MIR observations) at <50 pc resolution were restricted to the galaxies of the Local Group ($D \lesssim 1$ Mpc) because of the resolution of Spitzer and WISE ($\sim 6''$ and $\sim 12''$, respectively, at $\sim 20$ $\mu$m). For the Magellanic Clouds, existing FIR measurements also reach 10 pc spatial resolution, enabling highly spatially resolved studies of $q_{\rm PAH}$ across the LMC and SMC (Sandstrom et al. 2010; Paradis et al. 2011; Chastenet et al. 2019). The high-resolution measurements of $R_{\rm PAH}$ from PHANGS-JWST give new insights into the behavior of the PAH fraction at ~solar metallicity. In this section, we will highlight the primary results of this paper and how these results fit into the broader picture of PAH studies.

### 5.1. $R_{PAH}$ as a Tracer of $q_{PAH}$

The fraction of dust in the form of PAHs with $<10^3$ C atoms ($q_{\rm PAH}$; Draine & Li 2007) can be constrained using MIR through FIR observations. From the FIR, the peak of the thermal dust SED provides information on the radiation field intensity. The shape of the FIR SED can also provide constraints on the distribution of radiation fields heating the dust (Dale et al. 2014). With this information on the radiation field, the addition of MIR measurements that sample PAH emission yield a constraint on $q_{\rm PAH}$, since the primarily stochastic emission from PAHs is proportional to the radiation field intensity. The inferred PAH surface density compared with the dust mass surface density constrained by the FIR peak yields $q_{\rm PAH}$.

The resolution of existing FIR data sets strongly limits the sample of galaxies where $q_{\rm PAH}$ can be resolved at 10−50 pc resolution to the Local Group. For this reason, it is critical to explore MIR-only indicators of PAH fraction to extend observations beyond the nearest galaxies in order to make progress in understanding the life cycle of PAHs. In this paper, we have explored the MIR-only diagnostic $R_{\rm PAH} = ({\rm F770W_{ss}}+{\rm F1130W})/{\rm F2100W}$ as an indicator of $q_{\rm PAH}$. We have compared $R_{\rm PAH}$ and $q_{\rm PAH}$ at low resolution for several galaxies with FIR observations that were also covered by PHANGS-JWST, and found good correlation. We also explored the relationship between the predicted $R_{\rm PAH}$ to $q_{\rm PAH}$ in the Draine & Li (2007) dust models and their recent updates (Draine et al. 2021; Hensley & Draine 2023). In general, at dust mass weighted-average radiation field intensities $\lesssim 10^2$, which is typical for regions in our galaxies at 10–50 pc resolution, $R_{\rm PAH}$ is well correlated with $q_{\rm PAH}$, yielding a good diagnostic for changes in the PAH fraction (see also Appendix E). It is worth noting that the mapping between $R_{\rm PAH}$ and $q_{\rm PAH}$ is nonlinear and at high values of $q_{\rm PAH} > 5\%$ (super-MW $q_{\rm PAH}$ values), the slope between them becomes flatter, resulting in only small changes in $R_{\rm PAH}$ as $q_{\rm PAH}$ increases. On the other hand, decreases in $R_{\rm PAH}$ are a good diagnostic for revealing locations where the PAH fraction drops, presuming the dust mass weighted-average radiation field is not $U \gg 10^2$.

There are several questions about the $R_{\rm PAH}$–$q_{\rm PAH}$ relationship that should be addressed in future studies. First, we have focused on the Draine & Li (2007) model, which makes specific assumptions about the dust grain size distribution. Other dust models make different assumptions about grain size distributions and dust optical properties that can change the interpretation of $R_{\rm PAH}$, particularly if there is a variable amount of VSGs that can contribute to the MIR continuum at $\sim$20 $\mu$m. Future work with DustEM and The Heterogeneous dust Evolution Model for Interstellar Solids (THEMIS) model (Compiègne et al. 2011; Jones et al. 2013; Ysard et al. 2024) could explore $R_{\rm PAH}$ as a tracer of small hydrocarbon grain abundance in that model framework, which includes variable VSG abundance.

In addition, in our FIR modeling comparison and exploration of the model predictions for $R_{\rm PAH}$–$q_{\rm PAH}$ mapping, we have assumed a radiation field distribution (specifically, a delta function plus power-law model). This choice directly impacts the interpretation of the MIR emission, since the power-law component (with a distribution of radiation fields extending from $U_{\rm min}$ to $U = 10^7$ and a slope fixed to $\alpha = 2$) contributes MIR continuum emission at $\sim$20 $\mu$m. In models which assume a single radiation field that MIR emission is often attributed to changes in the grain size distribution (specifically, an increase in VSGs; see Figure 3.15 of Galliano 2022, for a very clear visualization of the differences between these types of models). The applicability of a delta function plus power-law distribution has been explored in a wide variety of contexts for unresolved galaxies or $\sim$kiloparsec-scale measurements (Dale et al. 2005; Aniano et al. 2012; Galliano et al. 2018). At a very high spatial resolution, in theory one might expect to reach a scale where a single radiation field may be applicable, but in general on 10–50 pc scales it seems likely that a distribution of radiation field intensities is present. Little is known about the detailed small-scale distribution of radiation field intensities throughout the ISM. Future work investigating this will be critical to improve understanding of the $R_{\rm PAH}$–$q_{\rm PAH}$ mapping and for reconciling differences between models that interpret the MIR continuum as changes in small grain abundance, PAH fraction, and radiation field intensity and distribution.

### 5.2. The Destruction of PAHs in H II Regions

H II regions crisply stand out in our $R_{\rm PAH}$ maps as regions with low PAH fraction. This observation agrees well with previous studies in MW H II regions (e.g., Cesarsky et al. 1996; Kassis et al. 2006; Povich et al. 2007), with extragalactic observations that have the spatial resolution to isolate H II regions (e.g., Chastenet et al. 2019), and with early results on JWST observations of our sample (Chastenet et al. 2023a; Egorov et al. 2023). Additionally, this follows from the trends between sSFR (measured by 70 $\mu$m surface brightness) and $q_{\rm PAH}$ measured at lower spatial resolution described in Aniano et al. (2020). When we separate "nebular" regions using the Groves et al. (2023) catalog, we find that these boundaries encompass nearly all of the low-$R_{\rm PAH}$ regions in our maps. We also find that the $R_{\rm PAH}$ weighted by H$\alpha$ shows an even more dramatic decrease in the nebular regions. To confirm this result is valid even if some H II regions were not included in the nebular catalog of Groves et al. (2023), we also examine trends in $R_{\rm PAH}$ as a function of $I_{\rm H\alpha}/\Sigma_{\rm HI+H_2}$, a pixel-based tracer of the amount of ionized gas, and find that $R_{\rm PAH}$ falls dramatically at a value of $I_{\rm H\alpha}/\Sigma_{\rm HI+H_2} = 37.5\,{\rm erg\,s^{-1}\,kpc^{-2}}\,(M_\odot\,{\rm pc^{-2}})^{-1}$, confirming that $R_{\rm PAH}$ decreases in regions dominated by ionized gas.

The good correspondence of the presence of H II regions with the decrease in $R_{\rm PAH}$ across a sample of H II regions with a wide range of ages and luminosities suggests that PAH destruction occurs quickly compared to the H II-region lifetime. Indeed, observations of PAH emission in MW H II regions suggest PAH survival times on the order of $\sim$few thousand years (Kassis et al. 2006; Compiègne et al. 2007) inside the ionization front. Recent JWST observations of the Orion Bar photodissociation region (PDR) have emphasized the sharp decrease in PAH emission near the ionization front (Chown et al. 2024; Peeters et al. 2024), corroborating a quick destruction timescale in the photoionized gas.

The exact mechanism of PAH destruction in H II regions is not fully understood. Laboratory studies of PAHs have suggested that fragmentation of PAH molecules is likely to occur when they are irradiated by photons with energies between 8 and 40 eV, although there is some uncertainty as to what photon energies will primarily fragment PAHs and which energies will lead only to photoionization of the PAHs (Jochims et al. 1996; Zhen et al. 2015). Theoretical calculations suggest that in photoionized gas with H II-region-like densities,

thermal sputtering would require long timescales ($\sim 10^7$ yr; Micelotta et al. 2010), which would be difficult to reconcile with the strong correspondence between H II region locations and dips in $R_{\rm PAH}$ across our large sample of regions. Observations of MW H II regions provide evidence for extreme-UV photons playing an important role in PAH destruction (Povich et al. 2007). Comparison of optical line ratios from MUSE to the regions of low $R_{\rm PAH}$ in the PHANGS-JWST targets also show $R_{\rm PAH}$ is correlated with tracers of the hardness and intensity of the UV field (Egorov et al. 2023). More detailed investigation of the correlation of $R_{\rm PAH}$ and PAH properties judged from spectroscopy with tracers of the ionized gas conditions and radiation field should provide key insights into the destruction pathways.

Because of the resolution of the MUSE and JWST data, our nebular regions always include contributions from both the H II region surrounding PDR and, depending on the H II-region size and galaxy distance and inclination, a substantial contribution from the surrounding "diffuse" gas. This means that the low-$R_{\rm PAH}$ signal associated with H II regions is diluted, particularly for small H II regions (see Section 4.1.3 for more discussion). Future work comparing the $R_{\rm PAH}$ maps to high-resolution H$\alpha$ from HST observations or Paschen-$\alpha$ from JWST should better resolve the boundary of the H II region, enabling less contaminated measurements of the decrease in $R_{\rm PAH}$. We do see, however, that in cases where the H II regions are large or the line of sight is dominated by ionized gas (see Figure 10) the decrease in $R_{\rm PAH}$ is more stark. This is likely to be a combination of a better match between the MUSE nebular region and the actual H II-region size, and the fact that large H II regions may be big enough to fully puncture through the galaxy disks, giving a line of sight that has little foreground or background contamination from the surrounding neutral ISM. It is worth noting that in the case of $q_{\rm PAH} \sim 0$, $R_{\rm PAH}$ does not asymptote to zero, but something more like $R_{\rm PAH} \sim 0.5$ in the Draine & Li (2007) and Hensley & Draine (2023) models. The nature of the MIR continuum in situations where there are truly no PAHs is not well characterized since few lines of sight with those characteristics have been studied in the tracers needed to constrain the grain population in the MW. Observations with Spitzer and SOFIA of Galactic H II regions NGC 7023 (Croiset et al. 2016) and the Eagle Nebula (Flagey et al. 2011) show little to no PAH emission inside the PDRs, but these observations were not the main comparison source for the Draine & Li (2007) and Hensley & Draine (2023) models. This means that at very low $q_{\rm PAH}$, the $q_{\rm PAH}$–$R_{\rm PAH}$ mapping may be more uncertain. Regardless, it is clear that we see the lowest $R_{\rm PAH}$ values in lines of sight that are most dominated by ionized gas. Our observations are consistent with a picture where ionized gas is essentially free of PAHs, as would be expected based on observations of MW H II regions and estimates of the PAH destruction timescale.

The observation that H II regions are holes in the distribution of PAHs in the ISM provides a potential explanation for the observed trends of kiloparsec-scale $q_{\rm PAH}$ and $R_{\rm PAH}$ with SFR and sSFR (e.g., Aniano et al. 2020). As the SFR surface density increases, a larger fraction of the ISM in that kiloparsec is comprised of H II regions, leading to a lower average PAH fraction. Also, because the kiloparsec-scale averages are luminosity weighted, and the surroundings of H II regions have some of the highest MIR luminosities, low-$q_{\rm PAH}$ material will contribute more to setting the kiloparsec-average $R_{\rm PAH}$. An interesting consequence of the SFR or sSFR trends in $R_{\rm PAH}$ may be to exaggerate the observed dependence of $q_{\rm PAH}$ on metallicity. Because low-metallicity galaxies tend to have low stellar mass, and therefore have higher sSFR (and in particular many of the low-metallicity galaxies previously studied in the MIR are starbursts with very high sSFR; Wu et al. 2006; Engelbracht et al. 2008), some part of the observed metallicity trend may in fact be a sSFR trend. Future JWST observations should be able to clearly disentangle these two effects by resolving the $R_{\rm PAH}$ maps of these sources and isolating the H II regions from the surrounding neutral ISM.

### 5.3. PAH Fraction as a Function of Metallicity

One of the strongest observed environmental trends in PAH fraction is its dependence on metallicity (Engelbracht et al. 2005; Madden et al. 2006; Draine et al. 2007; Rémy-Ruyer et al. 2015; Chastenet et al. 2019; Shivaei et al. 2024). Galaxy-integrated $q_{\rm PAH}$ measurements suggest a decrease in the PAH fraction at $12 + \log({\rm O/H}) \sim 8.1$–$8.3$ (Draine et al. 2007; Aniano et al. 2020; Galliano et al. 2021). This decline has been attributed to enhanced PAH destruction (Madden et al. 2006; Gordon et al. 2008) or impeded PAH formation (Sandstrom et al. 2010) at low metallicity, among other possibilities. Observations of the Magellanic Clouds have revealed that at 10 pc resolution, where H II regions and diffuse gas can be separated, the diffuse neutral gas PAH fraction shows a sharp decrease between the metallicity of the LMC and SMC, and that the diffuse neutral gas in the LMC has a nearly MW $q_{\rm PAH}$ value of $\sim$5% (Chastenet et al. 2019).

Understanding the origin of this metallicity trend is critical for using PAH emission to trace SF and for predicting attenuation curves for galaxies across a range of metallicities and redshifts. It also holds key information about the PAH life cycle—a subject that remains poorly understood. As discussed in Aniano et al. (2020), the galaxy-integrated $q_{\rm PAH}$ measurements as a function of metallicity do not provide a clear distinction between a model where the PAH fraction decreases gradually with metallicity or where there is a sharp decrease at some threshold metallicity.

Although our sample does not span a large metallicity range, nor does it reach the $12 + \log({\rm O/H}) \sim 8.1$–$8.3$ metallicities where the PAH fraction becomes substantially lower than the MW, our observations of a nearly constant $R_{\rm PAH,Diffuse}$ throughout our sample suggest that metallicity trends are steep rather than gradual. We see no clear metallicity trends in $R_{\rm PAH,Diffuse}$ over $\sim$0.3 dex in $12 + \log({\rm O/H})$, and in fact one of our lowest-metallicity galaxies has one of the highest $R_{\rm PAH,Diffuse}$ values. The lack of any systematic metallicity trend may lend some support to the scenario where there is a sharp drop in $q_{\rm PAH}$ at some metallicity. This agrees well with the LMC results (Chastenet et al. 2019) showing a MW-like $q_{\rm PAH}$ in the diffuse neutral gas of that galaxy, despite its low metallicity. An important future direction for understanding PAH fraction as a function of metallicity is to separate $R_{\rm PAH}$ in H II regions and diffuse gas in lower-metallicity targets. If the metallicity dependence is sharp, we may expect to see $R_{\rm PAH,Diffuse}$ in galaxies persist at high values until some threshold metallicity.

### 5.4. Behavior of the PAH Fraction outside H II Regions

Outside of the H II regions identified with the nebular catalogs of Groves et al. (2023), we find that $R_{\rm PAH}$ is fairly constant, with an average value of ∼3.4. Based on the dust-emission models of Hensley & Draine (2023), this corresponds to a $q_{\rm PAH}$ of 5.55%, assuming the "standard" PAH size distribution and a single radiation field with $U = 1$. The $q_{\rm PAH}$ calibration in Hensley & Draine (2023) places the MW diffuse ISM at $q_{\rm PAH} = 5.9\%$, very similar to what we infer in the diffuse ISM of galaxies in our sample. If we instead translate $R_{\rm PAH}$ to $q_{\rm PAH}$ using a distribution of radiation fields with $U_{\rm min} = 1$ and $\gamma = 0.005$ in the Draine & Li (2007) models, we find that $R_{\rm PAH} = 3.4$ translates to $q_{\rm PAH} \sim 4.5$–5 (see Figure 7). Within the Draine & Li (2007) models, the MW diffuse ISM $q_{\rm PAH} = 4.55\%$, again very similar to what we infer for our galaxies. These comparisons suggest that we are seeing $q_{\rm PAH}$ values in the diffuse neutral gas of our galaxies that is very similar to what is found in the MW. In addition, the consistency of $R_{\rm PAH}$ outside of nebular regions suggests that the diffuse ISM of these galaxies has a fairly uniform $q_{\rm PAH}$. The small degree of environmental variation at ∼solar metallicity in PAH fraction also helps explain observations showing a tight, nearly linear correlation of PAH emission with gas column (Chown et al. 2021; Leroy et al. 2023b). This is similar to what has been found in the MW, where gas column and dust emission are tightly correlated in the high-latitude cirrus (Boulanger et al. 1996; Planck Collaboration et al. 2011; Lenz et al. 2017).

The most significant driver of changes to the average value of $R_{\rm PAH,Diffuse}$ across our sample is the sSFR, a correlation that we tested both over the full JWST footprint (Figure 9) and within 1 kpc regions (Figure 11). The positive correlation between $R_{\rm PAH,Diffuse}$ and sSFR could be explained if regions with higher sSFR have an overall harder radiation field in the diffuse ISM compared to lower-sSFR regions, which would increase the $R_{\rm PAH}$ measured in the diffuse gas at a given $q_{\rm PAH}$. Future efforts to model the ISRF using information from the stellar populations observed by MUSE should provide important insights into these trends. In addition, studies of $R_{\rm PAH}$ in the vicinity of star clusters, where the radiation field can be predicted with stellar population modeling, show trends consistent with $R_{\rm PAH}$ responding to changes in radiation field hardness (Dale et al. 2023a; D. A. Dale et al. 2024, in preparation). Lastly, work with PHANGS-JWST exploring PAH band ratios has shown evidence of the dependence of PAH emission feature strengths on the hardness of the radiation field (Chastenet et al. 2023b; Baron et al. 2024). Accounting for the response of PAH emission to changes in radiation field spectrum will be a critical next step in interpreting $R_{\rm PAH}$ variations.

In addition to the correlation between $R_{\rm PAH,Diffuse}$ and sSFR, we see a slight decreasing trend in $R_{\rm PAH,Diffuse}$ and $f_{\rm Mol}$. This decrease could be explained by PAHs coagulating or sticking to larger dust grains in the dense gas. Ysard et al. (2013) suggest that coagulation of dust grains will occur above a density threshold of a few $10^3$ H cm$^{-3}$. Above this threshold, smaller grains may form fluffy aggregates, producing a different dust population than in the lower-density diffuse ISM and lowering $q_{\rm PAH}$. This aggregation could potentially cause some of the decrease in $R_{\rm PAH,Diffuse}$ we observe at high $f_{\rm Mol}$, where we expect the gas to be the densest. Additionally, or alternatively, in regions of dense molecular gas, $A_V$ is expected to be highest, blocking UV light that would excite PAHs from reaching these regions. This high attenuation of UV light could also be lowering $R_{\rm PAH}$ even if $q_{\rm PAH}$ remains constant; it softens the radiation field, leading to lower $R_{\rm PAH}$ at a given $q_{\rm PAH}$. Determining whether the main cause of this decreasing trend is coagulation or UV attenuation requires further spectral information not available with this data set. This trend appears consistent across our full sample, with the exceptions of NGC 1300 and NGC 5068, which show slight increases in $R_{\rm PAH,Diffuse}$ at high $f_{\rm Mol}$.

It should also be noted that our isolation of $R_{\rm PAH}$ from diffuse gas is limited by our ability to identify H II regions with MUSE. Some of the decrease observed in $R_{\rm PAH,Diffuse}$ at high $f_{\rm Mol}$ could be caused by embedded star-forming regions undetected by MUSE (as found in a small set of cases in Hassani et al. 2023). These embedded regions would decrease $R_{\rm PAH,Diffuse}$ through PAH destruction, as observed in the lower $R_{\rm PAH,Neb}$ measurements above. The magnitude of this effect is likely to be limited by the short duration of this highly embedded phase of star formation (Kim et al. 2023) and the overall excellent correspondence between 21 $\mu$m sources and H$\alpha$ (with 92% of F2100W bright sources falling within an identified nebular region; Hassani et al. 2023).

## 6. Summary

This work represents an in-depth analysis of the JWST photometry-based indicator of the fraction of dust in the form of PAHs: $R_{\rm PAH} = ({\rm F770W_{ss}} + {\rm F1130W})/{\rm F2100W}$. Using MIRI photometric maps of 19 nearby galaxies from the PHANGS sample, we are able to assess the behavior of $R_{\rm PAH}$ in a wide variety of ISM environments. Through this initial analysis, we provide the necessary verification that $R_{\rm PAH}$ as defined in this work is a robust tracer of the PAH fraction. We determine this through comparisons between $R_{\rm PAH}$ and $q_{\rm PAH}$, the PAH fraction as defined by the Draine & Li (2007) dust models. Model predictions of $R_{\rm PAH}$ increase with $q_{\rm PAH}$ up to a $q_{\rm PAH}$ of $\gtrsim$5%−6% using the dust-emission models of both Hensley & Draine (2023) and Draine & Li (2007), assuming reasonable radiation field properties (both single radiation fields and distributions of radiation field intensity) for 10–50 pc scales in galaxies. Above a $q_{\rm PAH}$ of ∼5%–6%, the modeled relationship between $R_{\rm PAH}$ and $q_{\rm PAH}$ continues to increase with a slightly flatter slope in both the Hensley & Draine (2023) and Draine & Li (2007) models, for a range of PAH size or charge distributions and ISRFs. We also compare observed values of $R_{\rm PAH}$ and $q_{\rm PAH}$ at low resolution for galaxies with both JWST and FIR observations, and find good correlation. Based on this behavior, we argue that $R_{\rm PAH}$ is a good indicator of PAH fraction in most typical ISM conditions observable at $\geqslant$10 pc scales. Across our sample, we find $\langle R_{\rm PAH,Diffuse}\rangle = 3.43$, which closely corresponds to the $R_{\rm PAH}$ values predicted for the MW of $q_{\rm PAH} \sim 5.9\%$ listed in the Hensley & Draine (2023) models or $q_{\rm PAH} \sim 4.6$ listed in the Draine & Li (2007) models.

We use $R_{\rm PAH}$ to assess the PAH fraction across the disks of the 19 PHANGS galaxies, and look for correlations with environment through comparisons to optical, millimeter, and submillimeter observations available in the PHANGS data set. We find that the dominant change in $R_{\rm PAH}$ is a steep decrease observed in H II regions, as noted both by lower average values of $R_{\rm PAH}$ within nebular regions and a sharp decrease in $R_{\rm PAH}$ above a $\log_{10}(I_{\rm H\alpha}/\Sigma_{\rm HI+H_2})$ of $\sim$37.5 erg s$^{-1}$ kpc$^{-2}$ $(M_\odot\,{\rm pc}^{-2})^{-1}$. The exact destruction mechanism of PAHs within H II regions is not well known, but is likely caused by

the UV radiation from young stars. The good correspondence between the low $R_{\rm PAH}$ values and the nebular regions, which span a wide range of ages and luminosities, suggest that PAH destruction occurs quickly compared to the H II-region lifetime.

We also find that the difference between the average $R_{\rm PAH}$ measured in nebular regions and the diffuse gas is correlated with the sSFR. This trend seems to be driven by the correlation between $\langle R_{\rm PAH,Diffuse}\rangle$ and sSFR, which was observed in 1 kpc regions and when examining the integrated measurements from the full area mapped by JWST. This could indicate that in galaxies with the highest sSFR, a harder radiation field is irradiating the PAHs in the diffuse ISM, producing a higher value of $R_{\rm PAH}$ for a given $q_{\rm PAH}$.

We further test what may affect the PAH abundance outside H II regions by examining how $R_{\rm PAH,Diffuse}$ changes as a function of galactic environment (nuclei, arms, bars, etc.), molecular gas fraction, and metallicity. We find little variation of $R_{\rm PAH}$ with metallicity, although this is likely caused by the limited range of $12 + \log({\rm O/H})$ covered by our sample. Within the metallicity range included in our sample, there is some indication of a slight decrease in the binned median values of $R_{\rm PAH,Diffuse}$ below $12 + \log_{10}({\rm O/H}) \sim 8.4$, but as only five galaxies in our sample have $Z$ lower than this threshold it is difficult to ascertain the veracity of this trend. We find a slight decrease in $R_{\rm PAH,Diffuse}$ with the molecular gas fraction $f_{\rm Mol}$, which could be caused by the PAHs forming into larger grains and decreasing the PAH fraction in denser gas or attenuation of UV photons that would excite PAH features, limiting the PAH emission in this ISM phase.

This paper lays the groundwork for using MIRI photometry to trace the PAH fraction at 10–50 pc scales in nearby galaxies. JWST has opened a new window for studying the distribution of PAHs at high sensitivity and high spatial resolution. Further observations of nearby galaxies including dwarfs, starbursts, and early-type galaxies with JWST will continue to expand our understanding of how the PAH fraction both impacts and is impacted by its local environment.

## Acknowledgments

This work has been carried out as part of the PHANGS collaboration. This work is based on observations made with the NASA/ESA/CSA JWST. The data were obtained from the Mikulski Archive for Space Telescopes at the Space Telescope Science Institute, which is operated by the Association of Universities for Research in Astronomy, Inc., under NASA contract NAS 5-03127 for JWST. These observations are associated with program 2107. The specific observations analyzed can be accessed via doi:10.17909/ew88-jt15.

J.S. and K.S. acknowledge funding from JWST-GO-2107.006-A. R.S.K. and S.C.O.G. acknowledge funding from the European Research Council via the Synergy Grant "ECOGAL" (project ID 855130), from the German Excellence Strategy via the Heidelberg Cluster of Excellence (EXC 2181-390900948) "STRUCTURES," and from the German Ministry for Economic Affairs and Climate Action in project "MAINN" (funding ID 50OO2206). A.K.L., D.P., and R.C. gratefully acknowledge support by grants 1653300 and 2205628 from the National Science Foundation, by award JWST-GO-02107.009-A, JWST-GO-03707.001-A, JWST-GO-04256.001-A, and by a Humboldt Research Award from the Alexander von Humboldt Foundation. M.C. and L.R. gratefully acknowledge funding from the DFG through an Emmy Noether Research Group (grant No. CH2137/1-1). COOL Research DAO is a Decentralized Autonomous Organization supporting research in astrophysics aimed at uncovering our cosmic origins. O.E. and K.K. acknowledge funding from the Deutsche Forschungsgemeinschaft (DFG, German Research Foundation) in the form of an Emmy Noether Research Group (grant No. KR4598/2-1; PI: Kreckel) and the European Research Council's starting grant ERC StG-101077573 ("ISM-METALS"). M.B. acknowledges support by the ANID BASAL project FB210003 and by the French government through the France 2030 investment plan managed by the National Research Agency (ANR), as part of the Initiative of Excellence of Université Côte d'Azur under reference No. ANR-15-IDEX-01. J.C. acknowledges funding from the Belgian Science Policy Office (BELSPO) through the PRODEX project "JWST/MIRI Science exploitation" (C4000142239). E.W.K. acknowledges support from the Smithsonian Institution as a Submillimeter Array (SMA) Fellow and the Natural Sciences and Engineering Research Council of Canada. E.R. acknowledges the support of the Natural Sciences and Engineering Research Council of Canada (NSERC), funding reference number RGPIN-2022-03499.

This paper makes use of the following ALMA data: ADS/JAO.ALMA#2012.1.00650.S, ADS/JAO.ALMA#2013.1.01161.S, ADS/JAO.ALMA#2015.1.00925.S, ADS/JAO.ALMA#2017.1.00392.S, and ADS/JAO.ALMA#2017.1.00886.L. ALMA is a partnership of ESO (representing its member states), NSF (USA), and NINS (Japan), together with NRC (Canada), NSC and ASIAA (Taiwan), and KASI (Republic of Korea), in cooperation with the Republic of Chile. The Joint ALMA Observatory is operated by ESO, AUI/NRAO, and NAOJ. The National Radio Astronomy Observatory is a facility of the National Science Foundation operated under cooperative agreement by Associated Universities, Inc.

*Facilities:* JWST (MIRI), VLT:Yepun, ALMA, VLA, MeerKAT.

*Software:* astropy (Astropy Collaboration et al. 2013, 2018, 2022) `jwst` (Bushouse et al. 2023), `matplotlib` (Hunter 2007), `numpy` (Harris et al. 2020), `photutils` (Bradley et al. 2022), SAOImageDS9 (Joye & Mandel 2003), `scipy` (Virtanen et al. 2020), `pjpipe` (Williams et al. 2022).

## Appendix A
## Histograms for Individual Galaxies

To highlight differences observed between each galaxy, individual histograms for each of the nineteen galaxies are displayed in this Appendix. Figure 16 shows $R_{\rm PAH}$ as a function of $I(H\alpha)/\Sigma_{HI+H_2}$ for each galaxy, binned medians are displayed over the pixels, color-coded by sSFR, as in Figure 10. Figures 17 and 18 show $R_{\rm PAH,Diffuse}$ as a function of metallicity and molecular gas fraction, respectively. Finally, expanding on Figure 13, the distribution of $R_{\rm PAH,Diffuse}$ for individual environments in each galaxy are shown in Figure19.

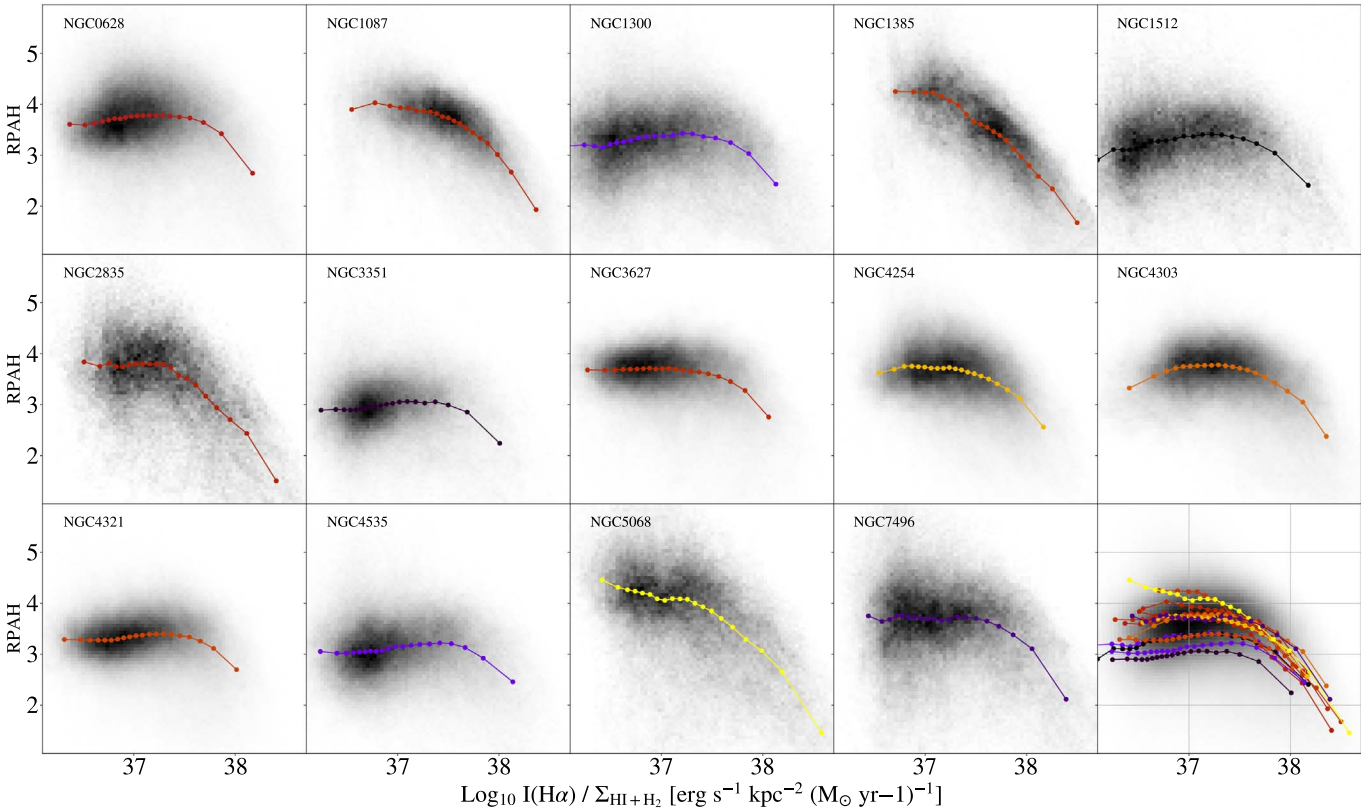


**Figure 16.** $R_{\rm PAH}$ plotted as a function of $I_{\rm H\alpha}/\Sigma_{\rm HI+H_2}$ for each galaxy with an H I map available. Binned medians are displayed in each panel. The final panel combines the binned medians from each galaxy for comparison. Medians are color-coded by increasing $\log_{10}$sSFR, using the same colors as in the main text.

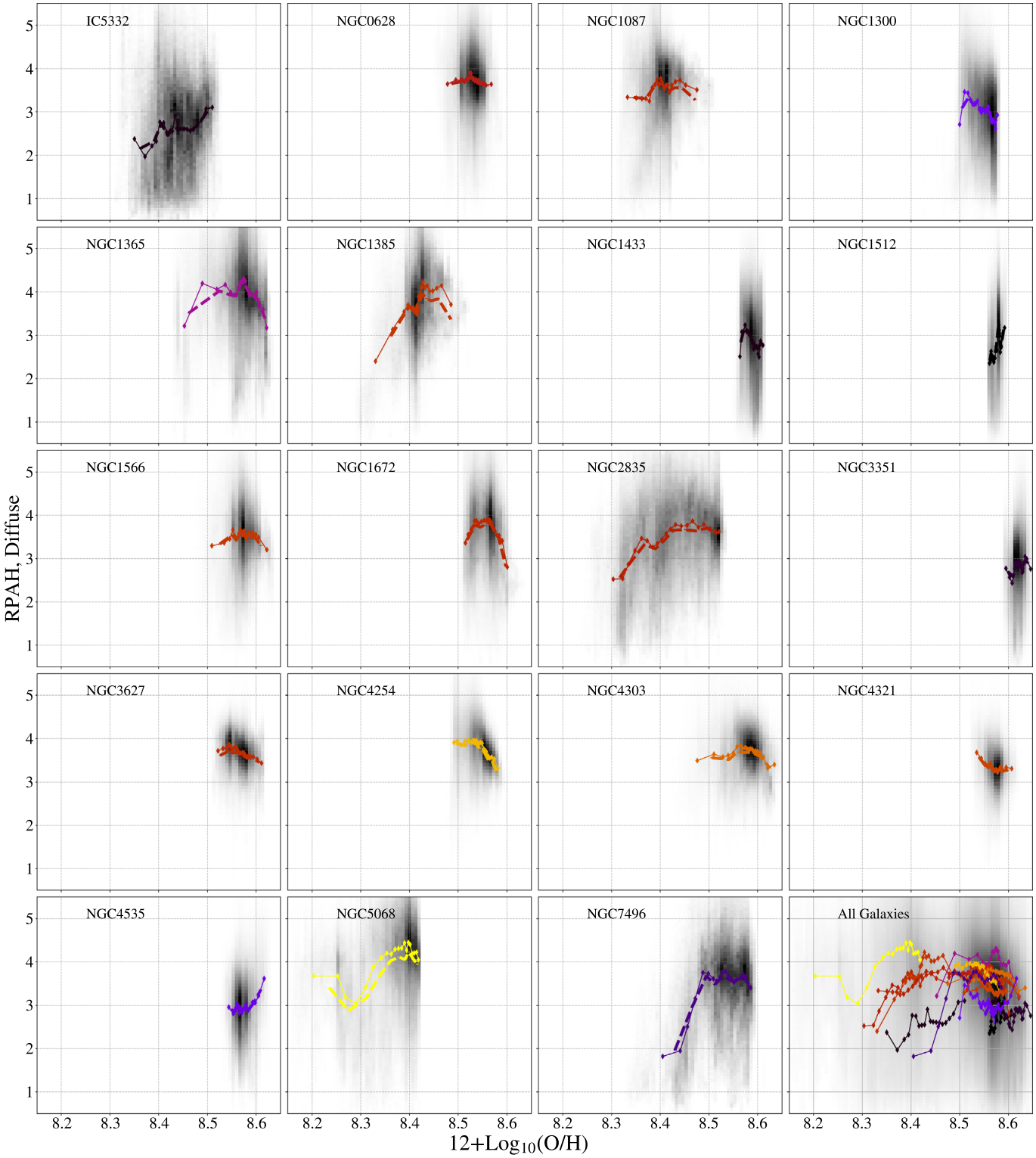


**Figure 17.** The per-pixel values of $R_{\rm PAH,Diffuse}$ plotted as a function of metallicity. Metallicities were determined using the metallicity maps of Williams et al. (2022). Binned medians are shown in each panel and plotted together in the final panel, color-coded by sSFR. Dashed lines represent the binned medians for all the measurements of $R_{\rm PAH}$.

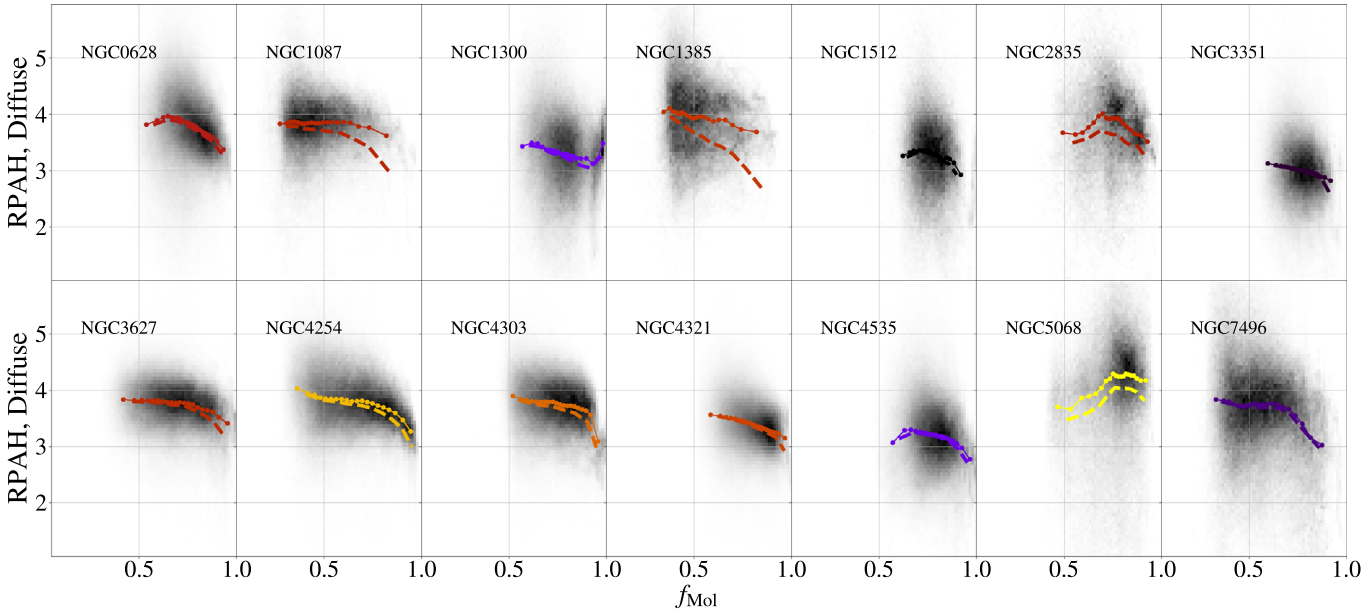


**Figure 18.** $R_{\rm PAH,Diffuse}$ plotted as a function of the molecular gas fraction, $f_{\rm Mol}$. $f_{\rm Mol}$ was determined using the $^{12}$CO (2–1)-derived $\Sigma_{\rm H_2}$ and H I-derived $\Sigma_{\rm HI}$. Binned medians are color-coded using the same sSFR schematic described in Figures 16 and 17. Dashed lines represent the binned medians for all the measurements of $R_{\rm PAH}$.

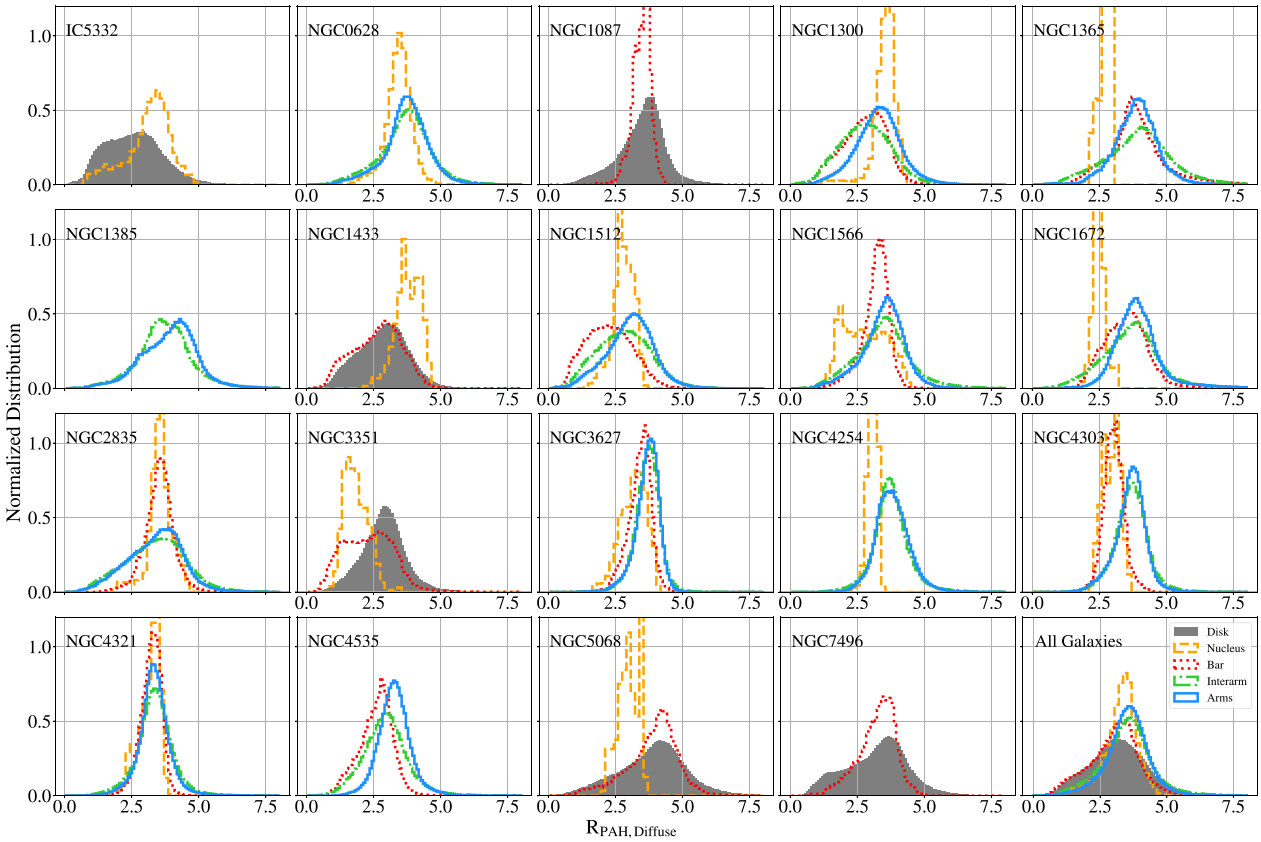


**Figure 19.** Histograms of $R_{\rm PAH,Diffuse}$ from isolated galactic environments as defined by Querejeta et al. (2021) for isolated galaxies. Gold histograms represent measurements from the nucleus, purple are spiral arms, green are interarm, red are bars, and black are disks without spiral arms.

## Appendix B
## $R_{\rm PAH}$ Alternatives

In some cases, only one of the PAH-dominated filters that we use in $R_{\rm PAH}$ may be available. In this appendix, we evaluate the relationship between $R_{\rm PAH}$ and F770W/F2100W and F1130W/F2100W to understand how well, empirically, these more restricted measurements can be expected to capture the full behavior seen in $R_{\rm PAH}$ in the main text. Although this paper uses the full (F770W+F1130W)/F2100W as a charge-agnostic PAH fraction tracer, we find that either F770W or F1130W

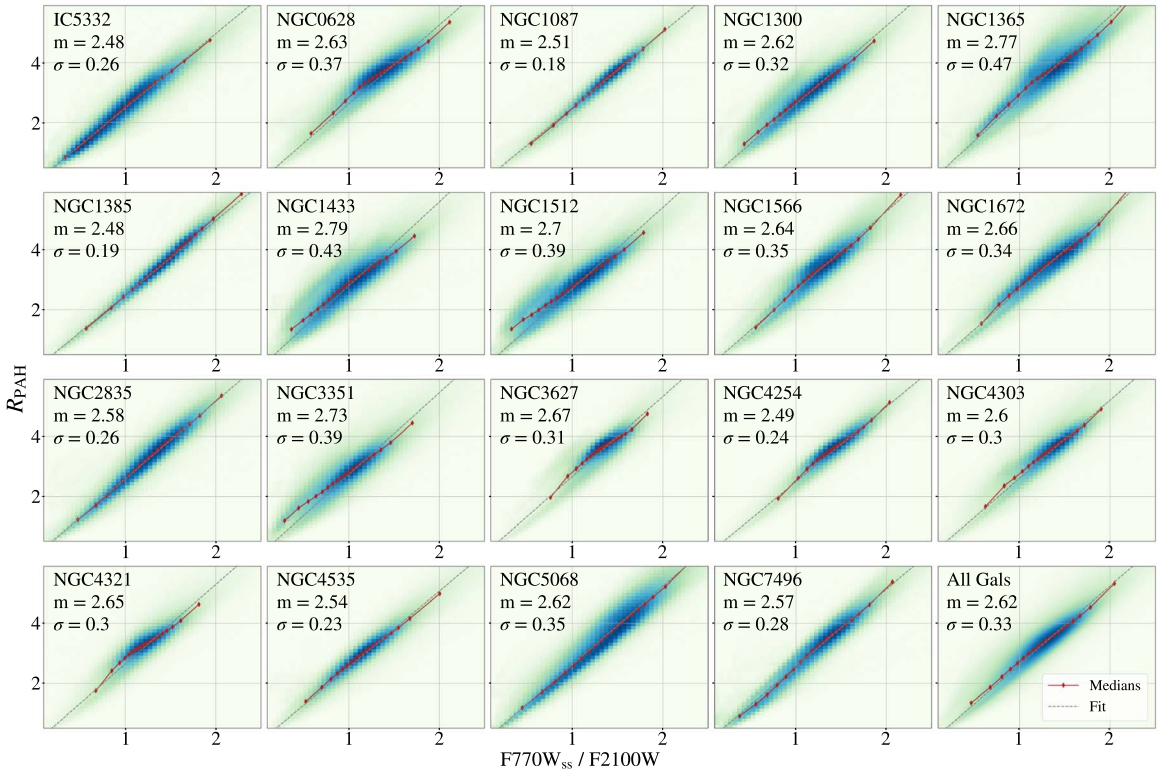


**Figure 20.** The relationship between F770W$_{ss}$/F2100W and $R_{PAH}$ for each galaxy in our sample, as well as the full sample in the last panel. Blue histograms show pixel distributions, red lines show binned medians, and the gray dashed lines show the best fit.

individually could be used as a good proxy for PAH emission, as shown by the strong correlations between $R_{PAH}$ and F770W/F2100W and F1130W/F2100W.

Figure 20 shows the relationship between $R_{PAH}$ and F770W$_{ss}$/F2100W. F770W$_{ss}$ is the F770W flux after starlight has been removed using the method described in Section 3.1. While the expected linear relationship is clear, we can see there are some galaxy-to-galaxy variations in the slope between $R_{PAH}$ and F770W$_{ss}$/F2100W. Across the full sample, we find $R_{PAH} = 2.57 \times$ (F770W$_{ss}$/F2100W), with a galaxy-to-galaxy $1\sigma$ scatter of 0.09 in the range of predicted slope values.

Figure 21 shows the relationship between F1130W/F2100W and $R_{PAH}$. Again, a reliable linear relationship is found between these two ratios, suggesting that F1130W/F2100W can provide constraints on the PAH fraction as well. For all pixels across our sample, we find $R_{PAH} = 1.59 \times$ (F1130W/F2100W), with a galaxy-to-galaxy $1\sigma$ scatter in the slope values of 0.04. While we recommend using $R_{PAH}$ as an indicator of the PAH fraction as it has less potential to be affected by the average charge of the dust grains (see, e.g., Draine & Li 2007; Draine et al. 2021), we find that both F770W$_{ss}$/F2100W and F1130W/F2100W provide viable alternatives.

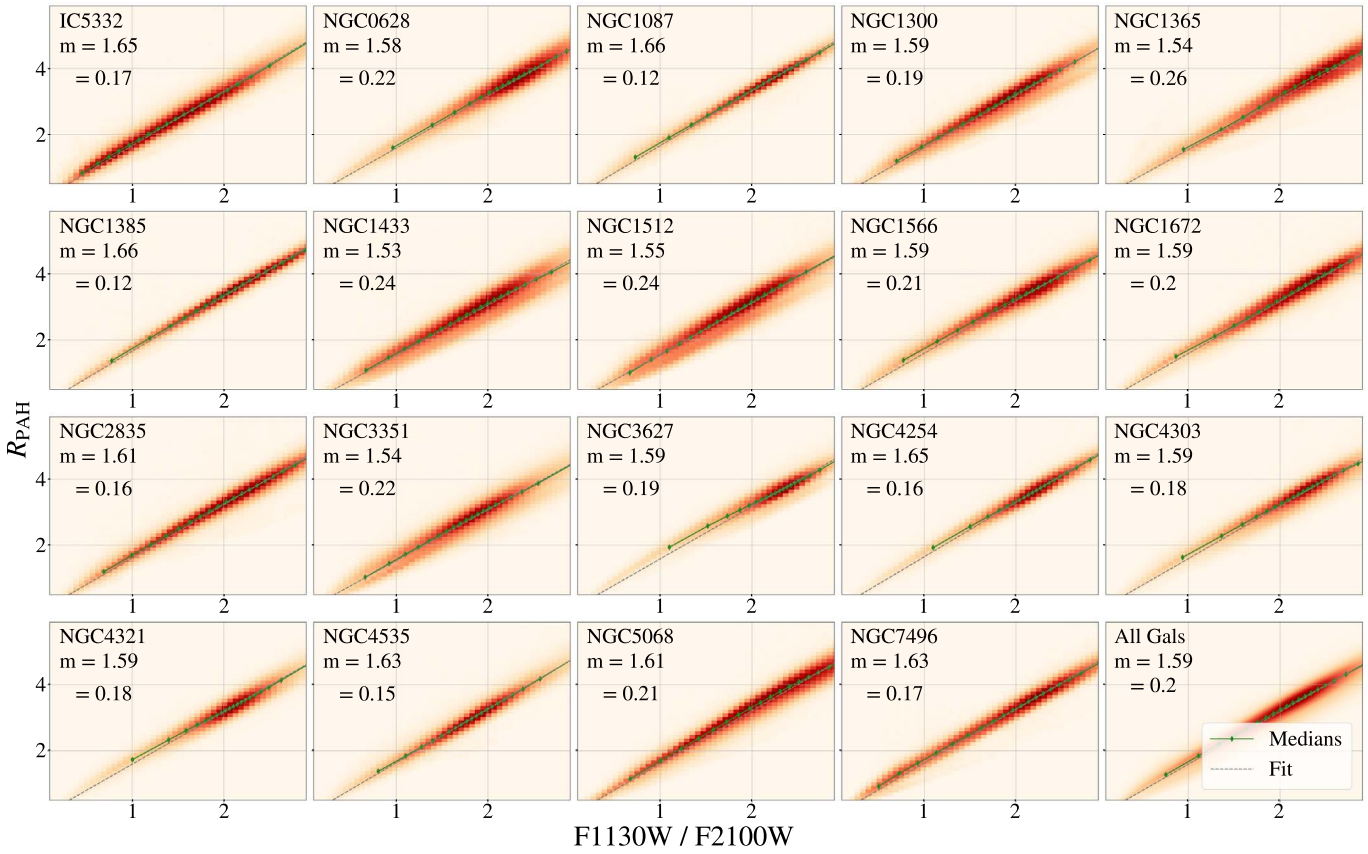


**Figure 21.** The relationship between F1130W/F2100W and $R_{PAH}$ for each galaxy in our sample, as well as the full sample in the last panel. The histograms represent all pixels, green lines represent binned medians, and gray lines represent the best fit of the form $R_{PAH} = m \times \frac{F1130W}{F2100W}$.

## Appendix C
## Dust Model Predictions of $R_{PAH}$

In addition to using the Draine & Li (2007) and Hensley & Draine (2023) dust models to determine the extent to which $R_{PAH}$ traces $q_{PAH}$ in Section 3.2, we also examined how changing the size and charge distribution of PAHs and the ISRF altered the value of $R_{PAH}$ produced by the Draine et al. (2021) dust models. These models provide nine PAH populations: three different size distributions (small, standard, and large) and three different ionization distributions (low, standard, and high). Each model includes the predicted PAH emission spectrum as well as the predicted spectrum of a population of larger dust grains (astrodust) for a range of ISRFs. We show the predicted values of $R_{PAH}$ determined for each of the size and charge distributions included in the Draine et al. (2021) models in Figure 22 for a range of possible ISRFs at $U = 1$. In addition, we show the predicted $R_{PAH}$ values for the THEMIS model (Jones et al. 2013) for two values of the incident far-ultraviolet radiation field, $G_0$. THEMIS $R_{PAH}$ predictions were computed using the standard distribution and summing the emission from the carbonaceous and silicate grains. All models produce $R_{PAH}$ between 4 and 6, matching our observations for areas with higher PAH fractions. This is expected for the Draine et al. (2021) models, which all assume a MW $q_{PAH}$ of 4.5%.

The overlap between points of different colors shows that changing the ionization state of the PAH population does not strongly influence measurements of $R_{PAH}$, which is expected as the 11.3 and 7.7 $\mu$m features trace neutral and ionized PAHs, respectively. The ISRF heating the PAHs has some effect on the predicted value of $R_{PAH}$. The range of ISRFs provided by the Draine et al. (2021) models are shown on the $x$-axis in order of relative radiation field hardness (harder radiation fields on the left, softer on the right). The first five ISRFs included are from the Bruzual & Charlot (2003, BC03) stellar population synthesis models for stellar populations of ages 3, 10, 100, 300 Myr, and 1 Gyr. The next ISRF, labeled mMMP, is a modified Mathis et al. (1983) ISRF which represents the average ISRF in the MW, and the final Draine et al. (2021) model shows PAHs illuminated by a ISRF matching the old stellar population found in the bulge of M31 (M31 Bulge). The next two models show the predicted values from the THEMIS dust model with a $G_0$ of 0.5 and 50.

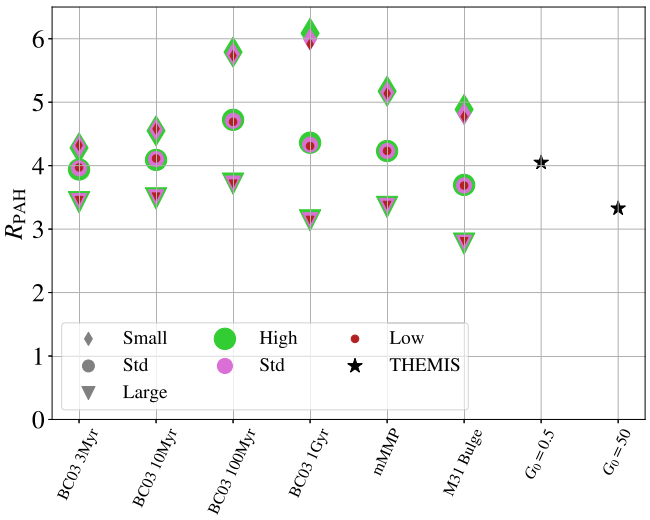


**Figure 22.** Predictions of $R_{PAH}$ for a range of available Draine et al. (2021) and THEMIS dust models. For the Draine et al. (2021) models we vary the size, charge, and ISRF heating the grains. For the THEMIS models we vary the $G_0$ of the radiation field heating the grains. All models produce $R_{PAH}$ between 3 and 6, matching values found in our data.

## Appendix D
## Flux Weighting versus Pixel Weighting

In order to represent the large amount of data included in this analysis, many of the figures in this paper displayed the binned averages of the data sets. It is worthwhile to note that there are multiple ways to determine the placement of these averages. For simplicity and uniformity, we have chosen to split the data up into bins of equal numbers of pixels and take the average value of all pixels in said bin. This is equivalent to giving each pixel in the bin an equal weight.

For quantities like $R_{PAH}$, which are ratios of other measurements, another method for placing the running averages would be summing the values of F770W+F1130W for each pixel in the bin and dividing by the summation of the F2100W values. This would be similar to taking a flux weighted average, as the pixels with the highest fluxes will have the greatest impact on the measured value. Figure 23 uses these two methods for determining the binned medians to recreate the relationship shown in Figure 16. Pink lines show the pixel-weighted medians, while yellow lines show the flux-weighted medians. The final panel displays the differences between the flux and pixel weighting.

We can see that in most cases the flux weighted average values are lower than the pixel-weighted values. This suggests that the brightest pixels that dominate the flux weighted average have lower $R_{PAH}$ measurements, likely driven by larger F2100W values. This is similar to what was found in Pathak et al. (2024), where they show that within areas of active star formation, the F2100W distribution has a relatively higher peak than the F770W and F1130W. These few bright pixels in F2100W dominate the F2100W total fluxes, lowering the flux weighted average $R_{PAH}$ measurements in comparison to the pixel weighted averages. This explains the differences in the average $R_{PAH}$ values shown in Figure 23. A more detailed analysis of the MIR flux distribution is presented in Pathak et al. (2024).

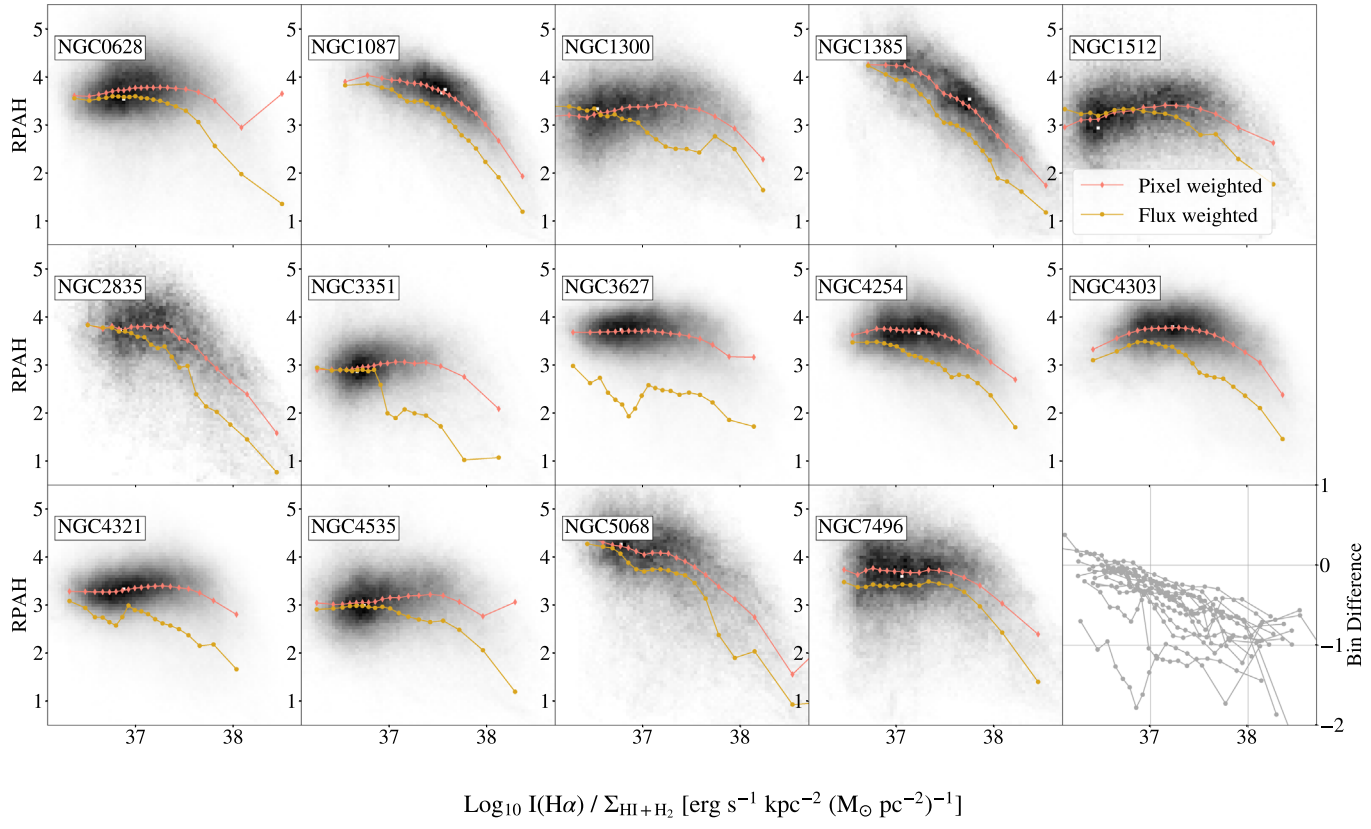


**Figure 23.** $R_{PAH}$ plotted as a function of $I_{H\alpha}/\Sigma_{HI+H_2}$ used to demonstrate the difference in using a pixel weighted average vs. a flux weighted average. The gray histograms show the full pixel distributions, while the salmon lines show the pixel-weighted binned medians and the yellow lines show the flux-weighted binned medians. The final panel shows the difference between the flux- and pixel-weighted binned medians. We can see that these values are primarily negative, driven by the brightest F2100W values dominating the flux weighted averages.

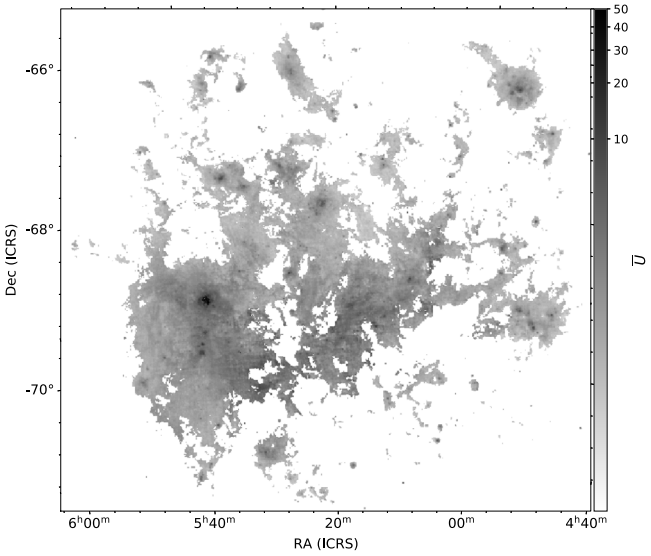


**Figure 24.** A map of the modeled $\overline{U}$ for the LMC. A log scale is used to better display the range of $\overline{U}$ found across the LMC. The star-forming region 30 Doradus has the highest values of $\overline{U}$, reaching $\overline{U} \gtrsim 30$.

## Appendix E
## Results from Previous 10 pc Far-IR SED Modeling

Although this work provides an unprecedented view of the PAH fraction in galaxies outside the Local Group, previous observations of the LMC with Spitzer and Herschel provide similar spatial resolution IR data. This allows for full FIR SED modeling. As these models are fit to both MIR and FIR data, they are able to include the emission from larger dust grains, which gives constraints on the radiation field heating the dust. Using these models as a guide, we can establish what range of radiation field intensities we might expect to be heating the dust at the 10–50 pc scales we measure within our sample.

Of particular interest is investigating the range of $\overline{U}$, the average radiation field in units of the Mathis et al. (1983) solar radiation field, that is heating the dust. Using the FIR SED models produced in Chastenet et al. (2019), we present a map of $\overline{U}$ for the LMC in Figure 24. Across this map, we find that $\overline{U}$ spans a range of ∼0–10 on 10 pc scales, with the exception of the starburst region 30 Doradus (where on scales $\ll$10 pc the radiation field intensity is very high, and where $\overline{U}$ reaches ∼50, the highest value of $\overline{U}$ measured in this map). This suggests that for the physical resolution we obtain using JWST for the galaxies presented in this work (∼10–50 pc), we can expect $\overline{U}$ to fall typically within the range ∼0–10, with some extreme star-forming regions potentially reaching a maximum $\overline{U}$ of ∼50.

This is relevant to our proposed use of $R_{\rm PAH}$ as a tracer of $q_{\rm PAH}$ because very high values of $U$ ($1 \times 10^2$ to $1 \times 10^4$; see Draine et al. 2021, their Figure 10) will push the peak of the blackbody emission produced by dust grains in equilibrium with the radiation field into the F2100W band, and at the highest values of $U$ ($1 \times 10^6$ to $1 \times 10^7$) the peak can even shift into the F1130W or F770W bands, and most grains are no longer stochastically heated. Large contributions of emission at F2100W from hot small grains in equilibrium with the radiation field would drive down $R_{\rm PAH}$ regardless of any changes to $q_{\rm PAH}$. Based on the modeled values of $\overline{U}$ found within the LMC at similar spatial resolution, it is unlikely that $U$ reaches the necessary values for this to happen within our sample. For this reason, we maintain that the decrease in $R_{\rm PAH}$ within the nebular regions is driven by PAH destruction, and not the increased intensity of the radiation field heating the dust.

Furthermore, by using these models of the IR SED of the LMC, we can test how the Spitzer-based photometric $q_{\rm PAH}$ tracer, IRAC4/MIP1, varies with changing $\overline{U}$. This is shown in the left panel of Figure 25. While there is a decreasing trend in IRAC4/MIPS1 with increasing $\log_{10}\overline{U}$, at low IRAC4/MIPS1 we can see that at these same values IRAC4/MIPS1 is still well correlated with $q_{\rm PAH}$. This suggests that the relationship observed between IRAC4/MIPS1 and $\log_{10}\overline{U}$ at these $\log_{10}\overline{U}$ values is caused by a change to $q_{\rm PAH}$, not a change to how the dust grains emit light. If we instead plot the trend between IRAC4/MIPS1 and $q_{\rm PAH}$, as shown in the right panel of this figure, we see a clear positive correlation. This suggests that at the 10 pc scales measured in these maps of the LMC, changes to $q_{\rm PAH}$ drive changes in IRAC4/MIPS1, while changes to $\overline{U}$ have only a small impact.

We note that the conclusions described above also depend on the assumption of a distribution of radiation fields heating the dust. In the delta function plus power-law radiation field model, a very small amount of dust heated by high radiation field intensities can contribute significantly to the MIR continuum emission at F2100W (see Figure 18 from Draine & Li 2007). In models that make different assumptions about the radiation field distribution (e.g., a single radiation field intensity), the mapping between $R_{\rm PAH}$ and $q_{\rm PAH}$ can differ significantly. Future studies that use different dust and radiation field models beyond Draine & Li (2007) with the delta function plus power-law model may draw different conclusions about the role the radiation field plays in interpreting $R_{\rm PAH}$.

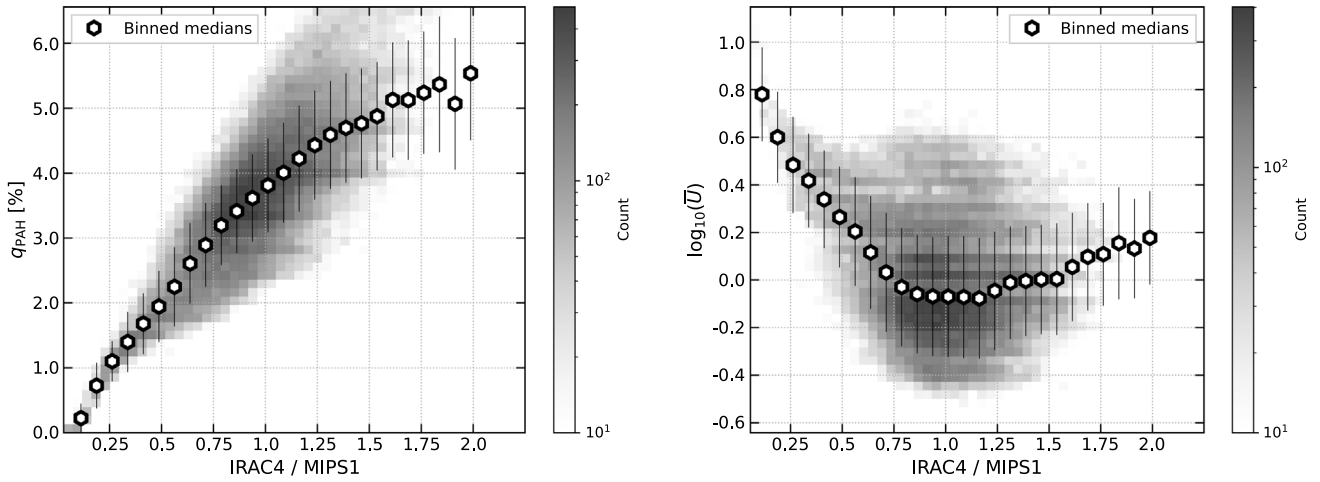


**Figure 25.** Left: modeled values of $q_{PAH}$ plotted as a function of IRAC4/MIPS1 fluxes. Here, the relationship between IRAC4/MIPS1 is clearly linear, suggesting that changes in this flux ratio are driven by changes in $q_{PAH}$, not changes in $U$, for the range of radiation fields measured at these 10 pc scales. Right: modeled values of $\log_{10}\overline{U}$ plotted as a function of IRAC4/MIPS1 fluxes. We can see a decreasing trend between $\overline{U}$ and the IRAC4/MIPS1 at low IRAC4/MIPS1 or low $q_{PAH}$. Despite this trend at low IRAC4/MIPS1, $q_{PAH}$ is still well correlated with IRAC4/MIPS1 at similar values.

## ORCID iDs

Jessica Sutter https://orcid.org/0000-0002-9183-8102
Karin Sandstrom https://orcid.org/0000-0002-4378-8534
Jérémy Chastenet https://orcid.org/0000-0002-5235-5589
Adam K. Leroy https://orcid.org/0000-0002-2545-1700
Eric W. Koch https://orcid.org/0000-0001-9605-780X
Thomas G. Williams https://orcid.org/0000-0002-0012-2142
Ryan Chown https://orcid.org/0000-0001-8241-7704
Francesco Belfiore https://orcid.org/0000-0002-2545-5752
Frank Bigiel https://orcid.org/0000-0003-0166-9745
Médéric Boquien https://orcid.org/0000-0003-0946-6176
Yixian Cao https://orcid.org/0000-0001-5301-1326
Mélanie Chevance https://orcid.org/0000-0002-5635-5180
Daniel A. Dale https://orcid.org/0000-0002-5782-9093
Oleg V. Egorov https://orcid.org/0000-0002-4755-118X
Simon C. O. Glover https://orcid.org/0000-0001-6708-1317
Brent Groves https://orcid.org/0000-0002-9768-0246
Ralf S. Klessen https://orcid.org/0000-0002-0560-3172
Kathryn Kreckel https://orcid.org/0000-0001-6551-3091
Kirsten L. Larson https://orcid.org/0000-0003-3917-6460
Elias K. Oakes https://orcid.org/0000-0002-0119-1115
Debosmita Pathak https://orcid.org/0000-0003-2721-487X
Lise Ramambason https://orcid.org/0000-0002-9190-9986
Erik Rosolowsky https://orcid.org/0000-0002-5204-2259
Elizabeth J. Watkins https://orcid.org/0000-0002-7365-5791

## References

Allamandola, L. J., Tielens, A. G. G. M., & Barker, J. R. 1989, ApJS, 71, 733
Anand, G. S., Lee, J. C., Van Dyk, S. D., et al. 2021, MNRAS, 501, 3621
Aniano, G., Draine, B. T., Calzetti, D., et al. 2012, ApJ, 756, 138
Aniano, G., Draine, B. T., Gordon, K. D., & Sandstrom, K. 2011, PASP, 123, 1218
Aniano, G., Draine, B. T., Hunt, L. K., et al. 2020, ApJ, 889, 150
Armus, L., Lai, T., U. V., et al. 2023, ApJL, 942, L37
Astropy Collaboration, Price-Whelan, A. M., Lim, P. L., et al. 2022, ApJ, 935, 167
Astropy Collaboration, Price-Whelan, A. M., Sipőcz, B. M., et al. 2018, AJ, 156, 123
Astropy Collaboration, Robitaille, T. P., Tollerud, E. J., et al. 2013, A&A, 558, A33
Barnes, A. T., Chandar, R., Kreckel, K., et al. 2022, A&A, 662, L6
Baron, D., Sandstrom, K. M., Rosolowsky, E., et al. 2024, ApJ, 968, 24
Belfiore, F., Leroy, A. K., Sun, J., et al. 2023, A&A, 670, A67
Bigiel, F., & Blitz, L. 2012, ApJ, 756, 183
Boquien, M., Burgarella, D., Roehlly, Y., et al. 2019, A&A, 622, A103
Boulanger, F., Abergel, A., Bernard, J. P., et al. 1996, A&A, 312, 256
Bradley, L., Sipőcz, B., Robitaille, T., et al. 2022, astropy/photutils: v1.5.0, Zenodo, doi:10.5281/zenodo.6825092
Bruzual, G., & Charlot, S. 2003, MNRAS, 344, 1000
Bushouse, H., Eisenhamer, J., Dencheva, N., et al. 2023, JWST Calibration Pipeline, v1.11.3, Zenodo, doi:10.5281/zenodo.8157276
Calzetti, D., Armus, L., Bohlin, R. C., et al. 2000, ApJ, 533, 682
Calzetti, D., Kennicutt, R. C., Engelbracht, C. W., et al. 2007, ApJ, 666, 870
Cappellari, M., & Emsellem, E. 2004, PASP, 116, 138
Cesarsky, D., Lequeux, J., Abergel, A., et al. 1996, A&A, 315, L309
Chabrier, G. 2003, PASP, 115, 763
Chastenet, J., Sandstrom, K., Chiang, I.-D., et al. 2019, ApJ, 876, 62
Chastenet, J., Sandstrom, K., Chiang, I.-D., et al. 2021, ApJ, 912, 103
Chastenet, J., Sutter, J., Sandstrom, K., et al. 2023a, ApJL, 944, L11
Chastenet, J., Sutter, J., Sandstrom, K., et al. 2023b, ApJL, 944, L12
Chown, R., Li, C., Parker, L., et al. 2021, MNRAS, 500, 1261
Chown, R., Sidhu, A., Peeters, E., et al. 2024, A&A, 685, A75
Ciesla, L., Boquien, M., Boselli, A., et al. 2014, A&A, 565, A128
Compiègne, M., Abergel, A., Verstraete, L., et al. 2007, A&A, 471, 205
Compiègne, M., Verstraete, L., Jones, A., et al. 2011, A&A, 525, A103
Cortzen, I., Garrett, J., Magdis, G., et al. 2019, MNRAS, 482, 1618
Croiset, B. A., Candian, A., Berné, O., & Tielens, A. G. G. M. 2016, A&A, 590, A26
Croxall, K. V., Smith, J. D., Wolfire, M. G., et al. 2012, ApJ, 747, 81
Dale, D. A., Bendo, G. J., Engelbracht, C. W., et al. 2005, ApJ, 633, 857
Dale, D. A., Boquien, M., Barnes, A. T., et al. 2023a, ApJL, 944, L23
Dale, D. A., Boquien, M., Turner, J. A., et al. 2023b, AJ, 165, 260
Dale, D. A., Cohen, S. A., Johnson, L. C., et al. 2009, ApJ, 703, 517
Dale, D. A., Helou, G., Contursi, A., Silbermann, N. A., & Kolhatkar, S. 2001, ApJ, 549, 215
Dale, D. A., Helou, G., Magdis, G. E., et al. 2014, ApJ, 784, 83
den Brok, J. S., Bigiel, F., Sliwa, K., et al. 2022, A&A, 662, A89
Draine, B. T. 2003, ARA&A, 41, 241
Draine, B. T., Aniano, G., Krause, O., et al. 2014, ApJ, 780, 172
Draine, B. T., Dale, D. A., Bendo, G., et al. 2007, ApJ, 663, 866
Draine, B. T., & Li, A. 2001, ApJ, 551, 807
Draine, B. T., & Li, A. 2007, ApJ, 657, 810
Draine, B. T., Li, A., Hensley, B. S., et al. 2021, ApJ, 917, 3
Egorov, O. V., Kreckel, K., Sandstrom, K. M., et al. 2023, ApJL, 944, L16
Emsellem, E., Schinnerer, E., Santoro, F., et al. 2022, A&A, 659, A191
Engelbracht, C. W., Gordon, K. D., Rieke, G. H., et al. 2005, ApJL, 628, L29
Engelbracht, C. W., Rieke, G. H., Gordon, K. D., et al. 2008, ApJ, 678, 804
Evans, A. S., Frayer, D. T., Charmandaris, V., et al. 2022, ApJL, 940, L8
Flagey, N., Boulanger, F., Noriega-Crespo, A., et al. 2011, A&A, 531, A51
Flagey, N., Noriega-Crespo, A., Boulanger, F., et al. 2009, ApJ, 701, 1450

Galliano, F. 2022, Habilitation Thesis, Univ. Paris-Saclay
Galliano, F., Galametz, M., & Jones, A. P. 2018, ARA&A, 56, 673
Galliano, F., Nersesian, A., Bianchi, S., et al. 2021, A&A, 649, A18
Gordon, K. D., Engelbracht, C. W., Rieke, G. H., et al. 2008, ApJ, 682, 336
Gordon, K. D., Roman-Duval, J., Bot, C., et al. 2014, ApJ, 797, 85
Groves, B., Kreckel, K., Santoro, F., et al. 2023, MNRAS, 520, 4902
Harris, C. R., Millman, K. J., van der Walt, S. J., et al. 2020, Natur, 585, 357
Hassani, H., Rosolowsky, E., Leroy, A. K., et al. 2023, ApJL, 944, L21
Helou, G., Roussel, H., Appleton, P., et al. 2004, ApJS, 154, 253
Hensley, B. S., & Draine, B. T. 2023, ApJ, 948, 55
Hunter, J. D. 2007, CSE, 9, 90
James, P. A., & Percival, S. M. 2018, MNRAS, 474, 3101
Jochims, H. W., Baumgaertel, H., & Leach, S. 1996, A&A, 314, 1003
Jones, A. G., Bendo, G. J., Baes, M., et al. 2015, MNRAS, 448, 168
Jones, A. P., Fanciullo, L., Köhler, M., et al. 2013, A&A, 558, A62
Jones, A. P., Köhler, M., Ysard, N., Bocchio, M., & Verstraete, L. 2017, A&A, 602, A46
Joye, W. A., & Mandel, E. 2003, in ASP Conf. Ser. 295, Astronomical Data Analysis Software and Systems XII, ed. H. E. Payne, R. I. Jedrzejewski, & R. N. Hook (San Francisco, CA: ASP), 489
Kassis, M., Adams, J. D., Campbell, M. F., et al. 2006, ApJ, 637, 823
Khramtsova, M. S., Wiebe, D. S., Boley, P. A., & Pavlyuchenkov, Y. N. 2013, MNRAS, 431, 2006
Kim, J., Chevance, M., Kruijssen, J. M. D., et al. 2023, ApJL, 944, L20
Köhler, M., Ysard, N., & Jones, A. P. 2015, A&A, 579, A15
Lai, T. S. Y., Armus, L., U, V., et al. 2022, ApJL, 941, L36
Lee, J. C., Sandstrom, K. M., Leroy, A. K., et al. 2023, ApJL, 944, L17
Leger, A., & D'Hendecourt, L. 1985, A&A, 146, 81
Lenz, D., Hensley, B. S., & Doré, O. 2017, ApJ, 846, 38
Leroy, A. K., Bigiel, F., de Blok, W. J. G., et al. 2012, AJ, 144, 3
Leroy, A. K., Bolatto, A. D., Sandstrom, K., et al. 2023a, ApJL, 944, L10
Leroy, A. K., Hughes, A., Liu, D., et al. 2021a, ApJS, 255, 19
Leroy, A. K., Lee, C., Schruba, A., et al. 2013, ApJL, 769, L12
Leroy, A. K., Sandstrom, K., Rosolowsky, E., et al. 2023b, ApJL, 944, L9
Leroy, A. K., Sandstrom, K. M., Lang, D., et al. 2019, ApJS, 244, 24
Leroy, A. K., Schinnerer, E., Hughes, A., et al. 2021b, ApJS, 257, 43
Li, A. 2020, NatAs, 4, 339
Li, A., & Draine, B. T. 2001, ApJ, 554, 778
Li, A., & Draine, B. T. 2002, ApJ, 576, 762
Madden, S. C., Galliano, F., Jones, A. P., & Sauvage, M. 2006, A&A, 446, 877
Makarov, D., Prugniel, P., Terekhova, N., Courtois, H., & Vauglin, I. 2014, A&A, 570, A13
Marble, A. R., Engelbracht, C. W., van Zee, L., et al. 2010, ApJ, 715, 506
Mathis, J. S., Mezger, P. G., & Panagia, N. 1983, A&A, 128, 212
Matsumoto, K., Hirashita, H., Nagamine, K., et al. 2024, arXiv:2402.02659
Micelotta, E. R., Jones, A. P., & Tielens, A. G. G. M. 2010, A&A, 510, A37
Miville-Deschênes, M. A., Boulanger, F., Joncas, G., & Falgarone, E. 2002, A&A, 381, 209
Neumann, J., Fragkoudi, F., Pérez, I., et al. 2020, A&A, 637, A56
Paradis, D., Mény, C., Demyk, K., Noriega-Crespo, A., & Ristorcelli, I. 2023, A&A, 674, A141
Paradis, D., Paladini, R., Noriega-Crespo, A., et al. 2011, ApJ, 735, 6
Pathak, D., Leroy, A. K., Thompson, T. A., et al. 2024, AJ, 167, 39
Peeters, E., Habart, E., Berne, O., et al. 2024, A&A, 685, A74
Peeters, E., Spoon, H. W. W., & Tielens, A. G. G. M. 2004, ApJ, 613, 986
Pilyugin, L. S., & Grebel, E. K. 2016, MNRAS, 457, 3678
Planck Collaboration, Ade, P. A. R., Aghanim, N., et al. 2011, A&A, 536, A19
Povich, M. S., Stone, J. M., Churchwell, E., et al. 2007, ApJ, 660, 346
Puget, J. L., Leger, A., & Boulanger, F. 1985, A&A, 142, L19
Querejeta, M., Schinnerer, E., Meidt, S., et al. 2021, A&A, 656, A133
Rémy-Ruyer, A., Madden, S. C., Galliano, F., et al. 2015, A&A, 582, A121
Rieke, G. H., Wright, G. S., Böker, T., et al. 2015, PASP, 127, 584
Sandstrom, K. M., Bolatto, A. D., Draine, B. T., Bot, C., & Stanimirović, S. 2010, ApJ, 715, 701
Sandstrom, K. M., Chastenet, J., Sutter, J., et al. 2023, ApJL, 944, L7
Santoro, F., Kreckel, K., Belfiore, F., et al. 2022, A&A, 658, A188
Schruba, A., Leroy, A. K., Walter, F., et al. 2011, AJ, 142, 37
Sellgren, K., Werner, M. W., & Dinerstein, H. L. 1983, ApJL, 271, L13
Shipley, H. V., Papovich, C., Rieke, G. H., Brown, M. J. I., & Moustakas, J. 2016, ApJ, 818, 60
Shivaei, I., Alberts, S., Florian, M., et al. 2024, arXiv:2402.07989
Smith, J. D. T., Draine, B. T., Dale, D. A., et al. 2007, ApJ, 656, 770
Sun, J., Leroy, A. K., Rosolowsky, E., et al. 2022, AJ, 164, 43
Thilker, D. A., Braun, R., & Walterbos, R. A. M. 2000, AJ, 120, 3070
Ujjwal, K., Kartha, S. S., Krishna, R. A., et al. 2024, A&A, 684, A71
Virtanen, P., Gommers, R., Oliphant, T. E., et al. 2020, NatMe, 17, 261
Walter, F., Brinks, E., de Blok, W. J. G., et al. 2008, AJ, 136, 2563
Weingartner, J. C., & Draine, B. T. 2001, ApJ, 548, 296
Whitcomb, C. M., Sandstrom, K., Leroy, A., & Smith, J. D. T. 2023a, ApJ, 948, 88
Whitcomb, C. M., Sandstrom, K., Murphy, E. J., & Linden, S. 2020, ApJ, 901, 47
Whitcomb, C. M., Sandstrom, K., & Smith, J.-D. T. 2023b, RNAAS, 7, 38
Williams, T. G., Kreckel, K., Belfiore, F., et al. 2022, MNRAS, 509, 1303
Williams, T. G., Lee, J. C., Larson, K. L., et al. 2024, ApJS, 273, 13
Wong, T., Xue, R., Bolatto, A. D., et al. 2013, ApJL, 777, L4
Wu, Y., Charmandaris, V., Hao, L., et al. 2006, ApJ, 639, 157
Ysard, N., Abergel, A., Ristorcelli, I., et al. 2013, A&A, 559, A133
Ysard, N., Jones, A. P., Guillet, V., et al. 2024, A&A, 684, A34
Zhen, J., Castellanos, P., Paardekooper, D. M., et al. 2015, ApJL, 804, L7